Structural Investigations on Semiconducting Donor-Acceptor Block Copolymers and Related Model Systems for Organic Photovoltaics

DISSERTATION

zur Erlangung des akademischen Grades

doctor rerum naturalium (Dr. rer. nat.)
genehmigt durch

die Naturwissenschaftliche Fakultät II
Institut für Physik
der Martin-Luther-Universität
Halle-Wittenberg

vorgelegt von
MSc. **Gaurav Kumar Gupta**
geboren am 09.11.1982 in Allahabad, Indien

Gutachter:

1. Prof. Dr. Thomas Thurn-Albrecht

2. Prof. Dr. Christine M. Papadakis

3. Prof. Dr. Wolfgang Paul

Halle (Saale), am 27.05.2014

In fond memory of my grandfather

Late. Krishna Kumar Gupta

Contents

Chapter 1

Introduction

With the present growth of industry and population, there is a huge pressure on conventional energy sources (e.g. oil, coal, natural gas and nuclear fuels) to fulfill the energy requirements. However, these natural resources are limited and will be exhausted in the near future. Therefore, alternate sources of renewable energy must be looked upon to meet the growing demand for energy. One such promising source of renewable energy is deriving power from the sun where the solar energy can be directly transformed into electrical energy. The first solar cells using this concept were made from inorganic semiconductors, such as crystalline Si, as early as in 1950's [1]. Although, inorganic based solar cells exhibit highest power conversion efficiencies [2] and are widely used, requirement of energy consuming production steps and stable encapsulations result in much higher production costs.

Semiconducting organic materials have emerged as an important class of new materials. The pioneering work by Shirakawa et al. about conjugated polyacetylenes in 1977 [3], for which they were awarded the Nobel prize in Chemistry in 2000, led to a significant surge in the research and development in these materials. Although, the charge carrier mobility in organic semiconducting materials is low as compared to their inorganic counterparts, these polymeric semiconductors offer a number of unique benefits. Firstly, the opto-electronic properties of these materials can be fine-tuned by changing the chemical structures. Secondly, these materials offer the ease of processability (simple coating or printing processes) due to their solubility in common solvents, thereby reducing the cost of the fabrication process. Thirdly, the mechanical flexibility allows fabrication of flexible devices. Besides solar cells, these materials have found wide applications in the field of organic light emitting diodes (OLED's) [4] and organic field effect transistors (OFET's) [5]. However, despite significant advances made in polymer based solar cells [2], the power conversion efficiencies are still too low for commercialization.

The photo-excitation in organic semiconductors does not result in generation of free charge carriers, rather, bound electron-hole pairs (excitons) are formed. Dissociation of excitons into free charge carriers occur if these excitons reach an interface within its lifetime which is of the order of 10 - 15 nm on a diffusion length scale. Once the free charge carriers are generated, the electrons and holes must be transported to the

respective electrodes before they recombine. Therefore, exciton dissociation and charge transport puts a morphological constraint of having bi-continuous domains (electron and hole conducting pathways) with interfaces on the exciton diffusion length scale; making morphology control of the active layer one of the key aspects in improving device performance.

Figure 1.1: Schematic representation of donor acceptor morphologies of organic solar cells (a) bilayer morphology, (b) phase separated donor-acceptor blend morphology and (c) ideal heterojunction morphology. The donor component is shown as blue while the acceptor component is shown as red

The first breakthrough in the field of polymeric based solar cells was achieved by introducing the concept of a bilayer heterojunction [6], resulting in enhanced efficiencies [7, 8] due to an efficient charge dissociation at the donor-acceptor interfaces as compared to single layer devices [9]. Further improvement in efficiencies was restricted due to a limited interfacial area in such structures. This limitation was overcome by the introduction of bulk heterojunction concept by blending two polymers in solution having donor and acceptor properties [10, 11]. An ideal bulk heterojunction morphology is supposed if it forms continuous, aligned and interpenetrating domains with structural length scales in the range of exciton diffusion length. Figure 1.1 shows the schematic of different morphologies in organic solar cells. One of the widely investigated material system till date is a blend of a donor polymer poly(3-hexylthiophene) (P3HT) and a fullerene derivative [6,6]-phenyl C_{61}- butyric acid methyl ester (PCBM) as an acceptor. Pronounced improvement in device performance have been observed in this system after thermal annealing as expressed by improved optical absorption [12] and improved crystallinity [13, 14]. This shows the large effect of morphology on solar cell performance. Power conversion efficiencies of up-to 5 % have been recently reported for this system [15, 16], making it commercially one of the most interesting systems. However, a major drawback of the bulk heterojunction solar cell based on a polymer- fullerene system is its morphological instability at elevated temperatures which originates due to the non-equilibrium structures obtained in polymer blends [17]. The kinetically trapped morphology initially obtained in spin casted films is unstable to phase segregation, driven by the strong tendency of the components to crystallize independently, resulting in macrophase separation on long term exposure at elevated temperatures [18, 19]. Thus, despite significant advances and steadily increasing efficiencies in polymer based solar cells, control of morphology and long term stability is still a challenging issue requiring tedious optimization of multiple experimental variables, e.g. relative concentration of donor/acceptor, nature of the solvent deposition technique, introduction of additives and thermal treatments [20–23].

A novel approach towards achieving a controlled morphology is by using block copolymers consisting of covalently linked donor (D) and acceptor (A) segments. The self-assembling properties of a block copolymer can be utilized to control the microphase morphology and to create interfaces in the range of exciton diffusion length. The nanodomains obtained, thus are molecularly pure and can provide efficient pathways for charge transport. Initial studies by Hadziioannou et al. and Thelekkat et al. have also demonstrated the advantages of charge transfer in D-A block copolymers compared to the corresponding blends [24, 25]. Further, several techniques e.g. substrate modifications, shear or electric fields [26–28] are known to vertically align these nanodomains. Such an alignment have also been theoretically predicted to favor improved device performances [29].
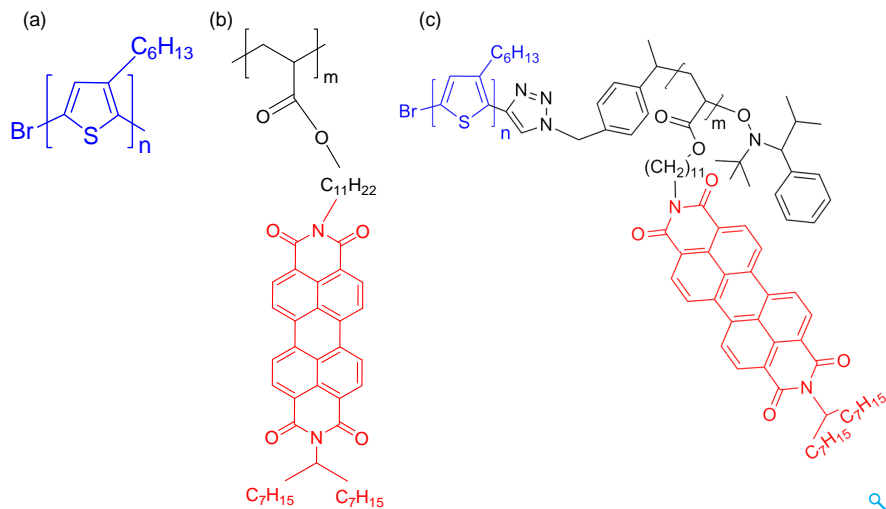
Figure 1.2: Chemical structure of the investigated homopolymers (a) P3HT (donor block) (b) poly(perylene bisimide-acrylate) (PPerAcr) and the (c) fully functionalized donor-acceptor block copolymer consisting of P3HT as the main chain polymer and PPerAcr as a side chain polymer

Self-assembly and structure formation on nanoscopic scales are common phenomenon in polymers, since in these systems a length scale on the order of 10 nm is naturally introduced by the size of the chains [30]. In a block copolymer containing amorphous blocks the microphase separation depends on the incompatibility factor $\chi_F N$ (product of the Flory-Huggins interaction parameter and the degree of polymerization) and the volume fraction. However, in a block copolymer containing crystalline blocks, the structure formation could be driven by microphase separation or crystallization (main chain or side chain). The complexity of microphase separation in crystalline-amorphous block copolymers as well as in double-crystalline block copolymers systems involving poly(ethylene) has been studied in detail by Ryan et al. and Register et al [31–34]. The systems proposed here for photovoltaic applications (Figure 1.2), containing P3HT as a donor block and poly(perylene bisimide-acrylate) (PPerAcr) as the acceptor block, typically combine at least two or even all three of these processes. The P3HT block used in the investigated block copolymer is one of the most efficient material used in organic solar cells due to its high hole mobility [35], high environmental stability and

its tendency to form highly crystalline lamellae [36,37]. On the other hand, PPerAcr is among one of the promising electron acceptor material with high electron mobility of the perylene core [38], strong light absorption [39], thermal stability and forms liquid-crystalline phases at room temperature [40]. It is therefore to be expected, that structure formation processes in these block copolymer materials are complex and result from a competition of kinetic and equilibrium factors.

Various block copolymers containing a conjugated poly(3-alkylthiophene) (P3AT) block as a donor segment and an electronically inactive amorphous blocks as the other segment have been synthesized, with some of them dealing with the issue of microphase separation. [41–44]. But only very few of these crystalline-amorphous block copolymers showed the typical microphase separated structures known from block copolymers having amorphous blocks [42,44].

Among the block copolymers containing P3HT as a donor block, only a few of them contained an electronically active second block; either carrying fullerenes [17,45,46] or perylene bisimides [47–51] as pendant moieties in acceptor block. However, in most of the investigated all conjugated block copolymers, [52–54] either no clear evidence of microphase separation is seen, or the nanostructure formation was driven by the crystallization of P3HT [54]. As a consequence, elongated fibrils or lamellar structures of P3HT were observed instead of microphase separated structures. Recently Guo et al. have demonstrated microphase separation in conjugated P3HT-b-PFTBT symmetric block copolymer having an amorphous PFTBT phase [55]. Indications for complex self-assembly processes were also observed by Ku et al. in P3HT-b-DPP (diketopyrrolopyrrole-terthiophene) systems [56]. Otherwise, up to now, well ordered microphase separated structures in block copolymer systems with semiconducting crystalline blocks have not been observed, most likely due to the crystallization of one of the blocks dominating over microphase separation.

The work presented in this thesis is a part of a collaborative interdisciplinary project involving the research expertise of three groups: (1) Prof. Mukundan Thelekkat, University of Bayreuth; (2) Prof. Thomas Thurn-Albrecht, University of Halle; and (3) Dr. Harald Hoppe, Technical University of Ilmenau. The fundamental aims of the project are:

- Design and synthesis of well-defined novel semiconducting model systems and block copolymers with perylene derivatives as a pendant group in the acceptor block and P3HT as a donor block (University of Bayreuth)

- Investigation of structure formation processes in these polymers in bulk and thin films (University of Halle). This includes an extensive study of the structure and phase behavior on bulk samples employing various experimental techniques e.g. calorimetry, x-ray scattering (small and wide angle) complimented with optical and electron microscopy. Further, the microstructure and orientation in thin films is investigated using x-ray scattering in particular, grazing incidence scattering techniques and atomic force microscopy.

- Device preparation, characterization and optimization of solar cells based on self assembling block copolymers (Technical University Ilmenau)

Due to the complex behavior of the polymers (i.e. the ability to undergo microphase separation, main chain and side chain crystallization), a thorough understanding of the ordering processes is necessary in order to control order and orientation of the mesoscopic structure. Further, the study aims to understand the correlation between the microstructural order and the charge transport properties. Therefore, a bottom-up strategy is employed starting with the study of simplified systems i.e. in individual homopolymers, extending it to more complicated block copolymer systems. This includes investigations of molecular weight dependence and the effect of thermal treatment on the semi-crystalline morphology, crystalline order and texture in P3HT thin films. This is followed by the study of the phase behavior and molecular packing of the electron accepting material i.e. perylenes (with different side groups) and the corresponding homopolymer poly(perylene-bisimide acrylate), PPerAcr, in bulk and thin film samples. As a final step, the ordering process in the block copolymer is investigated to inspect how the incorporation of these semiconducting materials in an all conjugated donor-acceptor block copolymers influence the structure formation processes in bulk samples. Further, it is stimulating to investigate whether the microphase morphology as observed in bulk samples also persists in thin films. If so, is there any preferred orientation of the observed microstructures? What is the crystalline order and texture of the individual blocks under confinement within these microstructures? Is there a correlation between the microstructural and crystalline order and orientation on the charge transport properties in these semiconducting block copolymers?

In this context, the work presented in this thesis is divided into the following chapters.

Chapter 2 provides a theoretical background comprising key concepts about the semi-crystalline structures in conjugated polymers, phase behavior and ordering processes in discotic molecules followed by the thermodynamical and phase behavior of di-block copolymers. Further, concepts of x-ray scattering, in particular grazing incidence x-ray scattering for determining the microstructural and crystalline order and orientation in thin films is also introduced followed by the section describing the space charge limited current devices.

Chapter 3 gives the instrumental details of the various experimental techniques used for the structural investigations.

Chapter 4 elucidates the structural investigations in thin films of the conjugated P3HT homopolymer (donor block) with focus on the molecular weight dependence on the semi-crystalline morphology, effect of thermal treatment on the microstructural properties (crystalline order, crystallite orientation) and its subsequent impact on the transport properties.

Chapter 5 presents the results of microstructural and phase behavior analysis in perylene derivatives and the side chain polymer in bulk and thin films. An important finding in this investigation was that by tuning the side chains/attachment of polymer backbone to the perylene core resulted in a liquid-crystalline phase which leads to enhanced transport properties.

Chapter 6 is dedicated to the microstructural and crystalline order in functionalized donor-acceptor block copolymers consisting of P3HT (main chain) as the donor

block and PPerAcr (side chain) as the acceptor block. The first section of this chapter deals with the investigations of structure formation processes in bulk samples. Combinatorial findings from scattering and transmission electron microscopy measurements reveal microphase separation in block copolymers having semiconducting blocks. Further, the crystalline structure of the individual components, as known from individual homopolymers, was found unaltered in microphase separated domains. The subsequent section documents the result from the microstructural analysis in thin films which reveals that the microphase separation as observed in bulk samples persists in thermally treated films with the orientation of the microstructures parallel to the substrates. The crystalline texture of the individual components was observed to be influenced by the confinement within the microdomains. Consequently, the transport properties in devices made from these block copolymers were found to be largely impacted by the microstructural and crystalline order and orientation.

Chapter 7 provides a summary of conclusions based on the findings of the work presented in this thesis and future scope.

Chapter 2

Basic concepts

Before proceeding to the experimental part, this chapter aims to provide a conceptual background to the experimental studies and interpretations presented in this thesis. The first three sections deal with understanding the semi-crystalline behavior of conjugated polymers (in particular thiophene based polymers), phase behavior and structures in discotic molecules and the theory for thermodynamics and phase behavior of block copolymers respectively. The penultimate section comprises of the basics of x-ray scattering with special focus on the grazing incidence x-ray scattering technique for thin films characterization. The final section describes the space charge limited current method for charge carrier mobility determination.

2.1   Semi-crystalline conjugated polymers

Can polymers form three dimensional crystals? In principle, by choosing identical helical conformations, a periodic structure in 3D can be obtained for all polymers, by orienting the helical axes of all chains parallel to each other and then packing the chains laterally in a regular manner [57]. This applies to all polymers having a linear architecture and a regular chemical constitution. Thus, polymers have the potential to crystallize, albeit in a peculiar way. To understand the peculiarities of crystallization of polymers, it is easier to first understand the crystallization behavior of oligomers. Oligomers are small chain molecules of uniform low molar mass e.g. n- alkanes and prfluoro n- alkanes. In the melt state, oligomeric molecules form coiled conformations. At a lower temperature, these oligomers readily crystallize forming crystals composed of stacked layers with stretched chains (also called extended chain crystals) as shown in Figure 2.1(a). Each stacked layer is an assembly of chain molecules with identical helical conformations with end-groups occupying the interfaces. For a polymer with uniform molar mass, the same crystallization behavior as observed for oligomers could be expected with crystals composed of extended chains. However, in contrast to the oligomers, polymers in general have a certain distribution of molar mass of the chains, irregular chemical constitution and chemical defects. In the backdrop of the above statement, the crystallization behavior of a polymer could be quite different from oligomers. In the melt, polymer chains are in a coiled state. Complete dis-
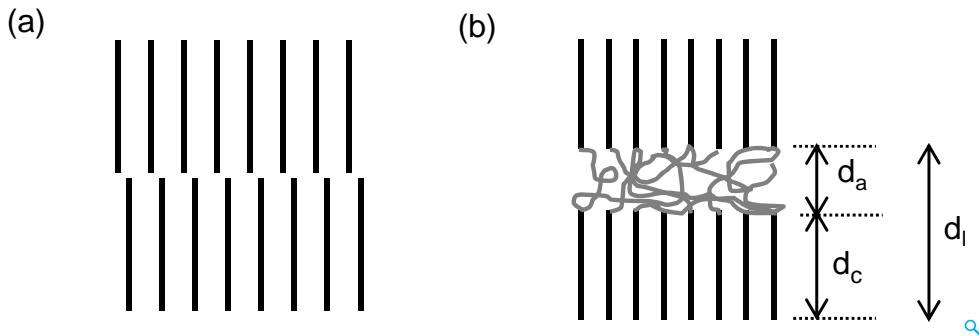
Figure 2.1: Schematic representation of the crystalline structure of an (a) oligomer and the semi-crystalline morphology in a (b) polymer

entanglement of chains does not occur when the polymeric melt is cooled below the equilibrium melting point resulting in a two phase structure consisting of layer like crystallites (crystalline regions) separated by disordered regions (Figure 2.1(b)). Such a morphology is often referred to as a semi-crystalline morphology and is in general common to most of the polymers. The basic mechanism leading to the formation of semi-crystalline morphology could be understood on the basis of a separation process. Crystallization occurs with a certain de-mixing, whereby chains that can be stretched and incorporated into a growing crystal are separated from chain parts which do not crystallize that are removed and shifted to amorphous regions. The amorphous regions can also contain folds or other topological defects, chemical defects and chain ends.

Among the family of conjugated polymers, poly(3-alkylthiophenes) (P3AT's) are an important class of semiconducting polymers due to their high charge carrier mobility, processability from solution and high environmental and thermal stability. They have found wide applications in the field of organic electronics [58, 59]. The semiconducting properties of P3AT's result from the hybridization of the sp^2 orbitals and the overlap of the remaining p_z orbitals, forming a conjugation resulting in delocalization of electrons along the chain. On the other hand, the alkyl side chains are non conducting and only act as a solubilizing group. Side chain substitution has also been used to tune the electronic properties of poly-thiophenes [60] and in some cases also to suppress the crystalline melting temperature by incorporating longer alkyl side chains [61]. In general, P3AT's, like other semi-crystalline polymer, exhibit characteristic structural features on different length scales.

Proceeding from a molecular scale to a microscopic scale, we begin with the chemical structure of this comb like conjugated molecule of poly(3-n alkylthiophene) as shown in Figure 2.2(a). The properties of P3AT's depend strongly on the arrangement of the attached side chains, called as regioregularity. The amount of head-tail couplings is defined as regioregularity, where the head describes position 2 in the vicinity of the alkyl substituent and tail the position 5 of the thiophene ring [64]. Besides head-tail coupling other configurations like head-head and tail-tail couplings are also possible. Depending on the various synthetic approaches P3AT's with quite different regioregularity can be synthesized [65–68]. Figure 2.2(b) shows the various coupling
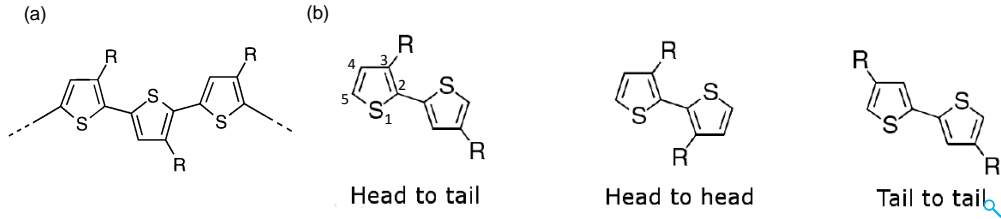
Figure 2.2: (a) Chemical structure of conjugated P3AT [62].(b) Schematic showing various isomeric coupling states observed in P3AT's [63]
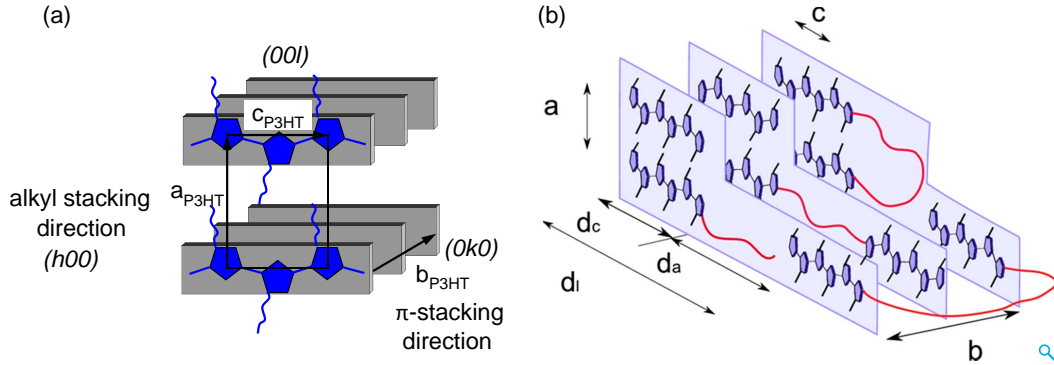

Figure 2.3: (a) Schematic illustration of the orthorhombic unit cell of P3HT illustrating the (h00), (0k0) and (00l) reciprocal lattice directions. (b) Illustration of the semi-crystalline morphology in P3HT; the long period $d_l = d_c + d_a$ where d_a is the thickness of the amorphous layer and d_c is the thickness of the crystalline layer [73]

schemes in P3AT's. While high regioregularity (head-tail couplings) allows for planar orientation of thiophene rings, head-head or tail-tail couplings cause steric interactions of the alkyl chains and an out of plane twist of the thiophene rings resulting in a loss of conjugation and an increased band gap with a consequent reduction in conductivity. Therefore, irregular couplings not only hinder charge transport along the chain (intra-molecular transport) but also along the the π-π stacking (intermolecular transport). Additionally, the charge carrier mobility depends on the chain lengths and increases with increasing molecular weights [69]. A better interconnectivity between the micro-crystalline domains throughout the amorphous regions and an increased crystallinity are discussed as the origin for the improved mobility of high molecular weight samples [37, 70]. Among the P3AT's, P3HT exhibits an optimum balance between good solubility and high charge carrier mobility [71] and is still regarded as a power-horse due to its large success in bulk hetero-junction solar cells [72].

The self assembled crystalline structure of poly-thiophenes has been investigated at several instances [74–77]. Although the detailed parameters are different among different research groups, there is a general consensus regarding the packing motif of P3HT in which stacks of poly-conjugated main chains organize themselves in a lamellar fashion with layers of π-π stacked backbones separated by about 0.38 nm [58]. While the periodicity between the main chain and side chain is of the order of 1.6 nm, the
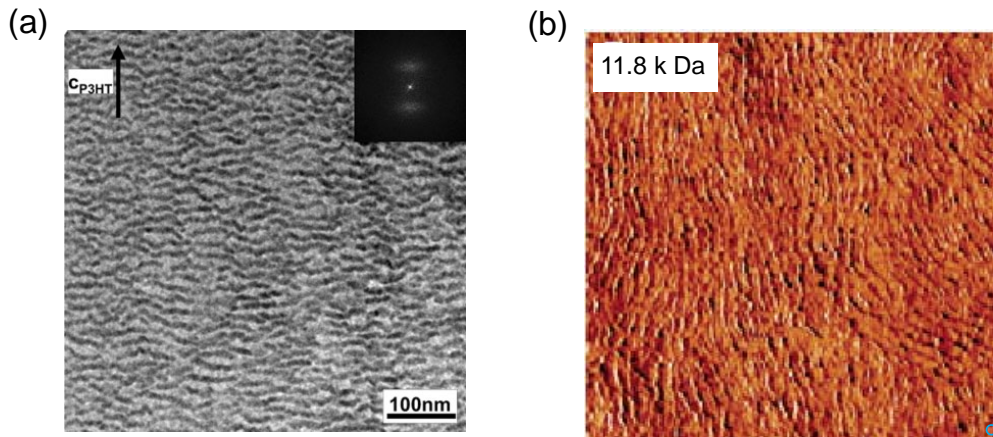
Figure 2.4: (a) Bright field TEM image exhibiting the semi-crystalline morphology of an oriented P3HT thin film. The direction of the chain axis of P3HT is along c_{P3HT} [36]. (b) AFM image (tapping mode) of drop casted thin film of P3HT showing a nano-fibrillar structure [80]

trans-planar sequence along the thiophene backbone is 0.78 nm [73]. Commonly, the unit cell of P3HT is described by an orthorhombic [76] or a monoclinic unit cell [78] such that the side chains are directed along the 'a' axis, the π-π stacking along the 'b' axis and the main chain direction along the 'c' axis as shown in Figure 2.3(a). In layered systems, the side chains can be disordered or highly organized depending on their structure and attachment density along the backbone. However, the description of the ordering state of the side chains is beyond the scope of this thesis, and the reader is directed to look for other sources [73, 79].

Another characteristic feature exhibited by P3HT is the semi-crystalline morphology, which involves the periodic alternation of the ordered crystalline and disordered amorphous layers of thickness d_c and d_a respectively as shown in Figure2.3(b). The long period which describes the periodicity of such a lamellar structure is given by the sum $d_c + d_a$ which is an order of magnitude larger than the lattice parameters 'a', 'b' and 'c'. Brinkmann and coworkers reported a clear evidence of semi-crystalline structure in regio-regular P3HT oriented by directional solidification on 1,3,5- trichlorobenzene (Figure 2.4(a)) [36]. The periodicity of crystalline lamellae and the amorphous zone was 28 nm with the molecular chains oriented normal to the crystalline lamellae. Similarly, a well-defined nanofibrillar morphology was also observed by McCullough and coworkers in thin films of regio-regular P3HT produced by drop casting from toluene [80]. Figure 2.4(b) shows an example for a P3HT sample with molecular weight of 11.8 kg/mol. The molecular chains are again oriented perpendicular to the long axis of the nanofibrilles. Such an observation of a lamellar morphology is very common in semi-crystalline polymers [37].

In thin films of P3HT, the alkyl stacking direction tends to lie out of the plane of substrate while the π- stacking direction lies in the plane of the substrate. Crystallites with their alkyl stacking direction out of plane of the substrate are referred as 'edge-on'. When crystallites are oriented with their π-stacking direction out of the

plane of the substrate , such a crystallite orientation is termed as face on. Miller indices will be used to identify reciprocal lattice directions throughout this work. The crystallite orientation and crystallinity (in thin films) in P3HT is known to depend on various factors e.g. regioregularity, molecular weight, processing conditions (e.g. solvents, annealing conditions, chemically modified substrates, epitaxy etc.) [58,81–83]. Sirringhaus et al. reported that for P3HT with high regioregularity (> 91 %) and low molecular weight, the crystallites adopted an edge-on orientation while samples with low regioregularity (81 %) and high molecular weight, the crystallites are preferentially oriented with the (100)-axis in the plane and the (010)-axis normal to the film [58]. Thankaraj and co-workers demonstrated an increase in preferential edge-on crystallite orientation and an enhanced crystallinity on pure and silanized Si/SiO_2 by varying the casting conditions from room temperature to -12°C [84]. Choi et al. also reported an enhanced crystallinity and a preferential edge-on orientation of crystallites in melt crystallized films as compared to as spun films [85]. Thus, owing to its technological relevance in the field of organic electronics, P3HT is an ideal material for an in-depth investigations of fundamental microstructure-property relationships in semi-crystalline semiconductors.

2.2   Discotic molecules

Compared to solid crystals, liquid crystals possess a higher intermolecular and intra-molecular mobility (i.e. several degrees of freedom of molecular rotation, translation and intra-molecular conformational changes) [86]. On the other hand, liquid crystals possess a higher degree of order as compared to the isotropic liquids. Derived from the shape of the constituting molecules liquids crystals can be classified as calamitic (rod like mesogens), discotic (disc shaped mesogens) or sanidic (board shaped mesogens). In this section only the phase behavior and the structures formed by discotic molecules are discussed. Discotic molecules comprise of a rigid disc shaped aromatic core surrounded by flexible side chains. While the core determines the opto-electronic properties [87], the side chains are responsible for lowering the melting temperature and an increased solubility. The liquid-crystalline phases formed by these discotic molecules was first observed in 1977 in hexa-substituted benzene derivatives [88] while such phases had been already discovered in calamitic molecules by Reinitzer in 1888.

Variations in the size and symmetry of the core, side chain lengths have an essential influence on the thermotropic properties and the packing of molecules. Figure 2.5 gives a schematic illustration of order in different phases observed in discotic molecules. In the isotropic state, discotic molecules are characterized by a random, isotropic structure and fluid-like behavior, analogous to conventional liquids. Similar to rod-shaped molecules, discotic molecules also form nematic phases where the short molecular axes of discotic mesogens is preferentially oriented along a common direction defined as the director n. This results in a long range orientational order with rotational symmetry around n with the molecular centers of mass translationally disordered in all directions (no long range range positional order). The more ordered structure of discotic molecules is shown in Figure 2.5(c), where the molecules arrange themselves into
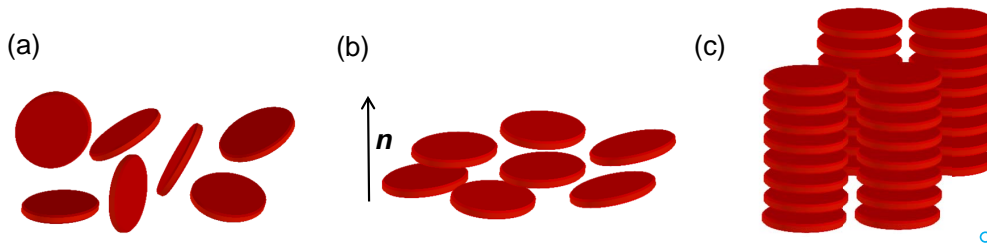
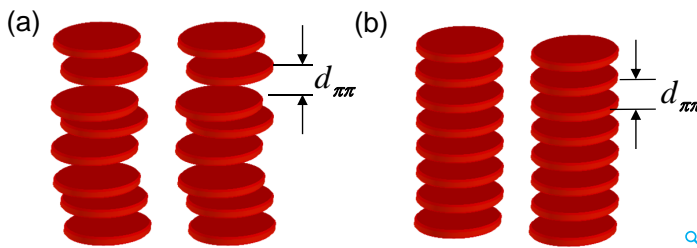**Figure 2.5:** Different ordered phases in discotic molecules (a) isotropic, (b) nematic and (c) 2D ordered

Figure 2.6: (a) Schematic of the ordering behavior of the mesogens along the π- π stacking direction (a) disordered and (b) ordered

columnar or lamellar stacks, which then can pack on a two-dimensional lattice with hexagonal, rectangular or oblique symmetries. Since the spacing between the stacks are comparable to the lateral dimensions of the molecules ($\approx$ 3 nm- 4 nm), the (*hk0*) reflections resulting from the two dimensional packing of the stacks usually appear at intermediate scattering angles.

The stacking of the molecules, a characteristic motive in the self organization of discotic molecules, results due to the strong π -π interactions (aromatic interactions) caused by the intermolecular overlapping of the p-orbitals in π conjugated systems [89]. Such a stacking behavior of the molecules is assumed to be advantageous for a 1D charge transport along the columns. The arrangement of molecules within the stacks can either be ordered with long range correlational order of mesogenic cores or disordered having a short correlational order as shown in Figure 2.6. X-ray scattering measurements can distinguish between these two arrangements. The distance between the molecules within the stacks is of the order of (0.3 to 0.4) nm which gives rise to a peak in the wide angle region. The correlation length of the molecules within the stacks can be determined from the full width at half maximum (FWHM) of this reflection ($l_{corr} = 2\pi/\Delta q$). Further, the side chains surrounding disc-shaped mesogenic cores can either be in a liquid like or in a crystalline state. Thus, different discotic phases can be distinguished depending on the ordering of the mesogenic cores within the stacks and the ordering state of the side chains.

The crystalline state, in which the discotic cores are correlated in 3D with high orientational and positional order along with crystalline side chains represents the most ordered state. A disordering of the side chains leads to a transition from the crystalline

Table 2.1: Summary of the various phases formed by discotic molecules [90]

Phases	Order	Experimental evidence (XRD)
Isotropic	No positional order + no orientational order + liquid like side chains	broad peak in the intermediate angle region
Nematic	No positional order + 1-D orientational order + liquid like side chains	broad peak in the intermediate and wide angle regions
Liquid crystalline disordered	2D crystalline + liquid like positional order along the π stacking + liquid like side chains	sharp (hk0) + broad (00l) reflection
Liquid crystalline ordered	2D crystalline + 1-D positional order along the π stacking + liquid like side chains	sharp (hk0) + sharp (00l) reflection
Plastic	3D crystalline + liquid like side chains	(hkl) reflections with h or k and l non-zero
Crystalline	3D crystalline + crystalline side chains	(hkl) reflections with h or k and l non-zero

state to a liquid-crystalline phase. If the side chains and the discotic cores become disordered simultaneously (melt at the same temperature), a direct transition from the crystalline to an isotropic phase would be detected. The two-dimensional positional order defined by the packing of the stacks and the one-dimensional positional order along the π-π stacking direction are uncorrelated in an ordered liquid-crystalline state. An intermediate phase, between the crystalline and liquid-crystalline phase, called the plastic phase has also been identified in which the cores have a 3D correlated order with liquid like side chains. A characteristic 3D ordered structures, in both plastic and crystalline phases, give rise to sharp (hk0) as well as reflections with mixed indices (h or k non zero and l non-zero). Therefore, a clear identification of between these two phases is not possible from scattering measurements alone. The plastic phases have been identified by investigating the dynamic properties e.g. by dielectric relaxation method [91,92]. A summary of the possible phases in discotic molecules is given in Table 2.1. While some discotic compounds exhibit only one of these phases, other compounds exhibit several phases [93,94].

The shape of the stack projection onto the lattice plane defines whether a columnar or lamellar structures will be formed. Columnar structures have been observed for all discotic molecules irrespective of the differences in the shape of the mesogenic cores e.g. in hexabenzenecoronene, triphenylene, pthalocynanine (circular core) and perylenes (rectangular core) [89,91,95,96]. Here every molecule is rotated at a certain angle with respect to each other with the angle of rotation covering the entire angular range.
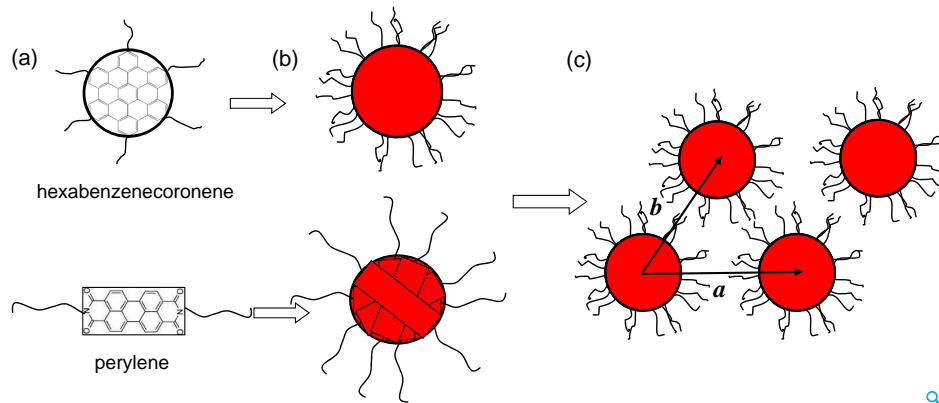
Figure 2.7: (a) Schematic illustration of columnar structures (a) single molecules of different shapes, (b) top view of the columns onto the lattice plane, (c) ordering of columns in 2D
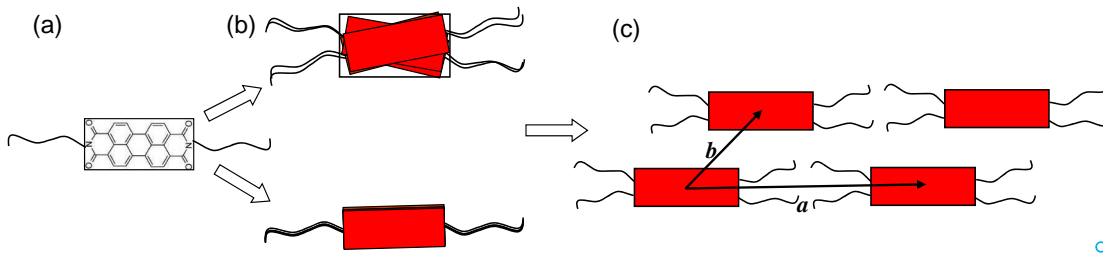

Figure 2.8: Schematic illustration of the formation of lamellar structures (a) single molecule of asymmetric perylene, (b) top view of stacks onto the lattice plane, (c) ordering of stacks in 2D

Figure 2.7(b) shows the top view of such a column which would appear as circles with side chains coming out in all possible directions.These columns can pack on a two-dimensional lattice forming columnar phases with hexagonal, rectangular or oblique symmetries (Figure 2.7(c)). The distance between the columns depend on the length of the mesogenic core and the side chains and are typically of the order of few nanometers.

Another possibility is the stacking of the molecules on top of each other with a limited angular range of the emanating side chains. This results in an asymmetrical distribution of the side chains around the mesogenic cores as shown in Figure 2.8(b). lamellar structures with rectangular or oblique symmetries are favored over the structures with circular symmetry due the deviation in stacking cross section (Figure 2.8(c)). Lamellar arrangements have been observed in perylene derivatives (with linear substituents and asymmetrically substituted perylene-bis-imides) [40, 97–99] with edge-to-edge ordering of the perylene cores. In lamellar structures, the smallest distance (edge-to-edge) is the distance between the neighboring molecules corresponding to the width of the mesogenic cores. For perylene derivatives the unit cell parameter b along the edge-to-edge direction was found to be b $\approx$ 1.03 nm for a unit cell containing one molecule [97, 98] and 2.2 nm for a unit cell containing 2 molecules [99] which is

close agreement with the width $w = 0.92$ nm of the perylene core [100].

These discotic molecules can be attached to each other via flexible spacers forming polymers either as a main chain [101, 102] or to a polymeric backbone as pendant groups [103, 104]. Such a linking often results in a reduced order leading to formation of liquid-crystalline phases in these polymers. As compared to the low molecular weight discotic molecules, the polymeric counterparts are more interesting due to film forming properties and mechanical stability. However, in contrast to the polymers containing rod like (calamitic) molecules as a side chain, detailed studies on the packing and phase behavior in polymers containing discotic molecules are rather limited [105–107]. Most of the examples investigated deal with polymers containing triphenylene moieties attached to different backbones [106, 108, 109]. Although, side chain polymers containing perylene bisimide have been incorporated as one block in donor acceptor diblock copolymers with possible applications in organic solar cells [25, 49, 110], the question of how the incorporation of discotic molecules into a side chain polymer influences packing was barely addressed.

2.3 Thermodynamics and phase behavior of di-block copolymers

Self assembling properties of block copolymers into a variety of ordered structures on the nanoscopic scale make them interesting systems for various applications in the field of nanotechnology [111]. In the molten state, block copolymers (with non-crystallizable blocks) can self assemble into various ordered structures via the process of microphase separation [112]. Microphase separation is a characteristic feature of a block copolymer and arises due to strong repulsive interactions between the unlike sequences A and B of a di-block copolymer A-B. The enthalpy associated with the demixing of the constituents drives the process of microphase separation. However, due to the chemical connectivity between the constituents, complete segregation on a macroscopic scale as observed in polymer blends [30, 57], does not occur. Microphase separation was first observed in concentrated solutions of block copolymers and later on in many other co-polymer systems, particularly in molten block copolymers [30, 112–114]. In a microphase separated state, the microdomains are not located at random but may form a regular arrangement giving rise to a periodic structure with a periodicity on the order of R_g [57], where R_g is the co-polymer radius of gyration. Mesophases with various types of lattices have been observed e.g cubic lattice of spheres, hexagonal lattice of cylinders, lamellar and gyroid structures as shown in Figure 2.9 [111].

An essential parameter in all the theories of microphase separation in block copolymers is the interaction parameter χ_F (also called as Flory-Huggins interaction parameter). Within the lattice model, the Flory-Huggins interaction parameter is given by equation (2.1) [115]

$$\chi_F = \frac{Z}{k_B T} \left[\epsilon_{AB} - \frac{1}{2} \left(\epsilon_{AA} + \epsilon_{BB} \right) \right] \tag{2.1}$$

where ϵ_{ij} is the segmental van der Waals interaction energy between the segments
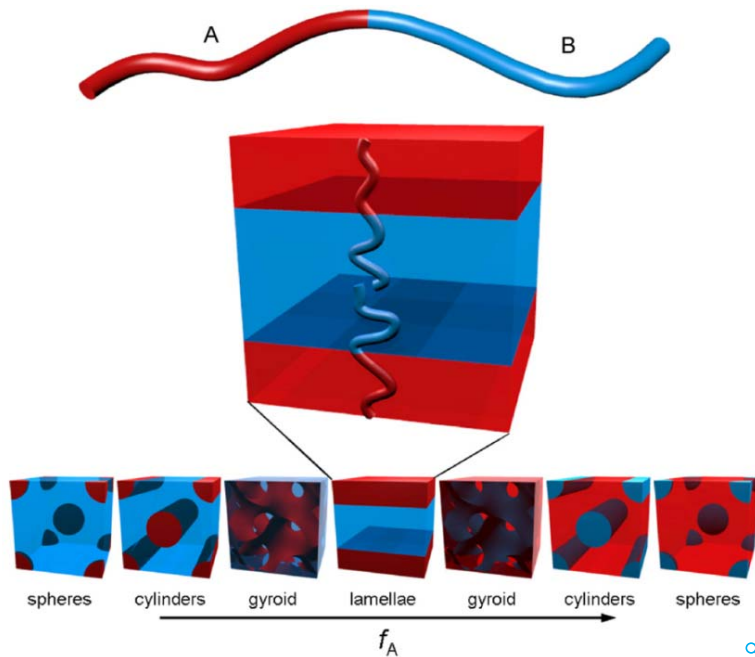
Figure 2.9: Schematic of various thermodynamically stable phases observed in a block copolymer [111]

i and j, Z is the number of nearest neighbor monomer, k_B is the Boltzmann constant and T is the temperature. In the above expression for the interaction parameter, it is assumed that the system is in the limit of zero compressibility. However, polymer chains in real exhibit departure from such an ideal situation and also exhibit a certain degree of polydispersity. Such effects are taken into consideration by additional entropic contributions in χ_F. In general, the Flory-Huggins interaction parameter can be empirically expressed as $\chi_F = A + B/T$, where A and B are constants for a particular system and can be calculated experimentally. While a positive χ_F shows repulsion between the monomers A and B, a negative value signifies mixing. Besides these enthalpic contributions, the thermodynamic state of a block copolymer is also determined by entropic contributions. The complete thermodynamic description is given by the Gibbs free energy

$$G = H - TS \tag{2.2}$$

where H is the total enthalpy given by H = U - pV (U is the internal energy, p is the pressure and V is the volume of the system), T is the temperature and S is the entropy. The minimum of the total free energy gives the equilibrium state.

For most cases it is experimentally observed that χ_F is positive [116]. Since χ_F is positive, there is a tendency to decrease the number of contacts between monomers A and B in order to lower the enthalpic contribution to the free energy. However, a decrease in the number of contacts A-B reduces the entropy of the system and consequently increases the free energy. Hence, the equilibrium state in a block copolymer is a balance of these two competing effects.
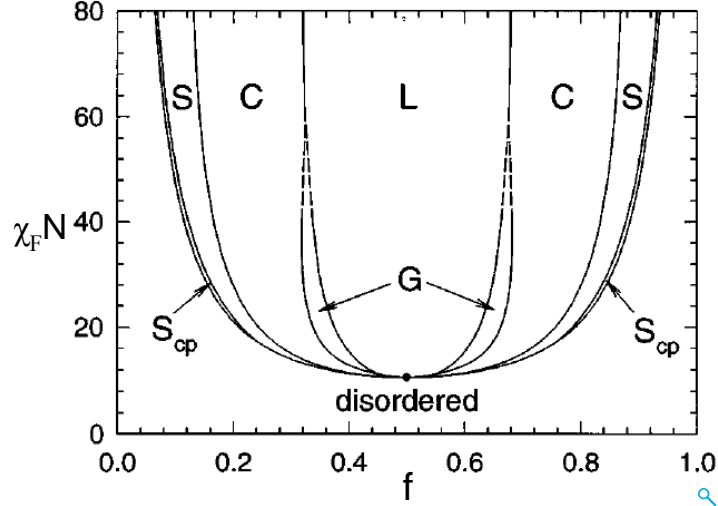
Figure 2.10: Phase diagram of a block copolymer melt showing various ordered phases as a function of incompatibility factor and the composition f. The dot marks the critical point below which the block copolymer forms a disordered melt [117]

Another parameter that strongly influences the thermodynamic phase behavior of the block copolymer is the total degree of polymerization N. Since the entropic and enthalpic contributions to the free energy scale as N^{-1} and χ_F respectively, it is the product $\chi_F N$ that parametrizes the block copolymer phase behavior along with the composition of the co-polymer f (where f is the number of monomers A in the chain i.e. f = N_A/N). For $\chi_F N \approx 0$ or sufficiently small, the entropic effects are dominant and favor mixing: the system exhibits an isotropic phase with the monomeric units A and B of the chains interpenetrating each other. Such a phase is called the disordered phase [112]. On the other hand, when the system is cooled (or composed of longer chains) such that $\chi_F N$ is larger than a certain value $(\chi_F N)_c$ or T < T_{ODT} (where T_{ODT} is defined as order-disorder transition temperature) [30], the enthalpic term in the free energy dominates and the system exhibits microphase separation. The phase diagram of a block copolymer showing various ordered phases as a function of incompatibility factor and the composition is shown in Figure 2.10.

Depending on the degree of incompatibility χ_FN, several regimes have been identified:

1. Strong segregation regime $(\chi_F N > 100)$: This regime is characterized with sharp interfaces [118] with the width depending on the χ_F parameter as $a\chi_F^{-1/2}$ where 'a' is the statistical segment length. In this regime phase boundaries are predicted to depend only on co-polymer composition f [119] and terminating at $\chi_F N = 100$ [30].

2. Weak segregation regime $(\chi_F N \approx 10)$: The phase diagram for weakly segregated di-blocks was first computed by Leibler using the Landau mean field approximation assuming that all chains in the block copolymer have same degree of polymerization N and same composition (i.e. monodisperse) and have zero

compressibility [112]. In his theory, Leibler predicted that only two quantities are relevant parameters for the characterization of phase equilibrium in molten di-block copolymers namely : the composition f (fraction of monomers A in the chain i.e. f = N_A/N) and the product $\chi_F N$. According to the work by Leibler, he was able to construct the phase diagram by comparing the free energies of the three classical ordered phases (lamellar, cylindrical and spherical) with respect to the disordered phase. Leibler was also able to locate the microphase separation transition at which the disordered block copolymer melt orders. For a symmetric block copolymer i.e. f = 0.5, the critical point $(\chi_F N)_c = 10.495$, where the disordered melt state orders into a lamellar microphase separated state. The block copolymers investigated in this thesis form weakly segregated systems [120].

3. Intermediate segregation regime ($\chi_F N \approx 10$ - 100) : This regime lies between the weak and strong segregation regime. The strong and weak segregation limit theories for block copolymer melts have been unified by Matsen and co-workers using numerical solutions of self consistent field equations, without approximations such as narrow phase approximations. The notable aspects of the phase behavior of block copolymers in this regime was the explanation of the existence of a new phase using self consistent field theory (SCFT), the double gyroid phase, in addition to the conventional phases as predicted by Leibler [117, 121, 122].

2.3.1 Structure factor in the disordered phase

Scattering experiments are a very attractive method for investigating various aspects of microphase separation e.g small angle x-ray scattering (SAXS), small angle neutron scattering (SANS). SAXS is very suitable when the chemical species of the co-polymer chain have significantly different electron densities (e.g., copoly(styrene-isoprene)). In addition to the phase diagram, Leibler provided an expression for the disordered phase structure factor S(q) [112]. Within the random phase approximation this function is given by

$$S(q) = N/\left[F(x, f) - 2\chi_F N\right] \tag{2.3}$$

where

$$F(x, f) = \frac{D(1, x)}{D(f, x)D(1 - f, x) - \frac{1}{4}\left[D(1, x) - D(f, x) - D(1 - f, x)\right]} \tag{2.4}$$

and D(f, x) is the debye function, defined as :

$$D(f, x) = \frac{2}{x^2}\left[fx - 1 + e^{-fx}\right] \tag{2.5}$$

and

$$x = \frac{q^2 N l^2}{6} = q^2 R_g^2 \tag{2.6}$$

At q = 0, the structure factor S(q) vanishes as the system is assumed to be incompressible. For large scattering vectors q (i.e. qR » 1), S(q) is again independent of the
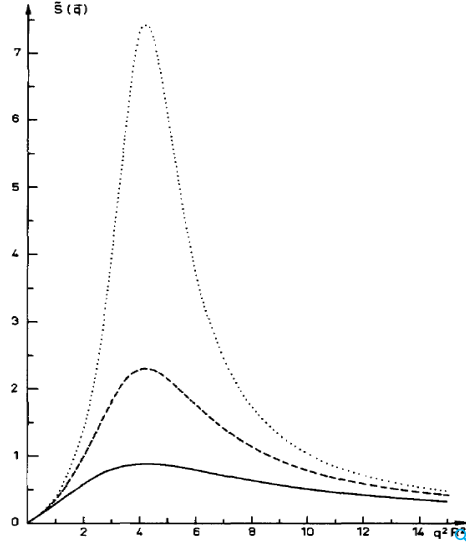
Figure 2.11: Scattering intensity (in arbitrary units) of a molten diblock copolymer with composition f = 0.25 as a function of x = $(qR)^2$ for different interaction parameters: $\chi_F N = 17.5$ (dotted lines); $\chi_F N = 16.0$ (dashed lines); $\chi_F N = 12.5$ (solid lines). The interaction parameter for which $S(q^*)$ diverges (spinodal point) is given by $\chi_F N = 18.2$ [112]

interaction parameter χ_F and tends to zero like $1/q^2$ i.e.

$$S(q) \approx \frac{2N}{q^2 R^2} f(1 - f) \tag{2.7}$$

For small q, (qR ≪ 1), S(q) is again independent of χ_F but now tends to zero like q^2 :

$$S(q) \approx 2Nf^2(1 - f)\frac{q^2 R^2}{3} \tag{2.8}$$

The S(q) $\approx q^2$ dependence is attributed to the 'correlation hole' [112] effect because each monomer is surrounded by a correlation hole, inside of which the concentration of monomers from other chains is slightly reduced [115]. The size of this correlation hole is that of a single chain. Therefore, S(q) develops a maximum (at intermediate q values) which, at high temperatures, results solely from a fixed length scale reflecting the average distance between the centers of the A and B blocks. Although the presence of the peak in S(q) is independent of the segregation effects (especially at high temperatures), the intensity and the shape of the curve depends strongly on the product χ_FN as seen from equation (2.3). However, the segregation effects become more prominent at lower temperatures. This is illustrated in the following example. Figure 2.11 shows an exemplary plot of the S(q) as a function of $(qR)^2$ for different values of χ_FN. A broad peak is observed for small χ_FN values which becomes narrower and higher in intensity with increasing χ_FN. At a certain critical value of χ_FN, $\chi_F N = (\chi_F N)_s$, the structure factor S(q) diverges at $|\mathbf{q}| = q^*$. This is called as the spinodal point. At this point a drastic change in the width of the peak and its temperature dependence could

be observed. A phase transition from the disordered phase to a microphase separated phase occurs. The periodicity of the microstructure corresponding to the scattering vector q* is then given by d = $2\pi/q^*$.

2.4 X-ray scattering

X-ray diffraction technique is a powerful, non destructive method to characterize the structures formed by microphase separation and crystallization processes. The length scale of the investigated structures can vary from micrometer (small angle x-ray scattering) to molecular range (wide angle x-ray scattering). This section introduces the basic principles of scattering techniques used in this thesis.

2.4.1 X-ray diffraction basics

The basics of x-ray diffraction are discussed in this section. More in- depth description could be found in other texts. [123, 124] The physics behind x-ray diffraction is based on the elastic scattering (i.e. the wavelength of the incoming and diffracted beam remains constant) of radiation beams reflected from well ordered lattice planes. A simple explanation of the diffracted beams from crystal planes is given by Bragg's law (Figure 2.12(a)). A crystal can be considered to consist of parallel planes of atoms. Suppose that incident waves are reflected specularly (angle of incidence equal to the angle of reflection), the diffracted beams are found when the reflections from parallel plane of atoms interfere constructively. For an incoming radiation with wavelength λ, incident angle θ, and interplanar spacing d it follows that

$$n \cdot 2\pi = \frac{2\pi}{\lambda} 2d \, \sin\theta_B \tag{2.9}$$

$$n \cdot \lambda = 2d \, \sin\theta_B \tag{2.10}$$

Equation (2.10) is the Bragg's law, and θ_B is the incident angle for which Bragg condition is satisfied, referred as the Bragg angle.

An elegant approach to study diffraction is by operating in reciprocal space. Every crystal lattice in real space corresponds to a lattice in reciprocal space. The transformation equations for the lattice vectors from real space to reciprocal space are given by

$$\mathbf{a}^* = 2\pi \frac{\mathbf{b} \times \mathbf{c}}{\mathbf{a} \cdot (\mathbf{b} \times \mathbf{c})} \tag{2.11}$$

$$\mathbf{b}^* = 2\pi \frac{\mathbf{c} \times \mathbf{a}}{\mathbf{a} \cdot (\mathbf{b} \times \mathbf{c})} \tag{2.12}$$

$$\mathbf{c}^* = 2\pi \frac{\mathbf{a} \times \mathbf{b}}{\mathbf{a} \cdot (\mathbf{b} \times \mathbf{c})} \tag{2.13}$$

The general reciprocal lattice vector is defined as:

$$\mathbf{G}_{hkl} = h\mathbf{a}^* + k\mathbf{b}^* + l\mathbf{c}^* \tag{2.14}$$
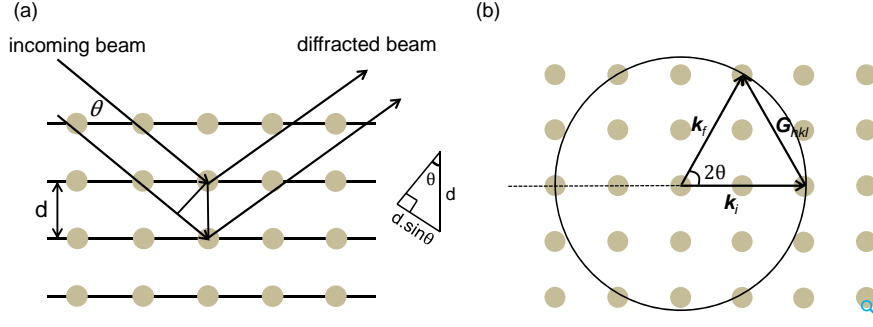
Figure 2.12: (a) Derivation of Bragg law in real space based on the constructive interference of diffracted beams. (b) Ewald sphere construction for a two dimensional square lattice. The radius of the Ewald sphere is equal to $2\pi/\lambda$

where h, k, l are the Miller indices of the corresponding planes within a crystal. The relationship between the magnitude of G_{hkl} and the interplanar spacing is given by:

$$|\mathbf{G}_{hkl}| = \frac{2\pi}{d_{hkl}} \tag{2.15}$$

The diffraction condition in reciprocal space can be also be illustrated using an Ewald sphere construction as shown in Figure 2.12(b). The incoming wave-vector $\mathbf{k}_i$ is drawn in the direction of the incident x-ray beam, with the choice of origin such that it terminates at one of the reciprocal lattice point. A sphere of radius $|\mathbf{k}_i| = 2\pi/\lambda$ is drawn. Any reciprocal lattice point that lies on this sphere can be connected by reciprocal lattice vector $\mathbf{G}_{hkl}$. The diffracted x-ray beam is in the direction $\mathbf{k}_f$ (which also has its origin at the center of the Ewald's sphere), and thus, satisfies the Bragg condition.

$$\mathbf{q}_B = (\mathbf{k}_f - \mathbf{k}_i) = 2\pi\mathbf{G}_{hkl} \tag{2.16}$$

$$|\mathbf{q}_B| = \frac{4\pi}{\lambda}sin\theta_B = \frac{2\pi}{d_{hkl}} \tag{2.17}$$

Diffraction data throughout this thesis will be shown in terms of $\mathbf{q}$, rather than the incident angle.

2.4.2 Grazing incidence diffraction

Within the last few years, grazing incidence x-ray scattering has emerged as a versatile and powerful technique to investigate micro and nano-structured thin films and surfaces. Grazing incidence x-ray scattering overcomes the limitations of conventional x-ray scattering with respect to small sample volumes in the thin film geometry. Here, the incident x-ray beam impinges under a very shallow angle onto the sample surface resulting in a large illumination length. By varying the sample to detector distance, the scattering angle and hence the resolvable length scales can be tuned accordingly. Thus

structures ranging from molecular dimensions (0.2 nm) up to micrometer range can be resolved. The full potential of grazing incidence x-ray scattering is realized with using a synchrotron radiation source in combination (which facilitates high radiation flux, collimation, choice of wavelength etc.) with two-dimensional detectors giving complete structural information (in-plane as well as out-of plane structures). Although, the first pioneering works of investigating the structure of gold particles on Si substrate using GISAXS was done by Levine and co-workers in 1989 [125], this method was introduced in the field of soft matter and polymers by Peter Müller-Buschbaum and co-workers in 1997 only [126]. The following section describes the basic principles of grazing incidence x-ray scattering.

Grazing incidence small angle scattering (GISAXS)

The physical process of scattering describes the reflection of an electromagnetic wave or particle at an object or in matter [127]. The electric field vector of a plane electromagnetic wave is given by

$$\mathbf{E}(\mathbf{r}) = \mathbf{E}_\circ exp[i\mathbf{k}_i \cdot \mathbf{r}] \tag{2.18}$$

where $\mathbf{E}_\circ$ is the amplitude, $\mathbf{k}_i$ is the wave-vector and $\mathbf{r}$ is the position vector. The modulus of the wave-vector is $k = |\mathbf{k}_i| = 2\pi/\lambda$. The electromagnetic wave propagation is given by the Hemholtz equation

$$\Delta\mathbf{E}(\mathbf{r}) + k^2 n^2(\mathbf{r})\mathbf{E}(\mathbf{r}) = 0 \tag{2.19}$$

where $n(\mathbf{r})$ is the position dependent refractive index and is given by

$$n(\mathbf{r}) = 1 - \delta(\mathbf{r}) + i\beta(\mathbf{r}) \tag{2.20}$$

with the dispersion

$$\delta(\mathbf{r}) = \frac{\lambda^2}{2\pi} r_e \rho(\mathbf{r}) \sum_{j=1}^{N} \frac{f_j^\circ + f_j^{'}(E)}{Z} \tag{2.21}$$

and the absorption

$$\beta(\mathbf{r}) = \frac{\lambda^2}{2\pi} r_e \rho(\mathbf{r}) \sum_{j=1}^{N} \frac{f_j^{“}(E)}{Z} = \frac{\lambda}{4\pi}\mu(\mathbf{r}) \tag{2.22}$$

where r_e is the classical electron radius, $\rho(\mathbf{r})$ the position dependent electron density, Z is the number of electrons and $f_j = f_j^\circ + f_j^{'}(E) + f_j^{“}(E)$ the forced oscillator strength of j_{th} atom [127]. For x-rays, $n(\mathbf{r})$ of matter is slightly less than unity, and therefore, total external reflection occurs at small angles. For small incident and exit angles, the influence of periodic crystal structures on the scattered intensity can be neglected and a description based on one mean refractive index n is appropriate [128]. Thus, the dispersion and absorption of a material are expressed by δ and β. Further, the absorption coefficient for the organic materials is negligible and hence neglected. The angle of total reflection is then given by $\alpha_c \approx \sqrt{2\delta}$ [127].
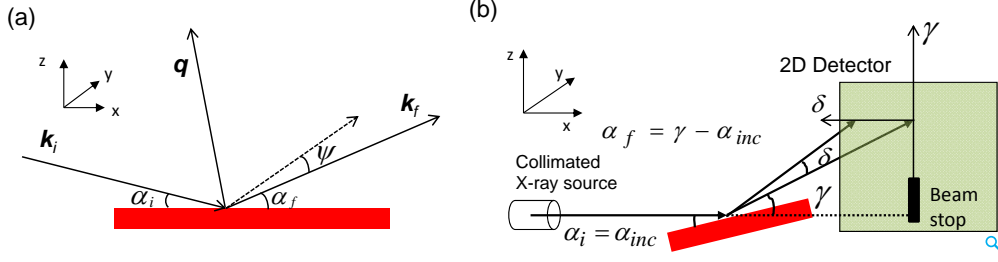
Figure 2.13: (a) Schematic of the grazing incidence scattering geometry. The incident angle is denoted by α_i, the exit angle α_f and an out of plane angle ψ. (b) Schematic of the GID set-up used at ESRF ID 10 showing the experimentally measured angles. The sample to detector distance determines the different scattering regimes

The scattering geomtery of GISAXS setup is shown in Figure 2.13(a). The sample surface defines the (x-y) plane with the x-axis oriented along the direction of incident x-ray beam, while the y-axis is perpendicular to the scattering plane defined by the incident angle α_i and exit angle α_f. The z-axis represents the the surface normal and consequently, the scattering plane is the (x-z) plane. The scattering outside this plane is probed under an out of plane angle ψ [129]. Assuming a monochromatic x-ray beam of wave-vector $\mathbf{k}_i$ ($|\mathbf{k}_i| = 2\pi/\lambda$) incident on the sample surface at an incident angle of α_i and scattered under an exit angle of α_f and an out of plane angle ψ, the scattering wave-vector q is defined by [129]

$$\mathbf{q} = \mathbf{k}_f - \mathbf{k}_i \qquad (2.23)$$

with the components given by

$$\begin{bmatrix} q_x \\ q_y \\ q_z \end{bmatrix} = 2\pi/\lambda \begin{bmatrix} \cos\psi\cos\alpha_f - \cos\alpha_i \\ \sin\psi\cos\alpha_f \\ \sin\alpha_i + \sin\alpha_f \end{bmatrix} \qquad (2.24)$$

For specular scattering ($\alpha_i = \alpha_f$) the scattering vector components are $q_x = q_y = 0$ and $q_z \neq 0$, sampling a depth sensitive information only. With off-specular or diffuse scattering ($\alpha_i \neq \alpha_f$) the lateral component $q_\parallel = (q_x, q_y) \neq 0$ probing the in plane structure of the sample surface. Commonly, the diffuse scattering is treated within the framework of distorted wave Born approximation (DWBA) [130]. In this framework, the scattering process is considered as a perturbation of an ideal system. The scattering cross section is determined using a first order perturbation theory, wherein smooth interfaces are used as ideal system and surface roughness and lateral structures are treated as perturbations. The differential scattering cross section is given by

$$\frac{d\sigma}{d\Omega} = \frac{C\pi^2}{\lambda^4}(1 - n^2)^2 |T_i|^2 |T_f|^2 F(\mathbf{q}) \propto F(\mathbf{q}) \qquad (2.25)$$

where C is the illuminated surface area, $T_{i,f}$ are the Fresnel transmission coefficients and F($\mathbf{q}$) the diffuse scattering factor [128]. The Fresnel's transmission coefficients have a maximum when the incident or the exit angle is equal to the critical angle of the
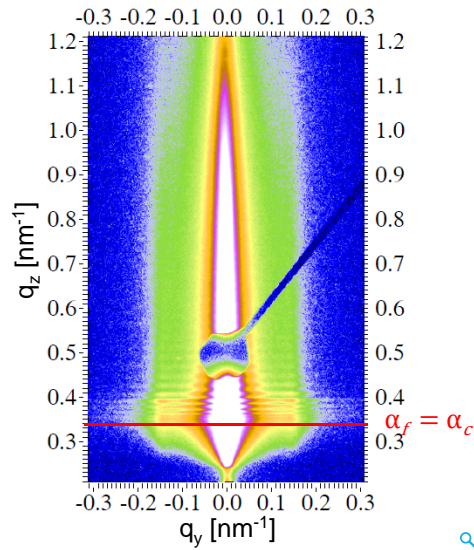
Figure 2.14: Example of a GISAXS pattern of the P3HT-b-PPerAcr 6 film measured at HASYLAB Hamburg. The profile cut along the q$_y$ axis at the fixed exit angle α_f ($\alpha_f = \alpha_c$) shown by the red line reveals information about the lateral structure

probed material. This maximum gives rise to the yoneda peak [131] in the scattered intensity which is material sensitive. The Fresnel's transmission coefficients act only as an overall scaling factor as α_i and α_f are fixed, the scattered intensity is directly proportional to the diffuse scattering factor [129].

In the grazing incidence small angle scattering, the small q_x component (along the direction of the incident beam) is neglected as the angles are typically very small. In the experimental set up, the angle of incidence was chosen such that complete penetration of x-rays occurs in the polymer layer in our samples i.e. α_c(polymer) $< \alpha_i < \alpha_c$(substrate). The experimentally measured angle are α_{inc}, γ and δ as shown in Figure 2.13(b). The transformation equations relating α_{inc}, γ and δ with α_i, α_f and ψ are given below.

$$\alpha_i = \alpha_{inc};\ \psi = \delta;\ \alpha_f = \gamma - \alpha_{inc} \tag{2.26}$$

Substituting α_i, ψ and α_f in equation (2.24) and neglecting q_x we get,

$$\begin{bmatrix} q_y \\ q_z \end{bmatrix} = 2\pi/\lambda \begin{bmatrix} \sin\delta\cos\gamma\cos\alpha_{inc} + \sin\delta\sin\gamma\sin\alpha_{inc} \\ \sin\alpha_{inc} + \sin\gamma\cos\alpha_{inc} - \sin\alpha_{inc}\cos\gamma \end{bmatrix} \tag{2.27}$$

If from the 2D GISAXS pattern selected cuts are taken, data have to be analyzed as a function of q_y for cuts at constant q_z (Figure 2.14), such a simplification is often referred to as effective surface approximation [129]. Thus, from these cuts only information about the lateral structures is extracted and no information about structures along the surface normal is obtained.
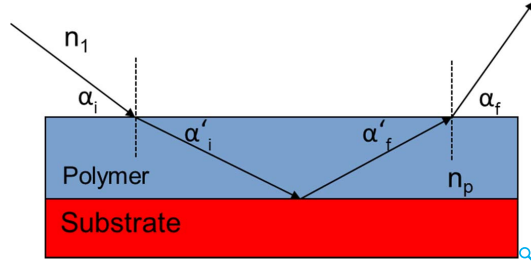
Figure 2.15: Ray diagram of the x-ray beam incident on the sample from vacuum at grazing incidence. The angle of incidence and the exit angle inside the sample is different from the experimentally measured angles and corrected by taking refraction effects into account

Grazing incidence wide angle scattering (GIWAXS)

The crystalline structure and orientation in thin films was investigated by GIWAXS. The set-up is equivalent to the GISAXS set-up (Figure 2.13(b)) with the only difference being a smaller sample to detector distance, thus, probing larger scattering angles as compared to GISAXS. The transformation equations used for the conversion of scattering data from pixels to reciprocal space map are same as used for GISAXS. However, the q_z component was modified to account for refraction effects [127]. Since the refractive index of material is less than unity, the incident and exit angles in the material are different than those in vacuum. Figure 2.15 gives a ray diagram of the incident and outgoing x-ray beam in grazing incidence geometry. Applying Snell's law (at the incident angle side) and the boundary conditions that the parallel components of the E field remain continuous at the interface, we get,

$$\sin(\pi/2 - \alpha_i) \cdot n_1 = \sin(\pi/2 - \alpha_i') \cdot n_p \Rightarrow \cos \alpha_i = n_p \cdot \cos \alpha_i' \qquad (2.28)$$

for total external reflection $\cos \alpha_c = n_p$, this gives

$$\cos \alpha_i' = \frac{\cos \alpha_i}{\cos \alpha_c} \qquad (2.29)$$

Similarly, applying Snell's law at the exit angle side we get

$$\cos \alpha_f' = \frac{\cos \alpha_f}{\cos \alpha_c} \qquad (2.30)$$

Thus, the modified transformation equations taking into account the refraction effects are given by equation (2.31)

$$\begin{bmatrix} q_x \\ q_y \\ q_z \end{bmatrix} = 2\pi/\lambda \begin{bmatrix} \cos\psi \cos\alpha_f - \cos\alpha_i \\ \sin\psi \cos\alpha_f \\ (\sin^2\alpha_i - \sin^2\alpha_c)^{1/2} + (\sin^2\alpha_f - \sin^2\alpha_c)^{1/2} \end{bmatrix} \qquad (2.31)$$

Again, α_i, α_f and ψ are converted in terms of the measured angles α_{inc}, γ and δ using equation (2.26) and substituted in equation (2.31).
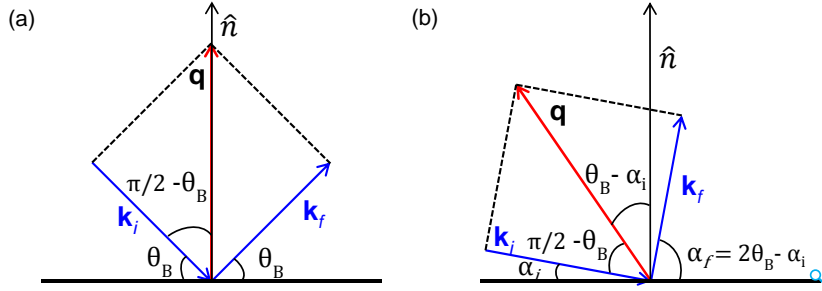
Figure 2.16: Schematic illustration of the scattering set up in (a) specular condition and (b) grazing incidence geometry. The substrate normal is denoted by $\hat{n}$

The scattering intensity is then plotted as a function of $q_{\parallel} = \sqrt{q_x^2 + q_y^2}$ and q_z. Due to the thin film geometry and interfacial effects, the polymer crystallites (investigated in this thesis) show preferential orientations. Consequently, the lattice planes oriented parallel and perpendicular to the substrate reveal Bragg reflections along the q_z and q_p respectively. However, in a GIWAXS measurement, as the angle of incidence is kept fixed, complete information about crystallite orientation from the lattice planes parallel to the substrate is not accessible. Figure 2.16 shows a comparative illustration of the different scattering geometry in specular and GIWAXS configuration ($\psi = 0$). In specular condition, the lattice planes with the scattering vector q parallel to the substrate normal $\hat{n}$ give rise to a reflection at the particular Bragg angle. On the other hand, in a GIWAXS geometry, due to a fixed angle of incidence, the most vertical orientation that will result in observed diffraction will be from the lattice planes tilted by an angle of (θ_B - α_i) from the substrate normal. Thus, in order to obtain complete information from the crystallites having lattice planes oriented parallel to the substrate normal, measurements in specular condition i.e. $\alpha_i = \alpha_f$ are necessary. A combination of measurements in GIWAXS and specular condition (pole figure analysis) [132] can provide complete quantitative information about the azimuthal distribution of a Bragg reflection. Preliminary results of the pole figure analysis are given in the appendix.

2.5 Charge carrier mobility determination by Space Charge Limited Current (SCLC) method

An important figure of merit in semiconductors is the charge carrier mobility. A simple way to determine the charge carrier mobility in organic semiconductors is called SCLC method. In this method, a material is sandwiched between two 'suitable' electrodes and charges are injected into it. If a quadratic relationship is observed between the measured dark current and the applied voltage i.e. space charge limited current (SCLC), the charge carrier mobility can be determined by fitting the measured IV characteristic curves against the SCLC relationship (equation(2.36)). This method determines charge carrier mobility of a single type of carriers only i.e. either electrons or holes in a vertical direction.
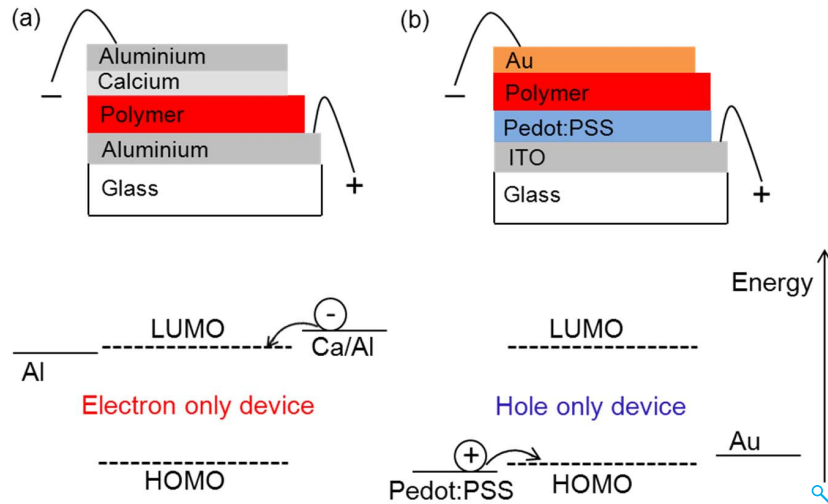
Figure 2.17: Schematic representation of SCLC (a) electron only and (b) hole only device for charge carrier mobility determination. The work function of the injecting electrode with respect to the HOMO/LUMO energy level of the material determines the type of the injected charge carriers [133]

The concept of space charge limited current (SCLC) was originally introduced by C.D.Child for the thermionic emission in vacuum tubes [134]. However, due to the ballistic nature (no scattering) of the space charge (in vacuum), no mobility dependent term is obtained in the j-V relationship. Later, Mott and Gurney [135] modified the Child's law for solid state semi-conductors. The charge carrier mobility of a single carrier in a device is determined by the movement/flow of injected charge carriers (either electrons or holes) into a semi-conducting material. The type of charge carriers injected into the material depends on the work function of the injecting electrodes. In an organic material, if the electrode work function is aligned with the HOMO (highest occupied molecular orbital) level, holes are injected. Correspondingly, if the work function is aligned with respect to the LUMO (lowest unoccupied molecular orbital) level, electrons are injected. Figure 2.17 shows a schematic of the SCLC electron and hole only devices with the corresponding work functions of the injecting electrodes with respect to the HOMO/LUMO energy levels in an organic semiconductor.

In a SCLC device, accumulation of injected charge carriers occur near the injecting electrode, in a low charge carrier mobility material, forming a space charge. Along the direction of the applied electric field E, the charges drift with an average speed, v_d = μE and limit the current flow across the electrodes. In the absence of any charge trapping, the space charge limited current j, as given by the Mott-Gurney equation, varies directly as the square of the applied voltage V and inversely with the cube of the thickness L of the semiconducting material. The application of the SCLC method for determining the charge carrier mobility requires the following conditions: (1) No barrier for charge injection i.e. the charge injecting electrodes must be ohmic, (2) the contacts must be chosen based on their energy levels to inject only single type of charge carriers (holes or electrons) and (3) the injected charge carrier density must be much greater than the intrinsic charge carrier density. A brief derivation of the Mott-Gurney

equation is given below.

Assuming that the diffusion current density is zero, the current density is given by the drift of the charge carriers under an applied field E

$$j = nev_d = ne\mu E \tag{2.32}$$

where n is the carrier density, e is the coulombic charge. According to Poisson's equation

$$\frac{\partial E}{\partial x} = \frac{ne}{\epsilon_r \epsilon_\circ} \Rightarrow n = \frac{1}{e\epsilon_r \epsilon_\circ} \cdot \frac{\partial E}{\partial x} \tag{2.33}$$

Substituting n in equation (2.32) and integrating once (assuming that $E = 0$ V/m at the injecting electrode i.e. at $x = 0$) we get

$$E = \sqrt{\frac{2jx}{\epsilon_r \epsilon_\circ \mu}} \tag{2.34}$$

The potential V across the device with an active layer length L is given by

$$V = \int_0^L E dx = \int_0^L \sqrt{\frac{2jx}{\epsilon_r \epsilon_\circ \mu}} dx = \frac{2}{3} \sqrt{\frac{2j}{\epsilon_r \epsilon_\circ \mu}} L^{3/2} \tag{2.35}$$

Rearranging we get,

$$j = \frac{9}{8} \epsilon_r \epsilon_\circ \mu \frac{V^2}{L^3} \tag{2.36}$$

Equation(2.36) gives the well known Mott-Gurney equation [135], where j is the current density, ϵ_r is the relative permittivity of the organic semiconductor, $\epsilon_\circ$ is the permittivity of free space, μ is the charge carrier mobility, L is the thickness of the active layer and V is the voltage drop across the device.

Another empirical formula often used to evaluate charge carrier mobilities in P3HT (equation(2.37)), was given by Murgatroyd [136], accounting for the field dependence of the charge carrier mobility. The field dependence on charge carrier mobility in P3HT have been explained within the framework of the Gaussian disorder models [137]. For a detailed theory of charge transport in disordered systems, the reader is directed to following references [137–139].

$$j = \frac{9}{8} \epsilon_r \epsilon_\circ \mu_h \, exp(0.89\xi\sqrt{E}) \, V^2/L^3 \tag{2.37}$$

where μ_h the zero field mobility of holes, ξ the field activation factor and $E = V/L$ the average electric field across the device

Chapter 3

Experimental methods

This chapter includes the technical details of the various experimental methods used in this thesis which include differential scanning calorimetry (DSC), transmission electron microscopy (TEM), x-ray scattering, grazing incidence x-ray scattering (GID) and atomic force microscopy (AFM).

3.1 Differential scanning calorimetry

Phase transitions are accompanied by liberation or absorption of heat resulting in a change of the physical state of the material. Calorimeters are one of the simplest tools to determine thermodynamical changes occurring in a material during a phase transition. Differential scanning calorimetry is a technique which provides qualitative and quantitative information about specific heat capacity, enthalpy and entropy of phase transitions and the kinetics of the processes. The working principle of differential scanning calorimetry (DSC) is the measurement of the differential heat flow rate to the sample with respect to a reference (normally an empty pan) upon application of a temperature program in form of temperature ramps. DSC instruments can be classified into two main categories on the basis of their functioning: (a) Heat flux DSC where, the measured signal Δ T (T_{sample}-$T_{reference}$) is proportional to the difference in the heat flow rate from the furnace to the sample and to the reference Δ ϕ (ϕ_{sample} -$\phi_{reference}$); and (b) Power compensation DSC where, the temperature difference Δ T is compensated by supplying additional electrical power. The additional power difference Δ P (P_{sample}-$P_{reference}$) is then assigned to the heat flow rate Δ ϕ. In this work, a power compensated DSC is used. A detailed description is given below.

The power compensated DSC operates in an isoperibolic mode i.e. the temperature of the sample surroundings is kept constant by an isolation jacket [140]. The calorimeter comprises of two identical micro-furnaces each equipped with a platinum temperature sensor and a heater, as shown in Figure 3.1. Both the micro-furnaces are situated in thermally decoupled aluminum blocks. The use of separate heaters allows the two furnaces to follow a given time-temperature program identically. In case of an ideal thermal symmetry between the two micro-furnaces, the same heating power is required to maintain the same temperature. An endothermic or exothermic process in the
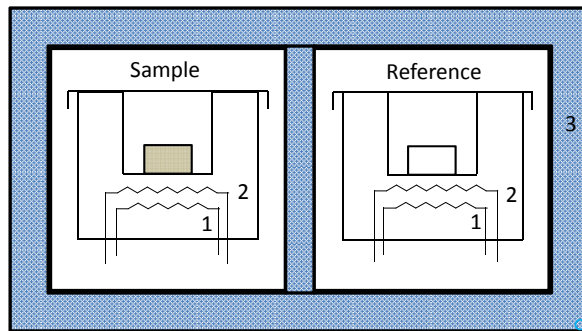
Figure 3.1: Schematic representation of a power compensation differential scanning calorimeter consisting of two identical micro furnaces containing (1) heater and (2) temperature sensor. The block (3) surrounding both microfurnaces is kept at a constant temperature T

sample results in a temperature difference thereby breaking the symmetry between the two micro-furnaces. The symmetry is restored by supplying additional power Δ P to the sample or reference micro-furnace. This compensating power Δ P supplied to achieve thermal symmetry of the two micro-furnaces is proportional to the heat flux consumed or produced by the sample. The output signal obtained is the heat flow rate $\Delta \phi$ (J/s) as a function of temperature. To evaluate the specific heat capacity of the sample as a function of temperature, the procedure undertaken is as follows: First, a temperature program for the heat flow rate measurement is defined such that an isothermal step is added before and after each heating and cooling step. The corresponding heat flow rate as a function of temperature is obtained for the sample. In the second step, the sample pan is removed and replaced by an empty aluminum pan with an approximately similar weight as that of the empty sample pan. The resulting heat flow rate from the empty pan measurement is then subtracted from the heat flow rate obtained from the sample measurement. The obtained heat flow rate is then divided by the scan rate (dT/dt) and the mass (m) of the sample resulting in the specific heat capacity of the sample as per equation (3.1)

$$c_p = \frac{\Delta\phi}{m \ (dT/dt)} \tag{3.1}$$

Figure 3.2 shows an example of the specific heat capacity curve measured during heating. The melting or crystallization temperatures from a DSC scan can be determined in two ways.
(i) Melting/crystallization temperature (T_m/T_c) is the peak maximum point of the endothermic/exothermic peak or
(ii) Onset melting/crystallization temperature determined from the intersection of the tangent drawn at the point of inflection and at the base of the peak [140]
In this thesis, the peak maximum temperature was chosen as the melting/crystallization temperature. The enthalpy of melting/crystallization (Δ H) is given by the area under the endothermic/exothermic peak in the c_p curve. DSC measurements were performed on Perkin Elmer DSC-7. The scan rate used was 10 K/min (both for heating
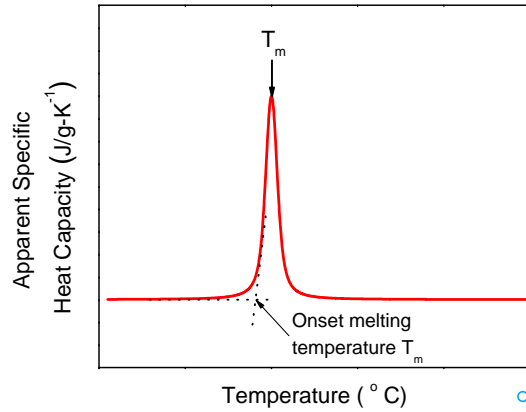
Figure 3.2: DSC data analysis of the melting peak and enthalpy

and cooling) unless otherwise stated. The first heating run for all samples was not considered to remove thermal history during the synthesis.

3.2 Transmission electron microscopy

Transmission electron microscopy (TEM) is an imaging technique where an electron beam is transmitted through an ultra-thin sample thereby interacting with the sample as it passes through. Owing to the small de-Broglie wavelength of electrons, the image resolution of a TEM is significantly higher than a normal light microscope and hence finds vast applications in the field of physical and biological sciences.
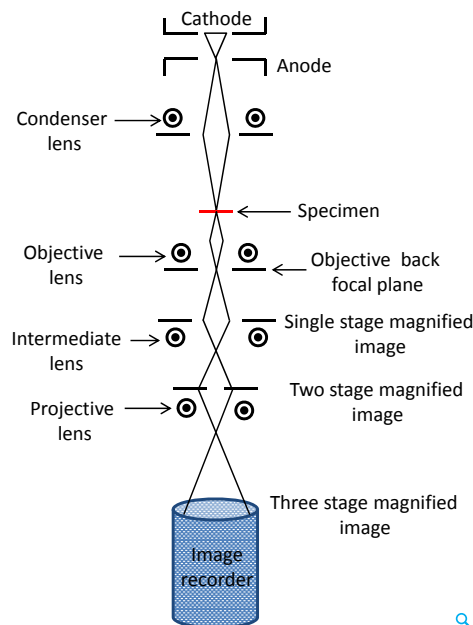

Figure 3.3: Schematic of a transmission electron microscope

The schematic of a transmission electron microscope is shown in Figure 3.3. The electrons generated at the cathode are accelerated by applying a high voltage via an anode. Focusing of the diverging beam of electrons on the sample is achieved using condenser lens assembly. The electron beam after passing through the sample is fed to an objective lens via an objective aperture forming a single stage magnified image. The selector aperture is located in the plane of the intermediate image. The intermediate image is magnified successively by the intermediate and the projector lens assembly. The resulting three stage magnified image can be captured using a digital camera, CCD or a fluorescent screen. For a detailed overview the reader is directed to the following reference [141].

The image contrast in a TEM can originate from various factors depending upon the mode of operation. The contrast can be produced by diffraction (between the crystalline and amorphous regions), absorption (by heavier elements or from thicker regions) or due to scattering. In general, polymers scatter electrons very weakly giving poor contrast in TEM [142]. The contrast in the block copolymers investigated in this thesis was produced by exposing the microtomed samples to the vapors of RuO_4 which selectively stains one block resulting in an enhanced contrast. TEM measurements on the block copolymers were made at University of Bayreuth by Melanie Förtsch on Zeiss 922 Omega and at Martin Luther University Halle by S. Göerlitz on JEOL 2100.

3.3 X-ray scattering

3.3.1 Rotating anode

The set-up of the rotating anode is shown in Figure 3.4. The assembly of the rotating anode consists of a cathode and an anode located in a high vacuum. Thermionically emitted electrons from the filament (cathode) are accelerated towards the anode.The electrons striking the anode target cause emission of x-rays. The x-ray emission spectra is a superposition of continuous radiation (also called Bremsstrahlung or white radiation) and characteristic x-rays of the target material.

In this work a copper target is used as an anode. In the usual operational mode, the tube voltage is kept at 40 kV by connecting the cathode to high negative voltage while the anode is connected to the ground potential. The resulting flow of electrons between the cathode and the anode is set by the tube current set at a default value of 60 mA. The heating of the filament is controlled by choosing a filament current of about 1 Amp. The filament is located in Wehnelt housing with an aperture for focusing the electron beam on a small surface area of the copper target. The dimension of the focal spot on the anode target is 0.2 mm x 2 mm. The heat generated at the focal spot is removed to avoid degradation of the target and is achieved by the constant rotation of the anode target. Additionally, the anode assembly is cooled with a water supply. A stable position of the focal spot on the target and a high vacuum is realized using a complex magnetic sealing. The rotating anode has two beryllium windows through which the x-rays can exit. In the laboratory set up, only one exit route for the x-rays was chosen using an externally controlled shutter while the other exit route was
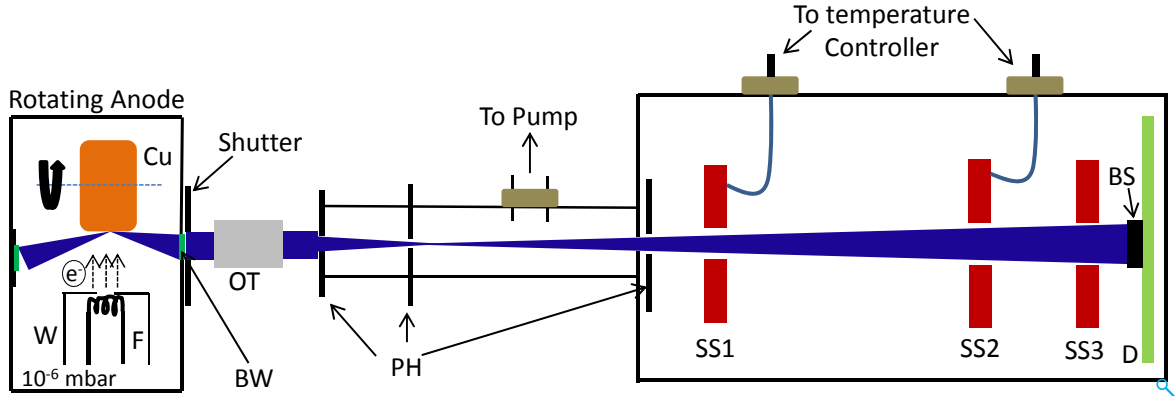
Figure 3.4: Schematic representation of rotating anode apparatus. The divergence of x-rays is shown in blue. The various components of the set-up are; (1) Cu: Copper anode, (2) F: Filament, (3) BW: Beryllium window,(4) OT: x-ray Optics, (5) PH: Pinholes assembly, (6) SS1, SS2, and SS3: Sample stages for small, intermediate and wide angle x-ray scattering respectively (7) BS: Beam stop, mounted on a crossed wire frame is placed in front of the detector (D) to block the direct beam

blocked. The x-rays, as shown in blue, are then fed to an evacuated x-ray optics device from Osmic (Confocal Max-Flux Optics). The x-ray optics consists of two mutually perpendicular multilayer mirror system and is placed such that one of its principal foci coincides with the focal spot of the anode. The thickness of the multilayers is designed such that it satisfies the Bragg condition of reflection for the Cu-k$_\alpha$ radiation only. Thus the usage of x-ray optics is two-fold. It focuses the x-ray beam and also acts as a monochromator. The resulting wavelength of the x-ray beam is 0.154 nm. The monochromatic x-ray beam from the x-ray optics is further collimated using a system of three pinholes. The first pinhole and the second pinholes have an aperture diameter of ≈400 microns and 200 microns respectively and are separated by a distance of about 69 cm. Such pinhole geometry limits the beam divergence. The third pinhole is located inside the sample chamber and has an aperture diameter of 700 microns. The third pinhole removes any parasitic radiation coming from the second pinhole. The pinhole panels and the sample stage are connected to each other by air pipes and evacuated by a vacuum pump to a pressure of 10^{-1} mbar.

The sample chamber consists of two motorized arms SS1 and SS2 (as shown in Figure 3.4) which can be moved vertically into the x-ray beam path. The position of the sample stages SS1 (for small angle x-ray scattering) and SS2 (for intermediate angle x-ray scattering) from the detector is 157 cm and 30 cm respectively. The combined scattering vector q range accessible (SS1 and SS2) was about q $\approx$ 6.5 nm^{-1}. Temperature dependent measurements were performed by mounting the samples on a hotstage from Linkam equipped with a Pt 100 temperature sensor. The hotstage was connected to a temperature control unit TMS 94 and an automatic cooling pump LNP 94/2 through the vacuum tight feedthrough. The temperature accuracy of the TMS 94 is 0.1°C. Liquid nitrogen was used for controlled cooling. Aluminium discs with a hole diameter of 0.8 mm were used as sample holders. Heat conducting paste was used to ensure good thermal contact between the hotstage and the sample holders. An

additional sample stage SS3 (c.f. Figure 3.4) was designed very close to the detector to probe structures corresponding to reciprocal scattering vectors up to ≈ 19 nm^{-1}. At this sample stage position no temperature dependent measurements were possible. The scattered intensity was measured with a Hi-Star area detector from Bruker. The detector consists of an x-ray proportional chamber with a precision, two dimensional multiwire grid; an integral amplifier; high resolution decoding electronics. The chamber is filled with a Xe/methane gas mixture. The scattered intensity is collected on a data frame 1024 x 1024 pixels with a pixel size of 105 microns. The scattering measurements obtained from different sample positions were calibrated using a standard silver behnate sample [40].

3.3.2   Magnetic field alignment

A special heating device, as shown in Figure 3.5, was constructed [143], which was used for performing crystallization, to obtain oriented samples in magnetic fields. The device consists of a brass cell which is heated by an electrical resistance heater and is connected to a thermal resistor (Macor) to a watercooled base plate. A PT 100 temperature sensor was used to measure the temperature. PID controller (Eurotherm) was used to control the temperature of the heating cell. The samples were placed in aluminum discs (same as used for x-ray scattering) which served as sample holders. The sample holders were then placed inside the brass cell. The heating device was flooded with nitrogen to provide an inert atmosphere in the heating chamber. The device assembly was inserted into a Bruker NMR magnet. The field strength of the magnet was 9.4 T. The samples crystallized in the magnetic field were then characterized for orientation using x-ray scattering at room temperature.
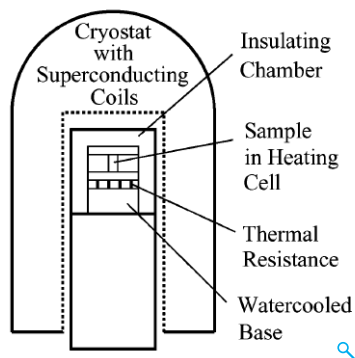

Figure 3.5: Schematic of the heating device used for orienting samples in the magnetic field [143]

3.3.3   Diffractometer

X-ray scattering measurements on thin films were performed on an Empyrean x-ray diffractometer from Panalytical (c.f. Figure 3.6). In Empyrean systems the goniometer is positioned vertically. The equatorial (or diffraction) plane (the plane set up by the
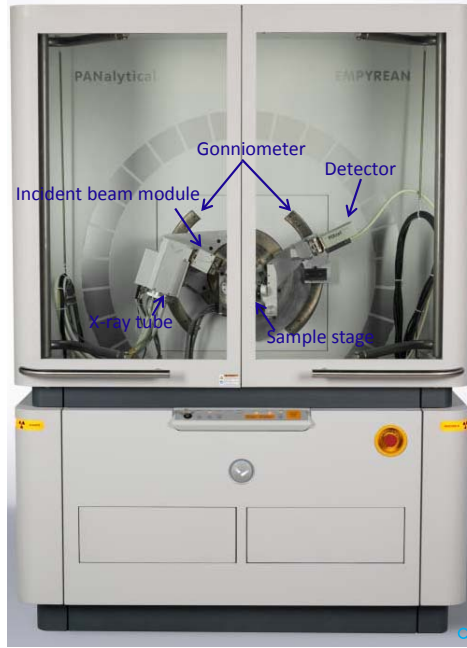
Figure 3.6: Empyrean x-ray diffractometer from Panalytical

incident and diffracted beams) is also vertical. The goniometer axes are placed horizontally. Empyrean systems are equipped with a PreFIX (pre-aligned fast interchangeable x-ray modules) stage interface for rapid exchange of sample stages without additional stage alignment. The x-ray tube used is a ceramic diffraction tube consisting of Cu anode. The operating tube voltage and current is kept at 40 kV and 40 mA respectively. The x-ray tube can be operated as a line or point focus. Using a line focus, the diffractometer can be operated in two different beam geometries namely: (1) divergent beam geometry (Bragg-Brentano) and (2) parallel beam geometry. Various prefix modules are available (for both incident and diffracted beam side) to achieve these two geometrical setups. These include programmable divergent slits, hybrid monochromator and a graded multilayer mirror for the incident side; programmable anti-scatter slit and a parallel plate collimator for the diffracted side. While the programmable divergent slits and anti scatter slits are used for the divergent beam geometry; parallel beam geometry is realized by using the hybrid monochromator or the multilayer mirror with a parallel plate collimator. On the diffracted side, the modules are coupled with a position sensitive PIXEL detector with an active channel length of 14 mm. Additionally, fixed beam masks and soller slits are used to control the width and the axial divergence of the x-ray beam respectively. Nickel filters are used to suppress the Cu-k_β component. The sample stage is a motor controlled 3 axis (ϕ, χ, z) Eulerian cradle fixed to the frame of the goniometer and does not rotate around the ω axis. A schematic of the position of the x-ray source, prefix modules along with the sample stage as used in a parallel beam geometry is shown in Figure 3.7.

θ-2θ scans on thin film samples covering a large angular range (2θ from $2°$-$30°$) used in this thesis were performed in parallel beam geometry. The advantage of using

parallel beam geometry for thin film measurements lies in the fact that it gives low background signal from the substrate and is less sensitive to misalignment of height and tilt of the sample. The parallel beam geometry was realized by using the hybrid monochromator and parallel plate collimator coupled with the detector operating in open detector configuration (active channel length 14 mm). The hybrid monochromator consists of a parabolic shaped graded multilayer mirror and special channel cut 2 x (220) germanium crystals. The x-ray mirror pre-collimates the divergent beam from the x-ray source to a quasi-parallel beam. This quasi parallel beam is monochromatized to the Cu-k_α spectral component ($\lambda = 0.154$ nm) by the monochromator crystals. The Cu-k_β spectral component is virtually eliminated. A divergence slit of 1/2° was used to control the illuminated length of x-ray on the sample. The alignment for the height and tilt of the sample was done as described in the section for reflectivity measurements.
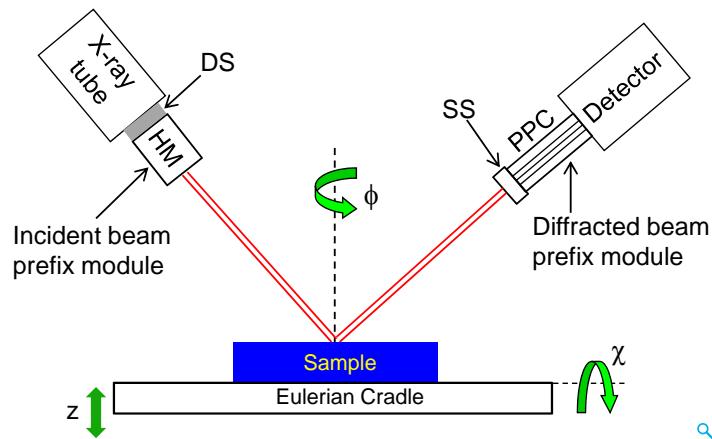

Figure 3.7: Exemplary illustration of the position of various components on the diffractometer in parallel beam geometry setup. The x-ray source is coupled with the incident beam prefix module (a hybrid monochromator; HM). The diffracted beam prefix module (parallel plate collimator; PPC) is coupled to the detector. Both the x-ray source and the detector are attached to the incident and diffracted arm of the goniometer. The other components: Soller slits (SS), the divergence slits (DS) and the cradle are also shown

Reflectivity measurements on thin films were also performed in the parallel beam geometry using a graded multilayer mirror (wavelength 0.154 nm) using 1/32° fixed divergence slit. A programmable beam attenuator was used. It consists of a nickel foil of thickness 0.125 mm (attenuation factor 200) that can be switched in and out at predefined intensity. The output signal is multiplied by the attenuation factor by the software. Soller slits with an angular opening of 0.04 radians were used on the incident and diffracted beam path. A fixed mask of 2 mm was used. The scattered signal was collected by the detector in the scanning mode with an active channel length of 1.05 mm. To determine the thickness of the films, reflectivity curves were fitted using the software program (X'Pert Reflectivity), based on Paratt algorithm, by Panalytical. Since reflectivity measurements are done at very small angle of incidence, it is very sensitive to the height and tilt of the sample. The sample alignment was done as described below.

(i) First the sample stage is moved out of the x-ray beam path. Calibration of the beam position is done by performing a 2θ scan. The center of the resulting beam profile is then chosen as the zero position. This procedure sets the fine calibration offset in 2θ of the primary beam position.

(ii) The height alignment of the sample is done by performing a z scan. It gives a similar profile as shown in Figure 3.10(a). The height of the sample is then given by the z corresponding to half the intensity of the direct beam.

(iii) The inclination of the sample in the beam direction is corrected by performing ω scans. The peak position of the resulting profile is set as zero position and subsequently defines the fine calibration offset for ω. The steps described in (ii) and (iii) are repeated until steady state values are reached.

(iv) Subsequently χ scans are performed to correct for the tilt of the sample. The peak position of the resulting profile is set as the zero position and defines the sample offset.
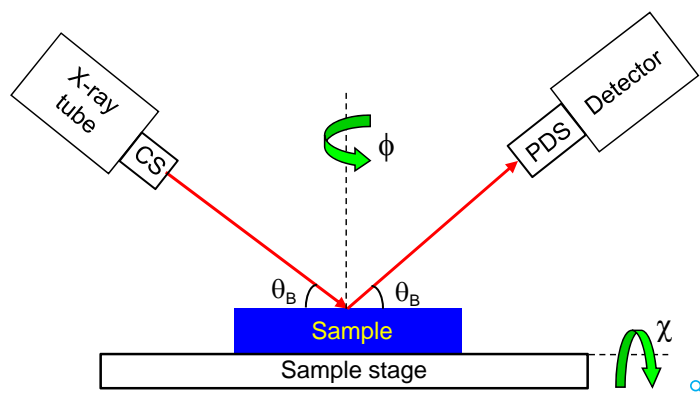
3.3.4   Texture measurements

Figure 3.8:   Schematic of the texture measurement setup showing the x-ray source (point focus), crossed slit collimator (CS), sample stage, programmable divergence anti-scatter slit (PDS) and the detector. The source and the detector were kept at a fixed position corresponding to the Bragg reflection

Texture measurements were also performed on an EMPYREAN diffractometer. The texture set up in reflection geometry [144] is shown in Figure 3.8. In this geometry, a point focus x-ray source is used in place of the conventional line focus. The incident beam prefix module consists of a crossed slit collimator with two manually adjustable orthogonal slits to define both axial and equatorial divergence of the x-ray beam. The crossed slit collimator is used to define the irradiated area on the sample. The sample stage used for performing the texture measurements is the same, 3 axis Eulerian cradle, as used for θ-2θ measurements. The height alignment of the sample was done using a dial guage. Texture measurements were performed in point focus geometry using a combination of crossed slits (aperture openings 0.2 mm x 1 mm) and a programmable anti scatter slit with a fixed divergence of 0.5° coupled with a position sensitive PIXEL detector. The wavelength used is 0.154 nm. Large nickel filter is used to suppress the

Cu-k_β radiation. Texture measurements were performed at a fixed angle of incidence and for a fixed detector position, corresponding to the dominant Bragg reflection as obtained from θ-2θ scan. The polar angle χ, was varied from 0° to 60° . For each χ, the azimuthal angle ϕ was scanned over 360°. While generally in a texture measurement, the intensity of a given Bragg reflection can depend on the angles ϕ and χ, the microstructure of the thin film samples is isotropic in the plane of the substrate. The measured ϕ dependence reflects only the outer shape of the films, which results from the casting process and finite size effects. Thus, for the analysis only the azimuthally averaged integrated intensity I(χ) were considered.

$$I(\chi) = \int_{\chi=constant} (I(\chi, \phi) \, d\phi \tag{3.2}$$

The intensity I(χ) is directly proportional to the orientation distribution of the crystals. FWHM of the peaks around $\chi = 0°$ was used as a quantitative measure. The integrated intensity I_{int} after background correction as defined in equation (3.3) is proportional to the crystallinity of the sample.

$$I_{int} = \oint (I(\chi) - I_{Bkg}) \, sin(\chi) \, d\chi \tag{3.3}$$

3.4 Grazing incidence x-ray scattering
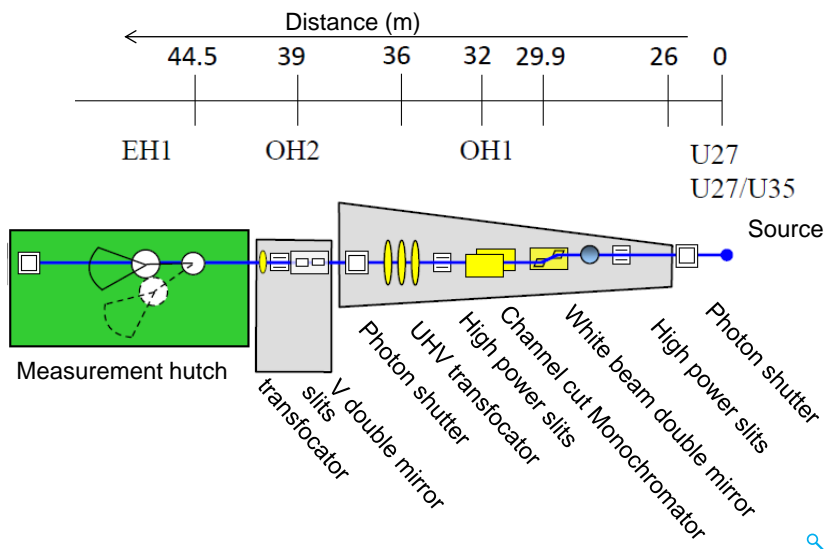
3.4.1 GISAXS

Figure 3.9: Schematic of the ID10 beamline at ESRF [145]. The various components of the beamline are shown. The measurement hutch contains the sample stage, the detector and the piezo driven guard slits besides various other components
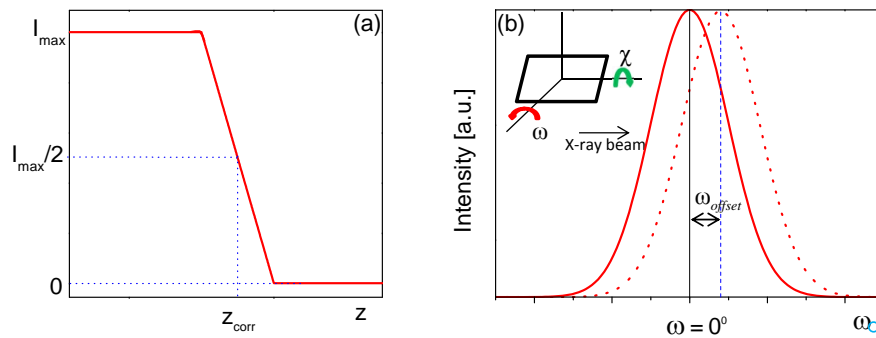
Figure 3.10: Alignment of the sample for correct height and tilt of the sample with respect to the direct beam

Figure 3.9 shows the schematic of the major components installed along the recently upgraded beam line ID 10 at ESRF synchrotron facility. The wavelength of the x-ray beam was 0.155 nm using a channel cut crystal monochromator with Si(111) crystal. The x-ray beam is focused horizontally and vertically using fixed Si/Pd/PT double mirrors. The ultra high vacuum (UHV) transfocator consists of an assembly of beryllium compound refractive lens which micro-focuses the beam to a spot size of 300 μm x 15 μm on the sample. The piezodriven guard slits just before the sample removes any parasitic signal enhancing the signal to noise ratio. Thin film samples prepared on Si substrates (15 mm x 15 mm) were placed on an horizontal sample stage (Huber 5202) and measured in air. The scattered data were recorded using a Pilatus 300k detector (619 x 487 pixels), with a pixel size of 172 μm. The direct and the specular beams were blocked using a beam stop to avoid detector saturation. An angle of incidence of 0.17°, which is slightly above the critical angle of the organic films and below the critical angle of the substrate, was chosen by tilting the sample along the beam direction. The sample to detector distance was kept at 81.9 cm

Sample Alignment: For the alignment procedure first, the CCD detector and the beam stops are completely moved out of the direct beam path. A diode beam stop is inserted to record the direct beam intensity. Thereafter z scans (for correct sample height) are performed. Figure 3.10(a) shows the intensity profile of such a z scan. When the sample is too low, full beam intensity is recorded. As the sample is moved into the beam the intensity begins to drop and reaches zero when the sample completely blocks the path of the direct beam. At this point, height of the sample corresponding to half intensity of the full beam is chosen as the correct height of the sample and is subsequently moved to this position. Thereafter, ω scans were performed to correct for any inclination of the sample with respect to the direct beam. The profile of an omega scan is shown in Figure 3.10(b). A misaligned sample will have a peak shifted from $\omega=0°$. The peak position of the ω scan is then given as an offset value (negative or positive) to the motor position and is set as zero. This procedure is repeated iteratively till steady state values are achieved. An incident angle of 0.5° was provided by tilting the sample with respect to the direct beam. An additional ω scan was performed at this incident angle followed by a z scan. No alignment of the sample was done for the

other angular tilt. After the completion of the alignment procedure the diode beam stop is taken out and the CCD detector is moved in. The desired angle of incidence was provided by tilting the sample with respect to the direct beam.

3.4.2 GIWAXS

The GIWAXS measurements at the ID10 beamline were performed with the same detector, wavelength and focusing set up as described in the GISAXS section above. The sample to detector distance was kept at 29.3 cm. The alignment of the sample was done as described in the previous section for GISAXS. The complete GISAXS signal was blocked using a rod like beam stop. The angle of incidence was kept at 0.17°. GISAXS/GIWAXS data obtained as a 2D image (in pixels) were first converted to an ASCII file using the Fit2D program. Programming in Matlab was done to transform the data from pixels to reciprocal space as described in section 2.4.2.

Further, GIWAXS measurements were also performed at the beamline ID10B at the ESRF synchrotron facility. An x-ray beam with a wavelength of 0.155 nm and a small bandwidth $\Delta E/E = 6.1 \times 10^{-5}$ (diamond (111) monochromator) was used. The beam was collimated using a combination of a horizontal and vertical slit, resulting in a beam size of 2 mm x 0.15 mm. An incidence angle $\alpha_{inc} = 0.18°$ was chosen. 2D scattering patterns were recorded by scanning a 1D vertical detector VANTEC located at a distance of 30 cm from the sample. Data conversion from pixels to reciprocal vector q was performed using the transformation equations as described in section 2.4.2 using the MatSpecGui program (ESRF). The resulting ACII data files of the reciprocal vectors were then plotted in Matlab to obtain the reciprocal space maps.
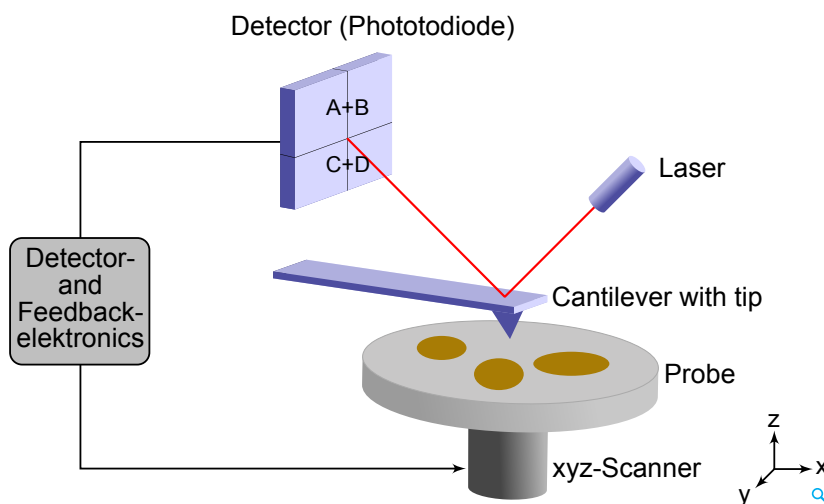
3.5 Atomic force microscopy

Figure 3.11: Atomic force microscope [146]

The fundamental principle of an atomic force microscope (AFM) involves the force interaction between a tip and the sample surface. Figure 3.11 shows the essential elements of an atomic force microscope. These include a micro-fabricated cantilever to support the tip, a system for detecting cantilever deflection with a feedback loop, and a scanner to control the relative position of the tip and specimen. The tip, in general, has a conical or pyramidal shape with a radius of curvature of a few nanometers. A laser beam is focused on the back side of the cantilever. The rear side of the cantilever is usually coated with a thin metallic layer to enhance reflectivity of the laser light. The reflected beam is projected onto a position-sensitive photo detector which is usually a split (quadrant) photodiode. The differential currents of the individual segments give a measure of the cantilever deflection. In order to acquire the image of a surface profile, the cantilever is moved line-wise over the sample area. Atomic force microscopy can be performed in two different operational modes viz. static mode and the dynamic mode. For investigating soft matter, the dynamic mode is preferred.
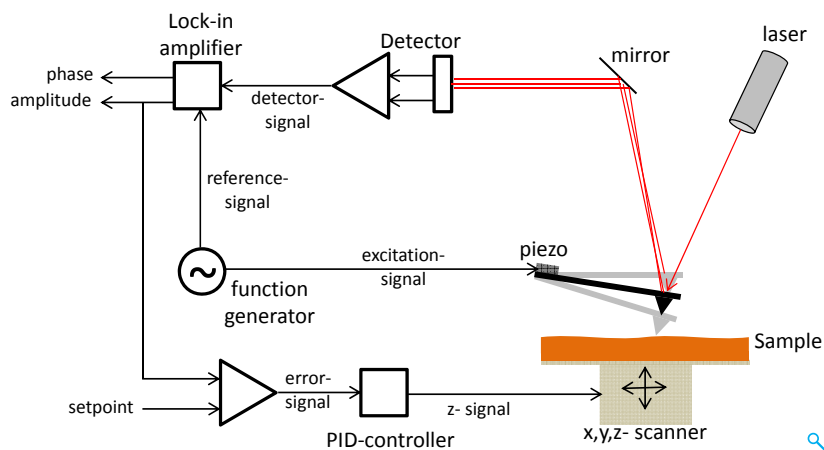

Figure 3.12: Schematic of an atomic force microscope in intermittent contact mode [147]

AFM measurements in this thesis were performed using intermittent contact mode (or tapping mode or amplitude modulation mode) as shown in Figure 3.12. In this mode the cantilever is excited externally (using an additional piezoelectric element) at a constant oscillation frequency close to its resonance [147]. When the tip is approached into the proximity of the sample, changes in resonance frequency cause changes in the amplitude and phase of the oscillation. The oscillation amplitude and the phase, detected with the photodiode are analyzed with a lock in amplifier. The oscillation amplitude and the phase of the probe are monitored as the tip approaches the surface. This can be observed from the force distance curve which also indicates the sharpness of the tip. For imaging, initially a set-point amplitude is defined which is smaller than the free oscillation amplitude. The detected amplitude is compared to the set-point amplitude, and the difference or error signal is used to adjust z- piezo i.e. the probe-sample distance. The displacement of the piezo device in z direction determines the height image. Additionally, the phase shift between the excited and the measured signal gives information about the mechanical properties of the sample. While a higher phase

reflects harder part, a lower phase corresponds to a softer part [148]. The mathematical description of cantilever dynamics using harmonics model are descried elsewhere [148].

Atomic force microscopy measurements were performed with a Nano Wizard I from JPK Instruments (Berlin, Germany) using single crystal N-type cantilever tips from NT-MDT having a resonant frequency between 240 and 440 kHz with a force constant of 22-100 N/m. The operating frequency was kept at $\omega_{op} = 0.995\,\omega_{\circ}$ and the amplitude set point at a ratio of 0.8 with respect to the free oscillating amplitude. The phase difference was set to zero at operating frequency in absence of tip-sample interaction.

Chapter 4

Investigation of structural order in conjugated P3HT thin films

The morphology of a semi-crystalline semiconducting polymer consists of crystalline domains and disordered (amorphous) regions. The microstructure of such a semi-crystalline polymer plays a critical role on its charge transport properties. While the crystalline regions are expected to be beneficial for efficient charge movement, the disordered regions between the crystallites can pose significant barriers to transport. Among various semi-crystalline organic materials, the solution processable hole-transporting conjugated polymer poly(3-hexylthiophene) (P3HT) has been investigated intensively and paved the way to basic understanding of charge transport properties in conjugated polymeric materials. Thin films of P3HT were demonstrated to adopt highly crystalline and anisotropic microstructures resulting in high charge carrier mobilities of up to - 0.1 cm^2/(V·s) in organic field effect transistor (OFET) devices [35]. The observed microstructure and associated crystallinity are also shown to be a function of regioregularity, molecular weight (MW) and film preparation conditions [58,69,149,150]. Apart from transistor applications, a very good light absorption, air-stability and suitable energy levels make P3HT the most often investigated material in polymer photovoltaics today [151].

Unlike in transistors, where the influence of morphology and molecular weight on charge transport at the dielectric interface is studied extensively [5, 37, 150, 152, 153], a detailed study of structure-property-relations for vertical charge transport (as used in photovoltaics) in P3HT is still missing. One such method for mobility determination is the space charge carrier limited current (SCLC), which measures the bulk transport properties of thin films. Among various processing conditions (e.g. casting conditions, surface treatments, epitaxy, solvent and thermal annealing) [82, 154, 155], thermal annealing is commonly employed in order to induce crystallization and to alter the morphology in semi-crystalline polymer thin films [17]. During this treatment, films are heated and annealed at an elevated temperature (usually above the glass transition temperature but below the melting temperature) resulting in crystallization either during the heating or the annealing process due to an increased molecular mobility [156]. On the other hand, crystallization from the molten state is more defined as it involves

crystallization from an equilibrium state (liquid like) removing any pre-history of crystallites during the thermal treatment. The full potential of this thermal annealing step (crystallization from melt) on the microstructure and charge transport properties (in diode configuration) in semi-crystalline P3HT thin films has not yet been investigated. In this chapter, we aim to develop a thorough understanding of how thermal annealing (crystallization from melt) affects the microstructure of thin films of P3HT and, in turn, how the microstructure is related to the electronic properties. The study aims to provide an insight to the following questions:

(1) What is the effect of crystalline order in polymer films and its importance with respect to the charge transport? Are other microstructural details, such as crystallite orientation important too?

(2) Is there an influence of the semi-crystalline morphology (lamellar periodicity/long period) on the transport properties?

The structure and charge transport in as-cast and melt-crystallized P3HT films is investigated systematically for highly regioregular (≈ 97 %) P3HT of different molecular weights, with M_n ranging between 3 kg/mol and 24 kg/mol. A comprehensive understanding of the microstructural properties and device behavior of both as-cast and melt-crystallized films was achieved by XRD, AFM, UV-vis spectroscopy and SCLC. Crystallization by cooling from the melt led to a substantial increase in crystalline order and a stronger alignment of the crystals in comparison to as-cast films. The charge carrier mobility in P3HT films was found to be correlated with the increased crystalline order and the long period.[1]

4.1 Materials and sample preparation
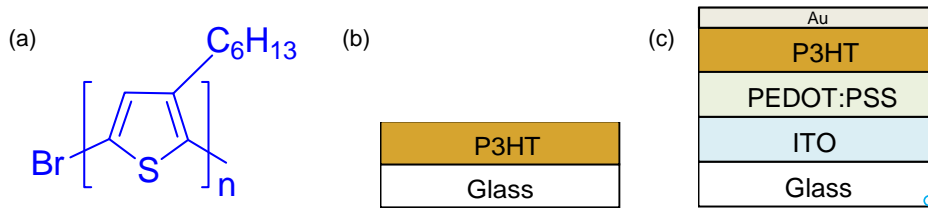
4.1.1 Materials

Figure 4.1: (a) Chemical structure of P3HT; (b) P3HT active layer on glass substrate used for structural investigations; (c) device structure used for SCLC mobility measurements

Regioregular P3HT samples were synthesized using the Grignard metathesis polymerization developed by McCullough and co-workers, described elsewhere in detail [158]. The molecular weights and the polydispersities (PDIs) were determined by gel permeation chromatography (GPC) in tetrahydrofuran (THF) with polystyrene as calibration standard. The number average molecular weight (M_n), PDI and melting tem-

---

[1]The results of this work were published in [157]

Table 4.1: Material properties of highly regioregular P3HT samples of different molecular weight

P3HT		P3HT 3	P3HT 7	P3HT 12	P3HT 18	P3HT 24
Mol wt M_n	MALDI	3.2	7	12.4	17.6	24
(kg/mol)	GPC	5.2	10.2	18.5	27.2	34.2
Repeating units		20	42	74	106	144
PDI (GPC)		1.15	1.15	1.16	1.16	1.15
T_m (°C) [73]		172	225	230	238	242

peratures are summarized in Table 4.1. The number average molecular weights were also determined on an absolute scale by matrix assisted laser desorption/ionization mass spectroscopy (MALDI-TOF MS) with time-of-flight detection. The number of repeat units of thiophene was calculated by dividing the MALDI molecular weight M_n by the monomeric molecular weight of P3HT M_o (M_o = 166 g/mol). Within this chapter, the different P3HT's are referred to by their MALDI molecular weights.[2]

4.1.2 Thin films for structural characterization

Thin films of P3HT for structural investigations were spin-cast on glass substrates. The glass substrates were cleaned by ultrasonicating them in acetone and isopropanol respectively for 10 min, and were dried. Thin films of about 300 nm thickness of P3HT samples of different molecular weights were spin cast from a 2 wt% of chloroform solution with a rotational speed of 450 rpm. These films were then kept in a vacuum oven overnight at room temperature. Subsequently the set of films were heated to 10 °C above the respective P3HT melting temperature and slowly cooled down (5 K/min) to room temperature. The thermal treatment was performed in an inert nitrogen atmosphere. The film thickness of different molecular weight P3HT films was determined by scratching the films and making a topographic scan with atomic force microscope (Figure 4.2).

4.1.3 Single carrier space charge limited devices

Single carrier SCLC devices in diode configuration were prepared for charge carrier mobility determination using a stack of glass/ITO/PEDOT:PSS/P3HT/Au (Figure 4.1(c)). The ITO coated glass substrates were first cleaned by toluene, acetone and isopropanol. A layer of PEDOT:PSS (30 nm) was spin coated onto the substrates. After drying the PEDOT:PSS for 15 min at a temperature of 180 °C, an approximately 300 nm thick layer of P3HT was spin-cast on top of this layer under inert conditions. The same thermal treatment was applied to all the films as done for the structural investigations. The top Au electrodes were thermally evaporated onto the polymer layer under

---

[2]Synthesis of various P3HT samples was done by R. Lohwasser (Univ. Bayreuth). SAXS on bulk samples were performed by J. Balko (MLU Halle). SCLC and optical absorption was done by C. R. Singh (TU Ilmenau)
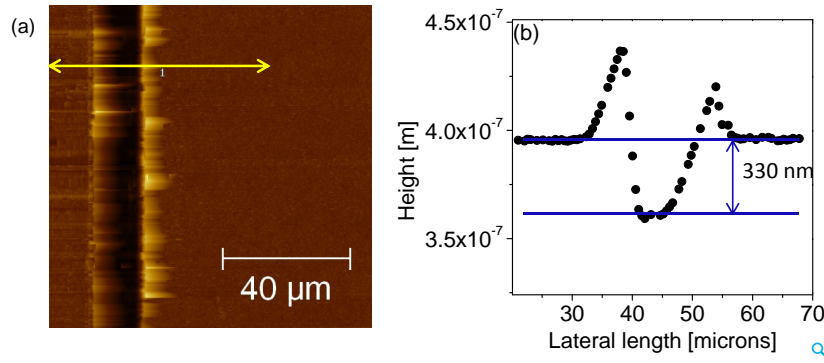
Figure 4.2: (a) Topographic AFM image of a scratched P3HT 12 film as a representative for the measurement of film thickness; (b) Profile scan of the scratch showing a film thickness of ≈ 330 nm
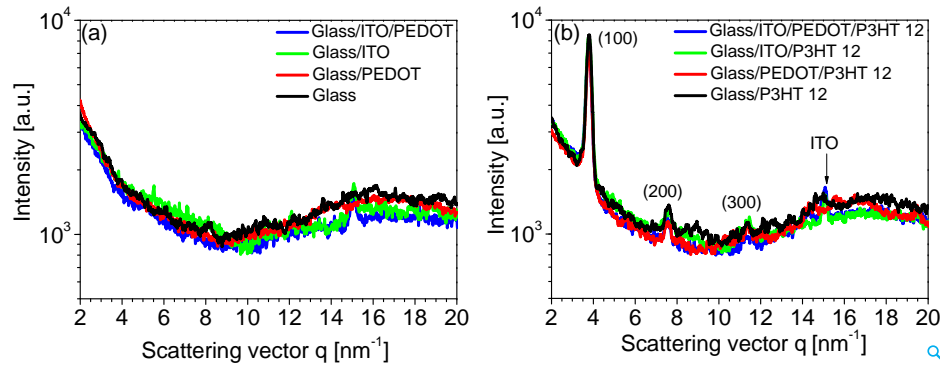

Figure 4.3: (a) θ-2θ scans performed on different glass substrates. A peak corresponding to ITO is observed at a scattering vector q = 15 nm^{-1} on glass substrates coated with ITO layer. (b) θ-2θ scans of melt-crystallized P3HT 12 on different glass substrates exhibits a similar scattering pattern suggesting a same structure and orientation

high vacuum conditions defining an active area of 0.16 cm^2 for a single SCLC device. The devices were completed by an epoxy resin based glass encapsulation under inert environment. The devices were characterized in the dark at room temperature with a Keithley 2400 unit. Because of the symmetrical work function electrodes in this hole-only device, a built-in voltage (V_{bi}) close to 0 V was assumed in fitting measured IV characteristics. The series resistance was determined from the reference devices fabricated without the P3HT layer. Both the V_{bi} and the voltage drop (IR) over the series resistance were subtracted prior to fitting the measured IV characteristics using the Murgatroyd SCLC relationship (equation (2.37)) for mobility determination [136]. Since the PEDOT:PSS electrode degraded upon the high temperature (240 °C - 250 °C) [159] treatment during melt crystallization, only reverse bias IV characteristics were used for mobility evaluation. In this case the hole injection took place from the stable Au electrode. X-ray diffraction measurements were done to check that the different substrates do not induce different structures in P3HT (Figure 4.3).

4.2 Structural characterization

4.2.1 Optical absorption

The absorbance spectra of as-cast and melt-crystallized P3HT films are shown in Figure 4.4. Already in as-cast films, the vibronic peak located at 615 nm indicates the presence of an ordered phase [13]. However, the spectrum of the lowest MW sample was blue shifted in comparison to higher MW samples. Zen et al. have also reported similar blue shift in as-cast low MW films and have reported it to be due to the backbone conformation/twisting of low MW polymers [149]. In addition to that Kline et al. related the blue shift with finite size confinement effects of the small molecules [37]. Whereas, the higher molecular weight samples exhibited a slight red shift of the total absorption spectrum upon melt crystallization, the lowest MW sample (P3HT 3, black line) continued to possess a pronounced absorption in the higher energy range which can be attributed to the amorphous fraction of the material [160]. Nevertheless, the observed enhancement of the vibronic peak at 615 nm in melt-crystallized films throughout all MWs evidenced an increased crystalline order as compared to as-cast films.
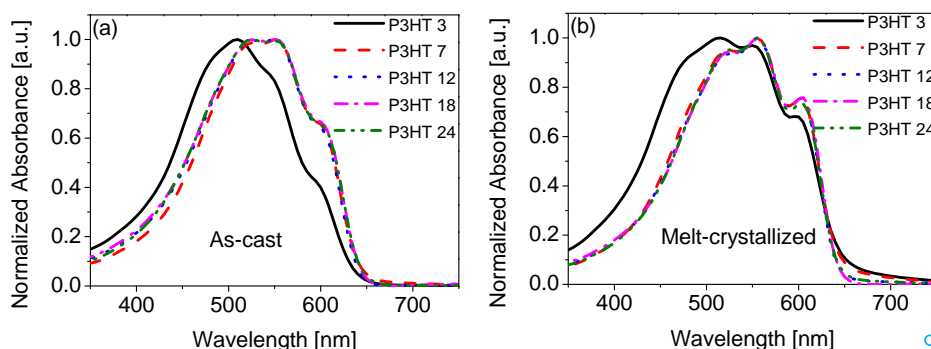

Figure 4.4: UV-vis spectra of (a) as-cast and (b) melt-crystallized P3HT films. Increased crystallinity after melt crystallization is evident from the enhanced vibronic peak at 615 nm for all P3HT samples.

4.2.2 X-ray scattering

For a detailed analysis of the structural differences between the as-cast and melt-crystallized films, x-ray scattering combining θ-2θ scans and texture measurements in reflection geometry was used. Figure 4.5(a) shows the result of two θ-2θ scans of the as-cast and melt-crystallized films for the P3HT 12 sample as a representative example. The (100) reflection corresponding to the distance between the P3HT main-chain is observed at a scattering vector q $\approx$ 3.77 nm^{-1} for both as-cast and melt-crystallized films. The spacing between the main chains corresponding to this reflection is calculated to be d = 2π/q = 1.67 nm. No higher order reflections corresponding to (*h00*) planes are observed in as-cast films. A broad halo around q = 16 nm^{-1} originates from the glass
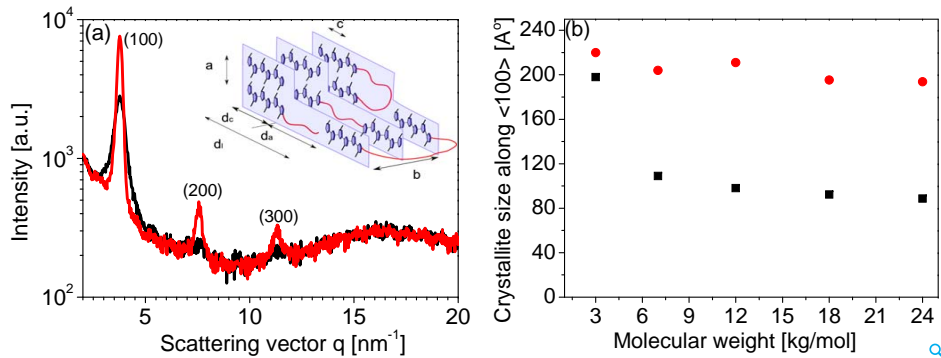
Figure 4.5: (a) θ-2θ scans of P3HT 12 of as-cast (black) and melt-crystallized (red) films. The inset shows a schematic of the typical microstructure of regioregular P3HT. a, b, c denote the crystal lattice parameters; d_c thickness of lamellar crystal; d_a thickness of the amorphous layer; $d_l = d_c + d_a$ gives the long period of the semi-crystalline morphology, which is an order of magnitude larger than the crystal lattice parameters [73]. (b) Crystal size calculated using equation 1 for as-cast (black square) and melt-crystallized (red circle) films

substrate. However, upon melt crystallization all molecular weight P3HT films exhibited reflections upto the third order. In both cases i.e. as-cast and melt-crystallized, no (020) reflection (corresponding to the π-π stacking distance) at a scattering vector q $\approx$16.4 nm^{-1} is observed. The (100) reflection strongly increases after crystallization from the melt and shows a reduced width. While the reduced width indicates an increased crystal size (t_{hkl}) in the direction perpendicular to the substrate which can be evaluated quantitatively using the Scherrer equation, the increase in intensity can either be caused by an increased crystallinity, or by a narrower orientation distribution with a prevalent orientation of the (100) lattice planes parallel to the substrate, or by both. Equation 4.1 gives the Scherrer equation, where λ is the wavelength used, θ_{hkl} corresponds to the Bragg angle and β is the full width half maximum (FWHM) in radians [161].

$$t_{hkl} = \frac{0.9\,\lambda}{\beta\,\cos\theta_{hkl}} \tag{4.1}$$

The resulting values of the crystal size along the (100) direction are shown in Figure 4.5(b). The crystal size increased generally by a factor of almost 2 to about 20 nm after crystallization from the melt, except for the lowest molecular weight P3HT sample (P3HT 3) which shows a correlation length of $\approx$ 20 nm in the as-cast films. This implies that single crystalline domains do not span over the whole film depth from the substrate to the air interface.

In a θ-2θ scan, only lattice planes having their normal vector parallel to the substrate normal contribute to the scattering signal. Thus, information about the orientation distribution in a crystalline material cannot be deduced from the conventional θ-2θ scan alone. To compare the orientation distribution of the crystalline part after melt crystallization, texture measurements were performed. Typically, for P3HT an orientation of the a-axis perpendicular to the substrate is observed for highly regioregular semi-crystalline P3HT on Si/Glass substrate [58,83]. This was also illustrated from the
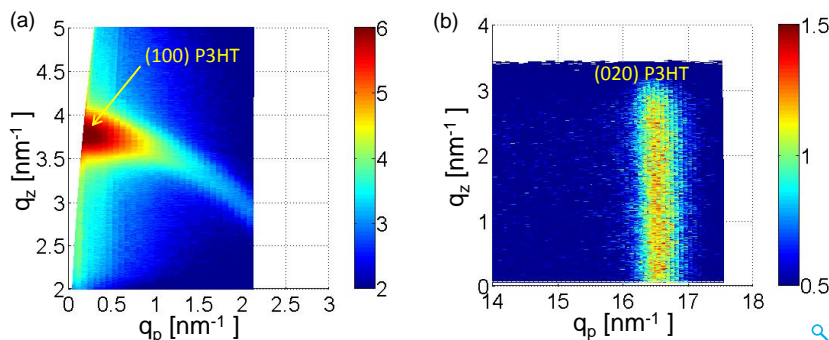
Figure 4.6: GIWAXS pattern of P3HT 12 films crystallized from melt on Si substrate. (a) The (100) reflection corresponding to stacking distance between the main chain and side chain exhibits an intensity maximum close to the q_z axis (b) The (020) reflection corresponding to the π-π stacking is observed along the q_p axis at $q_z \approx 16.6$ nm^{-1}

GIWAXS scattering pattern of the melt-crystallized film of P3HT 12 (Figure 4.6) where the (100) reflection shows an intensity maximum close to the meridian (i.e. along the q_z axis at $q_z \approx 3.8$ nm^{-1}) while the (020) reflection corresponding to the π-π stacking was observed along the q_p axis at $q_p \approx 16.5$ nm^{-1}.
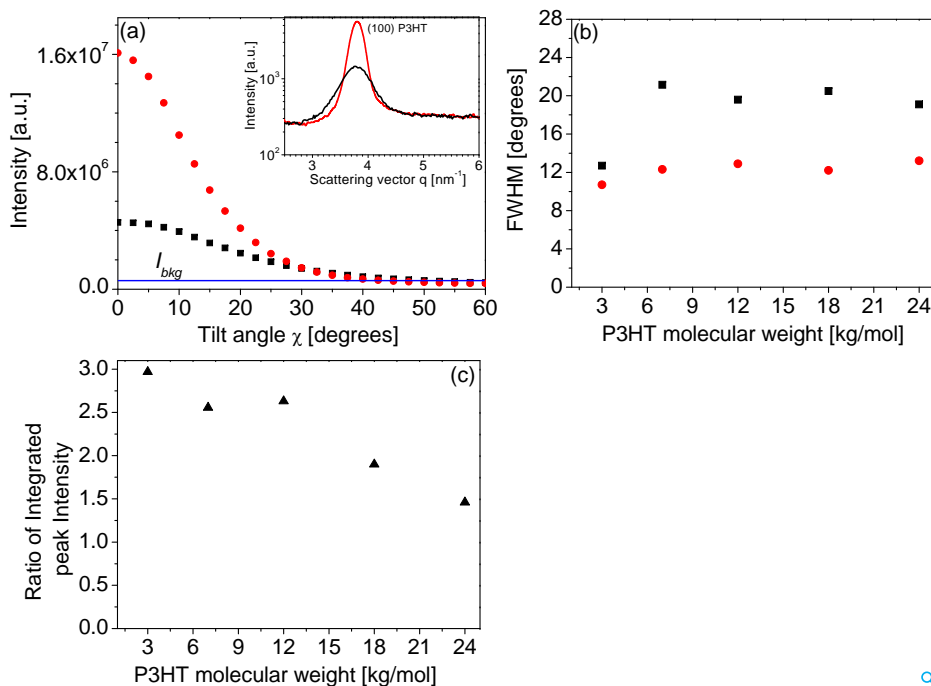
Figure 4.7: (a) Intensity vs. χ for the (100) reflection of P3HT 12 in as-cast (square) and melt-crystallized (circle) films. The inset shows the θ-2θ scan from the same films in the range of the (100) reflection using the point focus geometry. (b) FWHM of the orientation distribution of the crystalline part of the P3HT films as determined from measurements as shown in (a). (c) Relative increase in crystallinity as obtained from the ratio of the integrated intensity I_{int} of melt-crystallized and as-cast samples

Texture measurements were made at a fixed angle of incidence, corresponding to the (100) reflection of P3HT as obtained from θ-2θ scan, while the polar angle χ, was varied from 0° to 60°. For each χ, the azimuthal angle ϕ was scanned over 360°. The analysis of the texture measurement is described in the section 3.3.4. Exemplary intensity data I(χ) (as calculated using equation (3.2)) as a function of the polar angle χ, obtained for the as-cast and melt-crystallized films of P3HT 12 sample is shown in Figure 4.7(a). The reduction in FWHM of the intensity curve for the melt-crystallized films in comparison to as-cast films demonstrates a narrower orientation distribution of the (100) lattice planes. Thus, both effects, an increase in intensity as well as a narrowing of the orientation distribution were observed. Figure 4.7(b) shows the FWHM values as obtained from the I(χ) curves (after background correction) for all the samples. The integrated intensity I_{int}, obtained after background correction, which is proportional to the crystallinity of the sample, was calculated for all films using equation (3.3). An increase in the integrated intensity I_{int} was observed for all MW samples after melt crystallization indicating an increased crystalline order. Since the outer film shape and thickness of different P3HT samples varied to a certain degree, I_{int} can only be compared for a given sample before and after thermal treatment. The increase, measured by the ratio (Figure 4.7(c)), was highest for the lowest molecular weight sample.

4.2.3 Atomic force microscopy
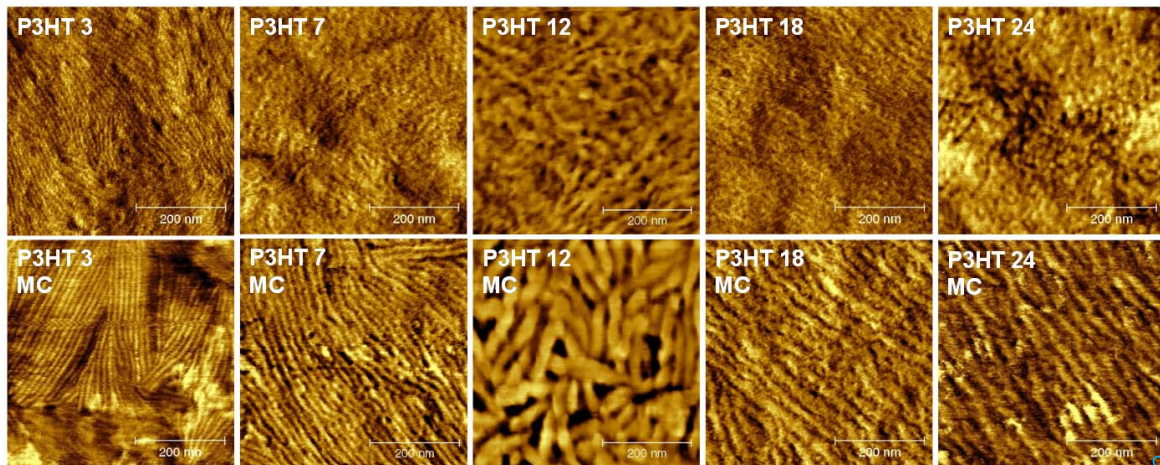
Figure 4.8:   AFM phase images of spin-cast (top) and melt-crystallized (MC) (bottom) films of different molecular weight P3HT's. The scan area for each sample is 500 nm x 500 nm. The scale bar in each image is 200 nm

Having addressed the issues of orientation and crystallinity by scattering techniques, the semi-crystalline morphology of P3HT films was characterized using AFM. AFM phase images of as-cast and melt-crystallized films of the different P3HT samples are shown in Figure 4.8. The phase signal mainly reflects the difference in the mechanical

properties of the crystalline and amorphous parts of the samples with the higher values of the phase corresponding to the stiffer, crystalline parts [148]. For the thin films and the given orientation distribution it is assumed that the structure observed at the surface of melt-crystallized films is characteristic for the entire film.

For the case of as-cast films, no well-defined structures were observed except for the lowest MW P3HT sample (P3HT 3). Kline et al. also reported clearly resolved lamellar crystals for as-cast low MW films and isotropic nodule-like structure for high MW P3HT films [37]. Obviously the structure obtained after spin coating corresponds to a trapped non-equilibrium structure, as crystallization is suppressed due to the low molecular mobility in a temperature range close to the glass transition temperature [83]. It is likely that the crystals for the as-cast samples are located close to the substrate and are therefore not visible by AFM. On the other hand, well defined lamellar structures were observed for all samples after melt crystallization. As shown from the scattering experiments (Figure 4.5(a)), the P3HT crystals adopt an edge-on orientation with the a-axis perpendicular to the substrate. Thus, the lamellar structures visible in the phase images correspond to the b-c plane of the P3HT crystallites. The AFM images also allow comparing the average periodicity (so called long period) of these lamellar structures for different molecular weights. The long period defines the average periodicity (repeating distance) of the layers of lamellar crystals in a stacked assembly. Visual inspection of the images of melt-crystallized samples suggests that the long period first increases with increasing molecular weight up to the P3HT 12 sample, but then decreases again for higher molecular weight samples. Previous studies have shown that low molecular weight P3HT forms extended chain crystals [73,80,162], while chain folding sets in for higher molecular weights [163] which explains why the long period levels off or even slightly decreases for higher molecular weight.
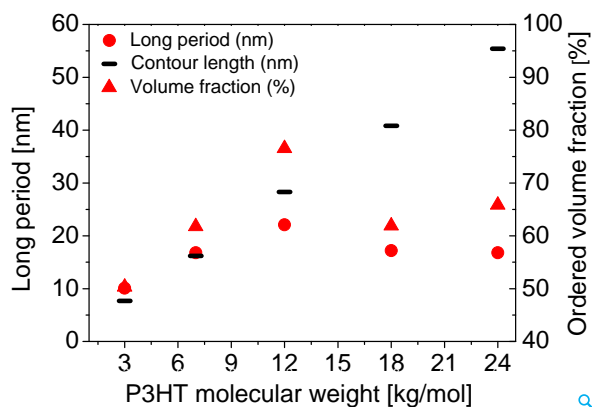
Figure 4.9: Left axis: Long period (circles) as measured by small angle x-ray scattering (SAXS) in bulk samples and calculated contour lengths (black bars) vs. molecular weight. Right axis: Volume fraction (triangle) of more ordered P3HT domains in melt-crystallized films evaluated by fitting ellipsometric data [157]

For a quantitative determination of the long period, small angle x-ray scattering (SAXS) experiments on bulk samples prepared with a similar thermal history were

performed [157]. The results are shown in Figure 4.9, the calculated contour lengths of the chains (number of repeating units times half of the unit cell parameter c) is given for comparison. The results confirm the AFM observation, namely an increase of the long period with increasing molecular weights up to P3HT 12. For further higher molecular weights the long period levels off or slightly decreases again. The comparison between the long period and the contour length indicates that chain folding sets in for molecular weights higher than that of P3HT 12 sample.

4.3 Charge transport properties

A typical j-V characteristic curve for the as-cast and melt-crystallized films for P3HT 12 is shown as a representative in Figure 4.10(a). The hole mobilities were evaluated by fitting measured IV characteristics obtained for the different molecular weight P3HT thin films using the Murgatroyd SCLC formula (equation (2.37)).

The SCLC hole mobilities μ_h for P3HTs of different molecular weight as determined in as-cast and melt-crystallized films are shown Figure 4.10(b)). The mobility in both as-cast and melt-crystalized films followed the same trend with the MW: an initially strong increase of the SCLC-mobility up to a maximum for the P3HT 12 sample followed by a decrease at higher MWs. Upon melt crystallization a strong increase of the mobility of up to one order of magnitude was found, which was especially pronounced for the higher molecular weight samples. The observed trend was reproduced across different samples and for varying film thicknesses. The maximum SCLC charge carrier
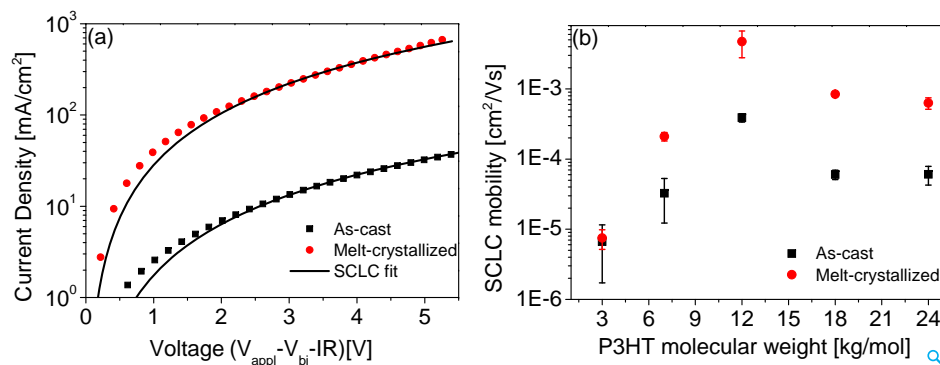

Figure 4.10: (a) The j-V characteristic of P3HT 12 sample in as-cast (square) and melt-crystallized (circle) devices measured at room temperature in diode configuration. The solid lines represent the SCLC fit with field dependent mobility. The j-V characteristics were corrected for the built-in voltage (V_{bi}) and the voltage drop (IR) over the contacts. (b) SCLC charge carrier mobility of holes in as-cast (square) and melt-crystallized (circle) P3HT films of different molecular weights. The mobility values were determined by fitting the J-V characteristics according to equation 4.2. [136] Each data point represents the average of 3-4 sets of devices produced for varying film thicknesses in the range of 250 nm - 350 nm

mobility was found for the intermediate MW P3HT sample (P3HT 12) for both, as-cast ($\mu_h = 3.9 \times 10^{-4}$ cm^2/(V·s)) and melt-crystallized ($\mu_h = 4.7 \times 10^{-4}$ cm^2/(V·s)) films.

Table 4.2: Material properties of highly regioregular P3HT samples of different molecular weight are summarized. Thin films were heated to 10°C above the respective melting temperature in order to ensure complete melting of the polymer. After the melting the thin film samples were slowly cooled down in a controlled manner (5 K/min), in order to allow the formation of large crystallites upon recrystallization

P3HT		P3HT 3	P3HT 7	P3HT 12	P3HT 18	P3HT 24
SCLC Mobility	AC	6.6×10^{-6}	3.2×10^{-5}	3.9×10^{-4}	6×10^{-5}	6.1×10^{-5}
[cm^2/(V·s)]	MC	7.5×10^{-6}	2.1×10^{-4}	4.7×10^{-3}	8.4×10^{-4}	6.3×10^{-4}
Crystal size along	AC	19.8	10.9	9.8	9.2	8.8
<100> axis (nm)	MC	22.0	20.4	21.1	19.5	19.3
Relative crystallinity of MC w.r.t AC		2.92	2.47	2.55	1.84	1.5
Long Period$_{SAXS}$ (nm)		10	16	22	17	17

The field activation factor ξ (equation (2.37)) was negative and lies between (-3x10^{-4} to -1x10^{-4}) (m/V)$^{1/2}$. The negative mobility dependence on the electric field has been explained earlier by the high spatial disorder in P3HT within the framework of the Gaussian disorder models [137].

4.4 Correlating structural order and charge transport properties

Different trends of the charge carrier mobility measured in diode configuration with respect to the MW are reported in literature. Goh et al. reported that SCLC mobility increases monotonically with MW in the range of (3 to 31) kg/mol [164]. On the other hand, Ballantyne et al. and Müller et al. showed that ToF (time of flight) mobility decreases with increasing molecular weight in the ranges of (13 to 121) kg/mol and (60 to 344) kg/mol, respectively [165, 166]. In contrast to these monotonic behaviors, it is here observed that the mobility in diode configuration does increase first to a maximum, followed by a decrease for increasing MWs. In fact, this non-monotonous trend of charge carrier mobility has been reported before in OFET configuration, where the authors interpreted the decrease (saturation) in the charge carrier mobility for high molecular weights with the degradation of morphology [167].

Based on our structural investigations as well as taking into account the existing literature [73, 162, 168], a schematic of the macromolecular structure of different molecular weight P3HTs is drawn in Figure 4.11 for visualization. Table 4.2 summarizes the findings quantitatively. The scheme depicts the increase in the crystallite size along the (100) direction and a narrower orientation distribution of the (100) lattice planes for the melt-crystallized films as obtained from the θ-2θ and texture measurements. Although one would expect that this orientation of the P3HT crystals is unfavorable for vertical charge transport along the a-axis, enhanced charge carrier mobilities along the vertical direction are observed for the melt-crystallized films. Nevertheless, the in-
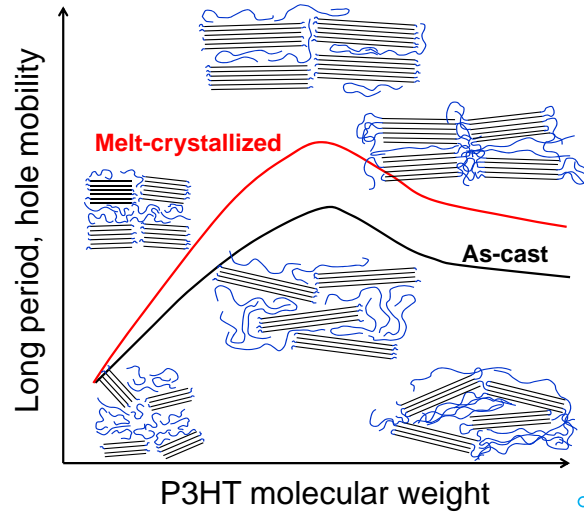
Figure 4.11: Schematic of the morphology and corresponding properties of semi-crystalline P3HT films (as-cast and melt-crystallized) versus the molecular weight. The schematic depicts an increased crystalline order and a narrowing of crystallite orientation in melt-crystallized films as compared to as-cast films. The schematic also exhibits the unique correlation between the long period and the hole mobility which increases with molecular weight, reaches a maximum for an intermediate molecular weight and then decreases slightly for the highest molecular weight samples. This trend is similar for both as-cast and melt-crystallized films

crease in crystalline order for melt-crystallized films corresponds well with the increase of the overall charge carrier mobility for melt-crystallized films [152].

However, the relationship between the crystallinity and the hole mobility does not seem to hold strictly over the full range of molecular weights. The lowest molecular weight sample (P3HT 3) exhibited no significant change in the charge carrier mobility after melt crystallization, despite the largest relative increase in crystallinity. However, the absorbance spectra of films based on this P3HT 3 sample showed the broadest absorption band - corresponding to large variations in the electronic bandgap. These, in turn, lead to a strongly disturbed charge transport, as the low bandgap energy or ordered regions do not extend vertically throughout the whole film. In order to form a percolating path, the charge carriers have to pass through the large bandgap energy or amorphous regions [160], which are interconnecting the crystallites. Hence the amorphous regions between the crystallites constitute significant barriers for efficient charge transport for the smallest molecular weight P3HT sample.

The schematic also depicts the observed correlation between the long period and the hole mobility. The increase in the long period for low and intermediate MW P3HT correlates well with the increase in mobility. The charge carrier mobility for high MW P3HT is then again limited by the amorphous regions, as their volume fraction increases as compared to the intermediate MW sample by chain folding [168]. This hypothesis is further supported by the volume fraction of the ordered P3HT domains as determined by spectroscopic ellipsometry on P3HT films (Figure 4.9) [157]. Previously, the role of grain boundaries has been explicitly emphasized as the limiting factor for

the charge transport through semi-crystalline P3HT [153,169]. In good agreement with these reports, here again, the amorphous regions around crystallites possibly limit the transport properties and could explain the gradual reduction of the mobility with the long period for high MWs. Furthermore, the results indicate that increase in crystalline order and variation in energy levels between crystalline and amorphous parts of the sample play a dominant role in determining the overall charge transport. Due to the similar trend of charge mobility in as-cast and melt-crystallized devices with MW (Figure 4.9), it is believed that the long period in as-cast films follows the same trend as observed for the melt-crystallized films.

4.5   Summary

Melt crystallization of semi-crystalline highly regioregular P3HT films resulted in a substantial increase in crystalline order and narrowing of crystallite orientation, as compared to as-cast films, as observed from the scattering analysis (combination of θ-2θ and texture measurements). In conjunction with an increased crystalline order, we observed a considerable increase by up to an order of magnitude in the hole mobility, as determined in SCLC devices. Even though a hindrance due to the insulating alkyl side chains could be expected for the observed a-axis orientation within the thin films, the enhanced crystalline order was generally found to be beneficial for the charge transport. Interestingly the lowest molecular weight sample did not yield improved charge carrier mobility upon melt crystallization. This deviation from the trend could be understood by investigation of the optical properties of the P3HT 3 sample. Interestingly, the charge transport in both, as-cast and melt-crystallized, films exhibited the same trend with molecular weight. At first the charge carrier mobilities increased with the molecular weight, reaching a maximum for an intermediate molecular weight (P3HT 12), which was followed by a decrease for the higher molecular weight samples. This behavior of the mobility is - on a logarithmic scale - in excellent agreement with the experimentally determined long period of the crystallites in bulk and the volume fraction of highly ordered P3HT within thin film samples. We conclude from the experimental data, that for high molecular weights, effects of chain folding and the concomitant increase of the amorphous volume fraction of P3HT limit the charge transport [163]. In summary, we were able to demonstrate that a higher crystalline order in melt-crystallized films as compared to as-cast films results in improved charge carrier mobilities. Thus, structural investigations are of utmost importance to understand the electronic properties of semi-conducting materials. The significance of this study lies in the fact that it provides an insight to the positive effects of higher crystalline order on the charge transport properties and an input to incorporate the P3HT 12 as the donor block in the fully conjugated block copolymer.

Having investigated the microstructure of the donor material, we further require a suitable electron conducting material for incorporation in the fully conjugated donor acceptor block copolymer. For this we investigated the structural and transport behavior of the electron conducting materials consisting of perylenes which forms the core of the next chapter.

Chapter 5

Investigation of microstructural order and phase behavior in perylenes

Perylene bisimide (PBI) derivatives have emerged as an important class of n-type semi-conductors in the field of opto-electronics due to their relatively high electron affinity, strong visible light absorption along with good photochemical and thermal stability. They have found applications in xerographic devices [170], organic field effect transistors (OFETS's) [104,171] and organic photovoltaics (OPV's) [110,172]. Previous studies on perylene derivatives have shown that substituents attached to the aromatic core can alter not only the solubility, but also the opto-electronic properties [173]. Various crystalline and liquid-crystalline phases of different symmetries have been observed in low molecular weight PBI's depending upon the architecture, nature and length of the substituents [95,97,100,174,175]. Thus, substituents are a powerful tool to tune the self assembling and electronic properties of PBI's. In organic molecules/semiconductors, the charge carrier mobility is not an intrinsic property, albeit, it depends strongly on the molecular packing [176]. While on a microscopic scale, local order determines the hopping process of charges between the molecules, defects like grain boundaries can pin charges on a macroscopic scale. Therefore, liquid-crystalline materials offer the possibility to circumvent this problem by combining high local order with self healing of structural defects and grain boundaries [94].

Few important questions that still need to be addressed are: How is the phase behavior (3D crystalline or 2D liquid-crystalline) and molecular order affected by tuning the substituents/polymerization? What is the effect of crystallinity and crystallite orientation in thin films and its importance with respect to charge transport? Is there any direct one-to-one correspondence of the variation in structural order and phase behavior with the transport properties? Keeping these questions in mind this study presents investigations on the structure-property relationship of a series of unsymmetrical N-substituted PBI compounds with linear side chains at one imide N-atom position and a swallow tail substituent at the other imide position along with a polymer containing PBI moieties as pendant groups using DSC, optical microscopy, x-ray scattering and SCLC. The nature of the substituents in the small molecule compounds was systematically varied from hydrophobic alkyl groups to hydrophilic oligoethylene-glycol (OEG)
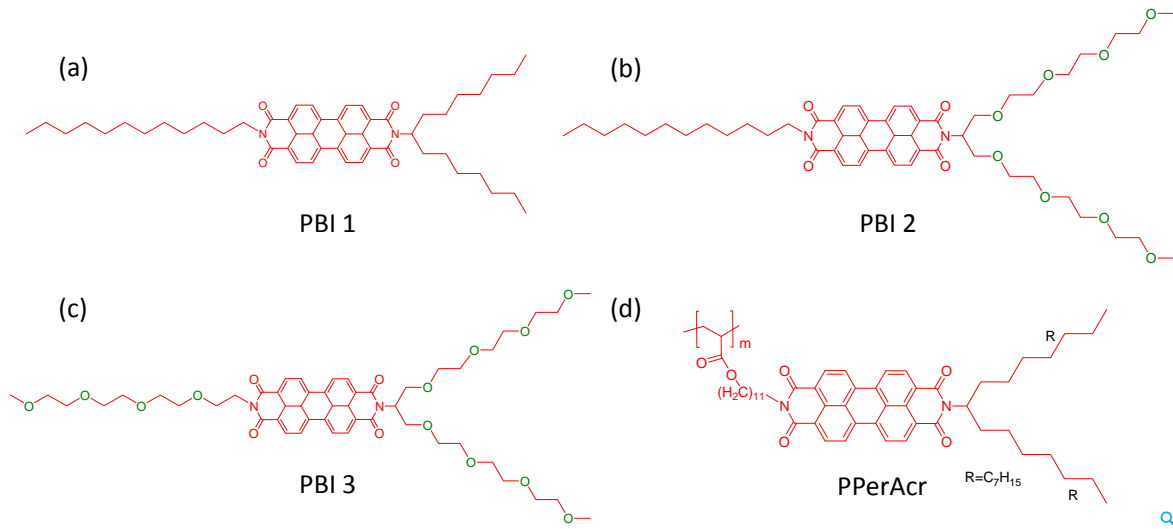
Figure 5.1: Chemical structures of the investigated materials: (a) alkyl substituted low molecoular weight PBI 1; (b) OEG substituted (at swallow tail position) low molecular weight PBI 2; (c) OEG substituted (at both swallow tail and linear position) low molecular weight PBI 3; and (d) side-chain polymer PPerAcr with polyacrylate backbone

groups. The study revealed that while, alkyl substituted PBI exhibited a crystalline 3D ordered phase; the OEG substituted PBI's and the side chain polymer exhibited a liquid-crystalline phase at room temperature. While, the molecular order was largely suppressed in pristine (as spun/blade coated) films, thermal annealing resulted in an enhanced crystalline order with a dominant edge-on orientation of PBI molecules with respect to the substrate. The increased crystalline order and packing correlates well with the enhanced charge carrier mobilities as measured by SCLC for all the thermally treated films from samples exhibiting liquid-crystalline phases. However, for the alkyl substituted PBI (exhibiting 3D crystalline phase) the charge carrier mobility was found to be reduced by an order of magnitude upon thermal treatment.[1]

5.1 Materials and sample preparation

5.1.1 Materials

The chemical structures of the investigated samples are shown in Figure 5.1. The low molecular weight perylene bisimide (PBI 1) was asymmetrically substituted with a branched (C15) alkyl swallow tail at one of the imide position and a linear C12 alkyl group at the other imide position and has a molecular weight of M = 769 g/mol. While PBI 2 had OEG substitution at the swallow tail carbon position, PBI 3 had OEG substitution at both the imide position. The molecular weight of PBI 2 and PBI 3 are 925 g/mol and 947 g/mol respectively. The side-chain polymer poly(perylene bisimide-acrylate) (PPerAcr) (Figure 5.1(d)) has a molecular weight of M_n= 23 kg/mol (GPC

---

[1]The results of this work were published in following reference [40, 177]

in THF, polystyrene standard) and a polydispersity of PDI = 1.71. The monomer of PPerAcr has a molecular weight of $M_o = 825$ g/mol. The complete synthesis details of all the perylene samples are described elsewhere [174, 178].[2]

5.1.2 X-ray scattering on bulk samples

X-ray scattering experiments on different perylene samples at the intermediate and wide angles were performed in transmission geometry with a laboratory rotating anode setup. The wavelength used was Cu-k_α radiation ($\lambda = 0.154$ nm). Aluminum disks with a central hole of 0.8 mm diameter were used as sample holders. Measurements were taken on two sample stages (SS2 and SS3 c.f. Figure 3.4). The samples were mounted on a Linkam hotstage for temperature control. Heat conducting paste was used to ensure good thermal contact. Scattering patterns were recorded during a stepwise cooling run (cooling rate 10 K/min) after heating the samples to molten state in vacuum. Liquid nitrogen was used for controlled cooling. The exposure time for each measurement was 600 s. The scattering patterns were corrected by subtracting the empty cell measurements. Silver behnate was used for calibration. For orienting the sample in presence of magnetic field, the setup as described in section 3.3.2 was used. Scattering patterns from oriented samples were recorded at room temperature.

5.1.3 Thin films for structural characterization

Thin films of low molecular weight PBI compounds (PBI 1, 2, and 3) for structural investigations were blade coated from chloroform solution on commercial glass substrates with a thin layer of PEDOT:PSS to resemble the actual SCLC device architecture. The glass substrates were cleaned in an ultrasonic bath using the following sequence: detergent, water, acetone and 2-propanol. The film thickness of 100 nm was measured using a profilometer. Due to the fast evaporation rate of this low boiling point solvent, the thin film morphology is a non-equilibrium (quenched/amorphous) state. To allow for better packing and orientation in semiconducting polymer films, commonly, thermal annealing is employed [13]. During this treatment, films are heated and annealed at an elevated temperature (usually above the glass transition temperature but below the melting temperature) resulting in crystallization either during the heating or the annealing process due to an increased molecular mobility [156]. Thin films of PBI 1, 2, and 3 were thermally annealed for 5 min at 5 °C below their respective melting temperature (Table 5.1) on a hotplate in an inert atmosphere of nitrogen and cooled at a rate of 3 K/min to room temperature. This thermal treatment was chosen for low molecular weight PBI's since the thin films de-wetted upon melting. For PPerAcr, thin films were spin coated (1000 rpm) from chloroform solution (concentration 10 mg/ml) on silicon substrates which were cleaned beforehand using sulfuric acid. The films were dried in vacuum at room temperature for several hours and were then heated above the

---

[2]Synthesis and device characterization for PBI 1, PBI 2, and PBI 3 was done by M. Muth (Univ. Bayreuth). XRD analysis of PBI 1 and PPerAcr (bulk samples only) was done by Peter Kohn (MLU Halle). SCLC properties of PPerAcr was investigated by C. R. Singh (TU Ilmenau)

melting point on a Linkam hotstage (in nitrogen atmosphere) and cooled at a rate of 10 K/min to room temperature. This thermal treatment is more defined as it removes any pre-history of crystallites during the thermal treatment. The film thickness as determined by reflectivity measurements was $\approx$ 70 nm.

5.1.4 Single carrier space charge limited devices

SCLC electron-only devices were fabricated using the following structure: glass/ITO/ PEDOT:PSS/active layer/Ca/Al. Commercial ITO coated glass substrates were clean ed using following sequence in an ultrasonic bath: detergent, water, acetone and 2-propanol. After ozone treatment of the substrates for 5 min, PEDOT:PSS was spin-coated on the ITO surface and dried at 130 °C for 30 min. All following steps were carried out under nitrogen atmosphere. After cooling the substrate, the active layer (for PBI 1, PBI 2, and PBI 3) was blade coated from chloroform solutions with a film thickness of $\approx$ 300 nm. The substrates were then placed in a thermal evaporation chamber to evaporate the top electrodes (Ca/Al) under high vacuum ($1\mathrm{x}10^{-6}$ mbar) through a shadow mask (active area 4 mm^2). The current-voltage characteristics of the devices were measured using a Keithley 2420 digital unit at 25 °C. Same thermal treatment was applied to the devices as used for structural investigations.

5.2 Structural characterization

5.2.1 Differential scanning calorimetry

The results of the DSC measurements for PBI 1, PBI 2, PBI 3, and PPerAcr are shown in Figure 5.2. All the materials exhibited a single reversible phase transition with largely different values for ΔH. While PBI 1 showed a melting enthalpy (ΔH) of 20.0 kJ/mol , the melting enthalpy for PPerAcr was approximately 5.5 kJ/mol (Table 5.1). PBI 2 and PBI 3 exhibited melting enthalpy values of 12.1 kJ/mol and 17.2 kJ/ mol respectively. As the mass fraction of the aromatic core plus side chains and spacer in the polymer (PPerAcr) is $\approx$ 91%, the trivial effect of a reduction of the fraction of structure forming material in PPerAcr cannot account for the large difference in the values of ΔH. For several low molecular weight PBIs with different aliphatic substituents the ΔH values for a transition from a liquid-crystalline phase to the isotropic state were reported to be of the order of 10 kJ/mol, while for a transition from crystalline to isotropic melt considerably larger enthalpy values are common [95, 97, 174]. The DSC results therefore suggest that while the low molecular weight compound PBI 1 forms a crystalline phase, the structure in the polymeric PPerAcr and OEG substituted PBI 2 and PBI 3 is liquid-crystalline. As will be shown, the results of all other experiments were consistent with that assumption.
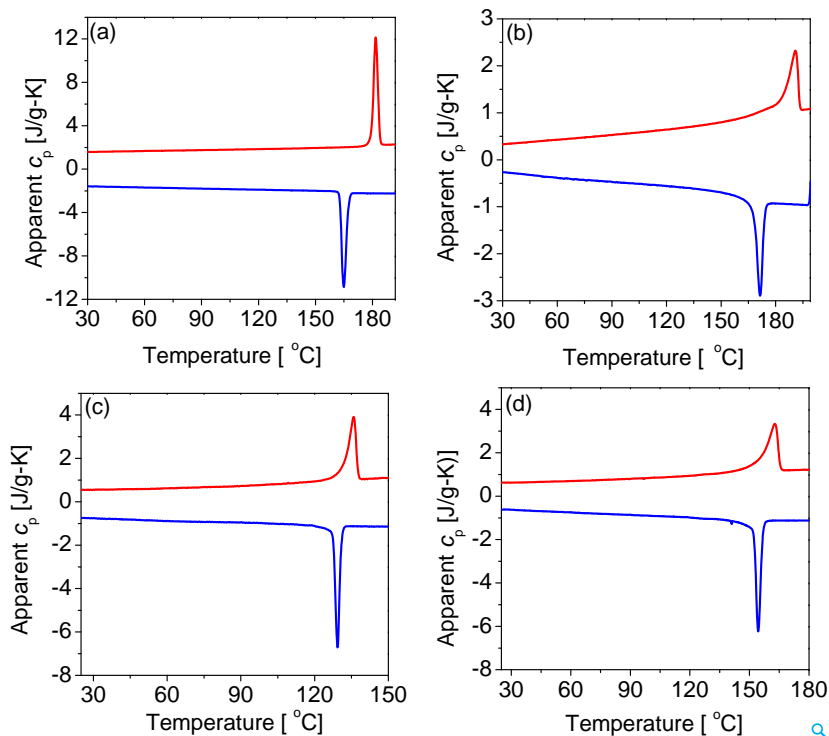
Figure 5.2: Differential scanning calorimetry thermogramms of (a) PBI 1, (b) PPerAcr, (c) PBI 2 and (d) PBI 3 with a heating (red) and cooling (blue) rate of 10 K/min

Table 5.1: Summary of the DSC results of the different PBI samples obtained for heating and cooling with 10 K/min. The enthalpies (kJ/mol) associated with the transitions are given in parenthesis

Sample	2nd heating cycle	1st cooling cycle
PBI 1	Cr 181.8 °C (20.4)$\to$ I	I 164.9 °C (18.9)$\to$ Cr
PBI 2	LC 136.4 °C (12.1)$\to$ I	I 129.5 °C (11.4)$\to$ LC
PBI 3	LC 164.8 °C (17.2)$\to$ I	I 154.8 °C (15.5)$\to$ LC
PPerAcr	LC 190.8 °C (5.5)$\to$ I	I 171.4 °C (6.14)$\to$ LC

5.2.2   Polarized optical microscopy

Polarized optical microscopy (POM) images of the perylene materials sandwiched between two glass slides (with crossed polarizers) are shown in Figure 5.3. All samples were heated above T_m for 5 min and then cooled with 10 K/min below the phase transition temperature, where birefringed textures were observed. The low molecular weight PBI 1 in Figure 5.3(a) formed large spherulites with a size of a several hundred micrometers. Spherulites often form in crystalline compounds and were previously also observed for discotic systems [174, 179, 180]. The texture of the polymeric PPerAcr (cf. Figure 5.3(b)) and OEG substituted PBI's (PBI 2 and PBI 3) (Figure 5.3(c,d)) is typical for a liquid-crystalline structure [174]. Further, in contrast to PBI 1, the textures
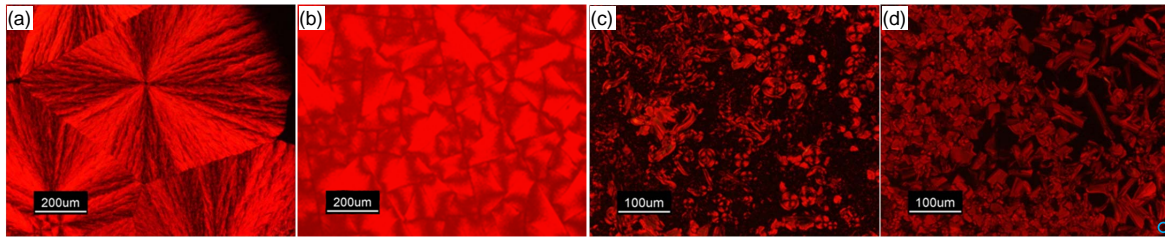
Figure 5.3: Polarized light optical microscopy: Crystalline phase of (a) PBI 1 at 172 °C; and liquid-crystalline phase of (b) PPerAcr at room temperature (c) PBI 2 at 130 °C and (d) PBI 3 at 155 °C. The birefringed textures obtained for PBI 2 and PBI 3 are highly shearable and re-orient after application of a small mechanical force. However no shearing was possible for the crystalline PBI 1. The scale bars in (a) and (b) are 200 μm while for (c) and (d) are 100 μm

of PBI 2 and PBI 3 are highly shearable at the given temperatures indicating that PBI 2 and PBI 3 indeed form liquid-crystalline phase. Details about the crystalline (PBI 1) and liquid-crystalline mesophases (PPerAcr, PBI 2 and PBI 3) were investigated using x-ray scattering.

5.2.3 X-ray diffraction: Microstructure in bulk samples

To investigate the structure of the different perylene samples on a microscopic scale, temperature dependent x-ray scattering experiments were performed.

We start with the analysis of PBI 1 and PPerAcr. In accordance with DSC results, temperature dependent x-ray scattering patterns for PBI 1 and PPerAcr exhibited a single phase transition from the melt to an ordered state at room temperature [40]. While, for a detailed study the reader is directed to the following reference [40], the main results of the analysis are presented.

The analysis of the side chain polymer PPerAcr is presented first. The x-ray scattering patterns obtained at room temperature for the intermediate and wide angle scattering vectors are shown in Figure 5.4(a) and (b). The WAXS pattern of PPerAcr (Figure 5.4(b)) showed no Bragg reflections in the range q ≈ (7 to 15) nm^{-1}. The absence of higher order (*hk0*) reflections in this range is in line with the assumption of a liquid-crystalline structure, as a strong reduction of the intensity of the reflections at higher q, caused by lateral fluctuations of the stacked molecules, would be expected in this case. The broad halo at around q ≈ (10 to 17) nm^{-1} is usually assigned to the scattering from the liquid alkyl side chains [91, 181]. The broad peak at q = 18.23 nm^{-1} reflects the π-stacking. The small value of the correlation length of $l_{corr} = 2\pi/\Delta q$ ≈ 4.5 nm as determined from the peak width is an indication for liquid like packing of the molecules within the stacks [91]. No reflection was found at q-values larger than q = 18.23 nm^{-1}; i.e. no (*hkl*) reflections with *h* or *k* and additionally *l* non-zero were observed, consistent with a liquid-crystalline structure without 3D crystalline packing. Extracting the lattice parameters for the two-dimensional lattice of the stacks from the positions of the (*hk0*) Bragg reflections alone is only correct, if the stacking direction of the cores is perpendicular to the plane of the 2D lattice. This could be demonstrated
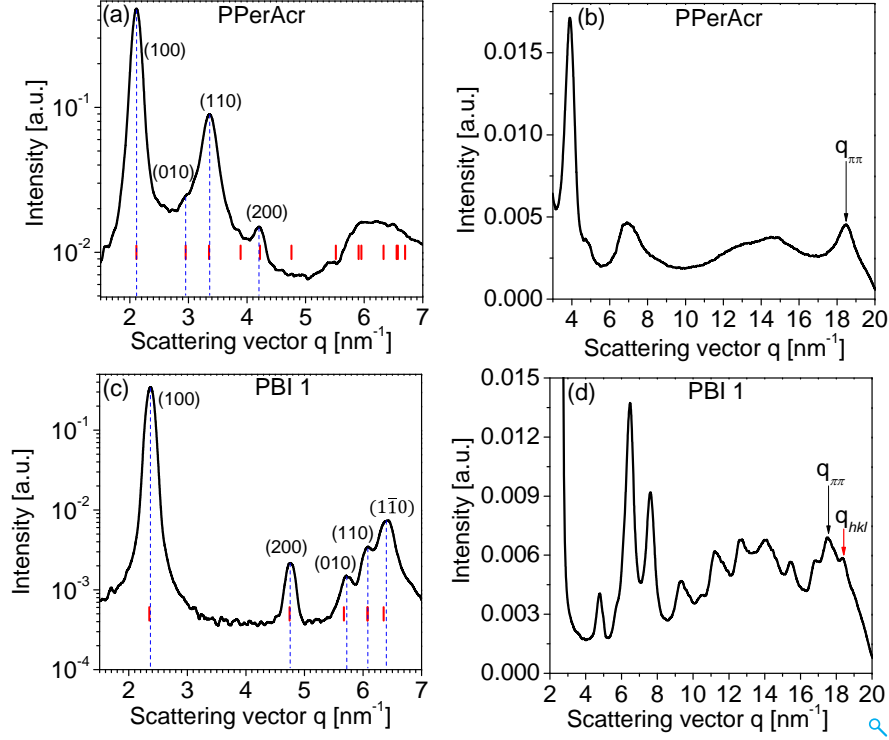
Figure 5.4: Bulk x-ray scattering patterns at T = 20 °C in the (a), (c) intermediate-angle range and (b), (d) wide-angle range for PPerAcr and PBI 1. The blue dashed lines correspond to experimentally determined positions of Bragg reflections, while the red bars indicate the positions expected for the suggested oblique lattice. The position of the reflection associated with the π-stacking is indicated by the arrow. While the scattering pattern of PPerAcr (b) shows no reflection corresponding to the mixed indices i.e. q_{hkl}, the scattering pattern of PBI 1(d) exhibits such a reflection(indicated with red arrow) indicating a 3-D crystalline ordering

by scattering patterns from oriented samples. The 2D scattering pattern at room temperature revealed intensity maximum along the equatorial and meridional positions respectively [40]. The reflection corresponding to the π-stacking showed equatorial intensity maxima demonstrating a preferred orientation of the π-stacking direction perpendicular to the magnetic field. The (hk0) reflections showed meridional intensity maxima. Such a pattern is expected if the π-stacking direction is aligned perpendicular to the magnetic field but free to rotate in the corresponding plane [143]. For PPerAcr the observed reflections (Figure 5.4(a)) can be described by a two-dimensional oblique lattice with lattice constants a = 3.01 nm, b = 2.15 nm, and γ = 81°. For the π-π stacking distance c $\approx$ 0.345 nm was deduced from the peak at q = 18.23 nm^{-1} in Figure 5.4(b). Based on these lattice parameters, only a unit cell containing two monomers gives a reasonable density $\rho \approx$ 1.26 g/cm^3; where

$$\rho = n \cdot \frac{M_{monomer}}{v \cdot N_A} \tag{5.1}$$

($M_{monomer}$ is the molar mass, v is the volume of the unit cell, n is the number of molecules and N_A is the Avogadro number). The structure of the unit cell which

is suggested based on these considerations is schematically depicted in Figure 5.5(a). While the (010) reflection (the weak shoulder at q $\approx$ 3 nm^{-1}) was nearly absent, the (110) reflection was clearly visible, indicating that a unit cell containing two molecules in b-direction was appropriate, caused e.g. by a slight displacement of every second core along the a-direction.
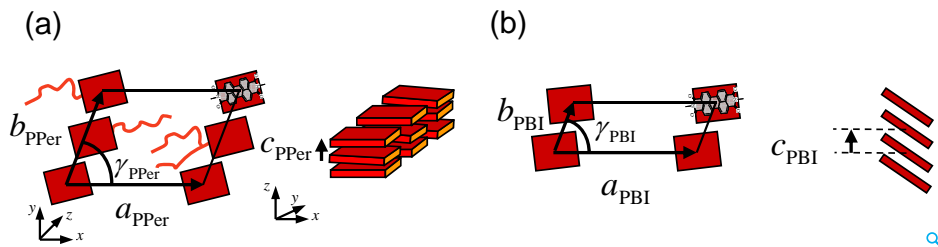

Figure 5.5: Illustration of the suggested monoclinic unit cell and columnar stacking for (a) PPerAcr and (b) PBI 1

The respective scattering pattern of PBI 1 at T = 20 °C at intermediate and wide angle scattering vector is shown in Figure 5.4(c) and (d). In contrast to the polymeric PPerAcr, the large number of reflections visible in the range q $\approx$ (7 to 15) nm^{-1} is consistent with a well-ordered crystalline structure with only small fluctuations of the molecules around their lattice positions. The peak observed at q = 17.56 nm^{-1} was assigned to the packing of the PBI molecules within the stacks, i.e. a (001) reflection. A further peak was observed at q = 18.41nm^{-1} (indicated by a red arrow in Figure 5.4(d)). Such reflections are indicative for a 3D lattice as they correspond to mixed (hkl) reflections with h and/or k and additionally l nonzero. They generally occur in crystalline or in plastic phases [91, 92, 96]. PBI 1 was also cooled from the isotropic melt state in the magnetic field. Unlike PPerAcr, the 2D scattering pattern showed no azimuthal anglular dependence on intensity [40]. This is in line with the observed spherulitic crystallization (Figure 5.3 (a)) as spherulites are overall isotropic objects unaffected by external fields [143]. The detailed analysis of the exact crystal symmetry was difficult de to the isotropic crystal orientation.

Independent of the exact unit cell symmetry, the fact that q$_{(200)}$ $\approx$ 2q$_{(100)}$ (Figure 5.4(c)), with no reflection visible in between, clearly indicated a lamellar structure as also observed for the PPerAcr. The larger lattice parameter in c-direction of d$_{\pi-\pi}$ $\approx$ 0.36 nm for the crystalline PBI 1 could indicate a tilt of the flat PBI core with respect to the (a/b) plane. The results of this qualitative analysis are schematically depicted in Figure 5.5(b). For further analysis a monoclinic unit cell with lattice parameters a = 2.68 nm, b = 1.11 nm, γ = 81° and c = 0.36 nm was chosen. All the reflections in Figure 5.4(c) could be indexed consistently with this choice of a unit cell. The resulting crystallographic density was calculated to be ρ $\approx$ 1.21 g/cm^3 (equation (5.1)) with one monomer per unit cell.

Figure 5.6 shows the complete temperature dependent scattering patterns during a stepwise cooling, from the melt state, of PBI 2 and PBI 3 in the intermediate scattering vectors range. In accordance with the DSC results, at temperatures below 130 °C, both
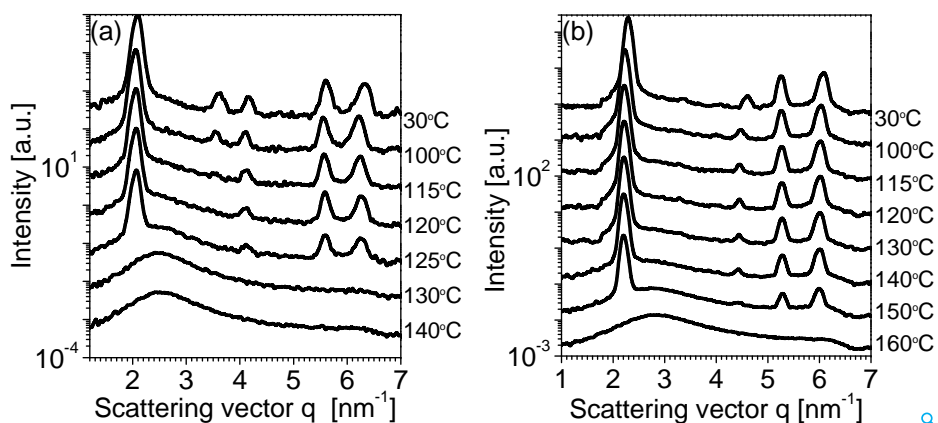
Figure 5.6: Temperature dependent XRD data as measured during cooling from the isotropic melt (a) PBI 2 and (b) PBI 3

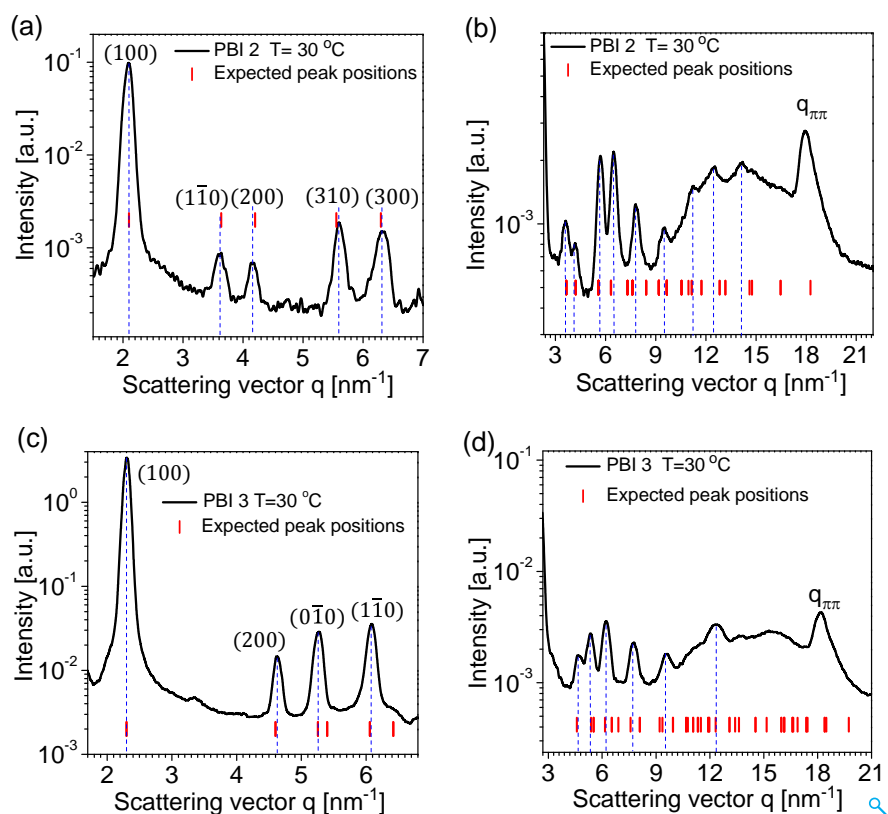**Figure 5.7:** Bulk x-ray scattering measurements for PBI 2 at T = 30 °C at (a) intermediate and (b) wide angle range; the observed Bragg reflections in (a) can be indexed by assuming a hexagonal lattice; red bars denote the expected peak positions for a hexagonal unit cell with lattice parameters a = b = 3.47 nm, c = 0.350 nm and $\gamma = 60°$. Bulk x-ray scattering measurements for PBI 3 at T = 30 °C in intermediate (c) and wide-angle range (d); the observed Bragg reflections in (c) can be indexed by assuming a monoclinic unit cell; red bars denote the expected peak positions for the unit cell with lattice parameters a = 2.76 nm; b = 1.2 nm, c = 0.346 nm and $\gamma = 81.5°$

samples were in an ordered state as indicated by the appearance of Bragg reflections. No additional phase transitions were observed during further cooling. The scattering patterns at intermediate and large scattering vectors of PBI 2 and PBI 3 recorded at T = 30 °C are shown in Figure 5.7(a and b) and Figure 5.7(c and d) respectively. The peak around q = 17.95 nm^{-1} reflects the π-π stacking. As expected for a liquid-crystalline phase additional reflections with larger q on the right hand side of the (001) are not observed. This is in line with the previous observations from optical microscopy that PBI 2 and PBI 3 are liquid-crystalline. In order to determine correct lattice parameters for the 2D lattice of the stacks from the positions of (*hk0*) reflections, scattering patterns were obtained from oriented PBI 2 and PBI 3 samples. Alignment of PBI 2 and PBI 3 was also achieved by slowly cooling the sample (10 K/min) from the isotropic state in a magnetic field.
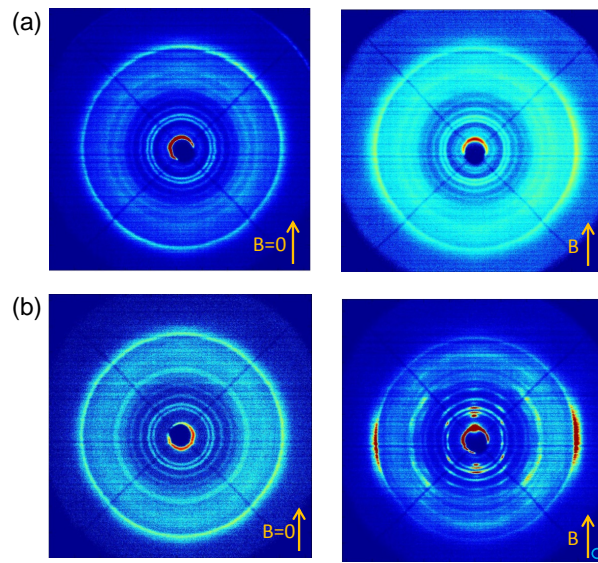

Figure 5.8: 2D wide angle scattering pattern of samples cooled without magnetic field B (left) and in presence of the magnetic field (right) of (a) PBI 2 (b) PBI 3
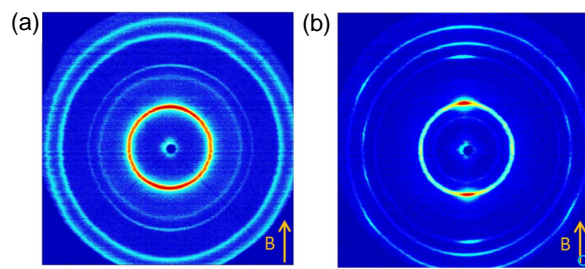

Figure 5.9: 2D intermediate angle scattering pattern of (a) PBI 2 and (b) PBI 3 samples cooled in presence of the magnetic field B

The 2D scattering pattern of PBI 2 measured at room temperature is shown in Figure 5.8(a) and Figure 5.9(a). The reflection corresponding to the π-π stacking direction

showed weak equatorial intensity maxima demonstrating a preferred orientation of the π-π stacking direction perpendicular to the magnetic field while the (*hk0*) reflections showed weak meridional intensity maxima. The azimuthal angular dependence of intensity of various reflections is shown in Figure 5.12(a). Based on these findings all reflections observed in Figure 5.7(a) and (b) can be indexed by a hexagonal unit cell with lattice constants a = b = 3.47 nm, c = 0.350 nm and γ= 60°. There is only a slight discrepancy between the observed and calculated positions of scattering peaks for the peaks at q = 12.5 nm^{-1} and q = 14.15 nm^{-1} which is difficult to analyze in depth with the given accuracy of the measurements. A reasonable density was obtained by assuming that the unit cell contains two molecules leading to a value of 0.84 g/cm^3 according to equation (5.1). An illustration of PBI columns forming a hexagonal packing is shown in Figure 5.10(a).

The scattering pattern of PBI 3 (Figure 5.7(c)) is similar to that of PBI 2. It can be described by assuming a lamello-columnar packing and an oblique unit cell with lattice parameters a = 2.76 nm, b = 1.2 nm and γ = 81.5° where γ is the angle between lattice vectors $\boldsymbol{a}$ and $\boldsymbol{b}$, schematically depicted in Figure 5.10(b). However, the unit cell assignment of PBI 3 was more complex as compared to the other perylene samples.
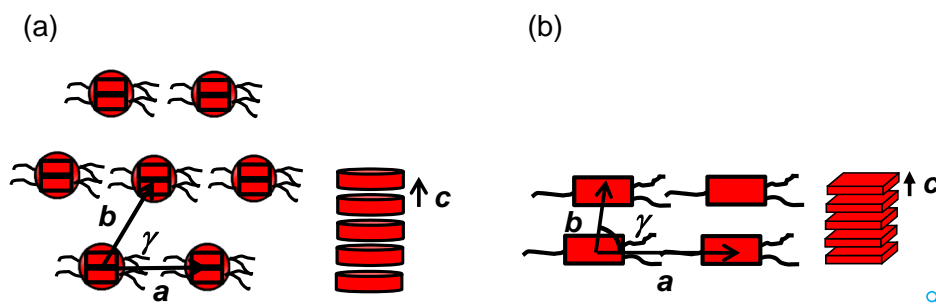

Figure 5.10: (a) Illustration of columnar hexagonal packing of stacks of PBI 2; and (b) monoclinic unit cell for PBI 3

The 2D scattering pattern, measured at room temperature, after cooling PBI 3 from the melt in presence of magnetic field is shown in Figure 5.8(b) and 5.9(b). The reflection corresponding to the π-π stacking direction here, again exhibited strong equatorial intensity maxima implying a preferred orientation of the stacks perpendicular to the magnetic field. Reflections corresponding to the (100) lattice planes exhibited intensity maximum along the meridian implying that reciprocal lattice vector $\boldsymbol{a}^*$ is oriented along the magnetic field direction. In addition, several reflections were observed at the non-equatorial- non-meridional positions. To completely understand this complex 2D scattering pattern, a more quantitative approach was employed:

A possible orientation of the monoclinic unit cell under the influence of the magnetic field $\boldsymbol{B}$, derived from the observation that $\boldsymbol{c}^*$ is perpendicular and $\boldsymbol{a}^*$ parallel to $\boldsymbol{B}$ is shown in Figure 5.11. The observed scattering pattern corresponds to a situation where the incoming beam is lying in the horizontal plane and an intensity distribution resulting from an average due to a rotation around the vertical axis. A coordinate
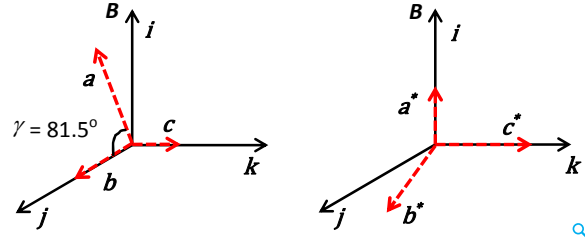
Figure 5.11: Direction of the magnetic field and lattice vectors in the reference coordinate system: (left) real space and (right) reciprocal space

system with unit vectors $\boldsymbol{i}$, $\boldsymbol{j}$, and $\boldsymbol{k}$ with $\boldsymbol{i}$ being parallel to $\boldsymbol{B}$ is used. This gives

$$\boldsymbol{a} = a \sin \gamma \ \boldsymbol{i} + a \cos \gamma \ \boldsymbol{j}; \ \boldsymbol{b} = b \ \boldsymbol{j}; \ \boldsymbol{c} = c \ \boldsymbol{k} \tag{5.2}$$

Correspondingly, a reciprocal scattering $\mathbf{q}_{hkl}$ vector is given by

$$\mathbf{q}_{hkl} = 2\pi \left[\left\{ \frac{h}{a \ \sin \gamma} - \frac{k \ \cos \gamma}{b \ \sin \gamma} \right\} \boldsymbol{i} + \frac{k}{b} \boldsymbol{j} + \frac{l}{c} \boldsymbol{k} \right] \tag{5.3}$$

where a, b, c correspond to the crystallographic lattice parameters. γ is the angle between the crystallographic axis $\boldsymbol{a}$ and $\boldsymbol{b}$. The interplanar spacing d_{hkl} can be calculated as

$$|\mathbf{q}_{hkl}| = \frac{2\pi}{d_{hkl}} = 2\pi \left[\frac{h^2}{a^2 \ \sin^2 \gamma} + \frac{k^2}{b^2 \ \sin^2 \gamma} - \frac{2hk \ \cos \gamma}{ab \ \sin^2 \gamma} + \frac{l^2}{c^2} \right]^{\frac{1}{2}} \tag{5.4}$$

The azimuthal angle of a reflection (hkl) measured from the vertical axis as observed in the 2D scattering pattern corresponds now to the angle between $\mathbf{q}_{hkl}$ and $\mathbf{q}_{100}$

$$\mathbf{q}_{hkl} \cdot \mathbf{q}_{100} = |\mathbf{q}_{hkl}| \, |\mathbf{q}_{100}| \cos \Delta \psi \tag{5.5}$$

In correspondence with equation (5.5), the $(0\bar{1}0)$ reflection appears at an angle of 80° from the meridian. With this unit cell we were able to assign indices to all observed reflections and to predict the azimuthal positions on the 2D scattering pattern. Table 5.2 summarizes the calculated and experimentally determined (c.f. Figure 5.12(b)) azimuthal positions of reflections in aligned PBI 3 sample. In addition there is a second population of crystals with the same structure but a different orientation distribution leading to an additional broader meridional maximum for the ($hk0$). This pattern corresponds to an orientation distribution similar as observed for PBI 2, characterized only by the condition that the columnar stacks are standing perpendicular to the magnetic field. The estimated crystallographic density based on the lattice parameters mentioned above gives a larger density of $\rho = 1.4$ g/cm^3 for 1 molecule per unit cell which is attributed to the combined effect of tighter packing and a larger oxygen content of the molecules.

The results of all the experiments on bulk samples consistently indicated the same main structural difference, though the detailed structure is different: while the low
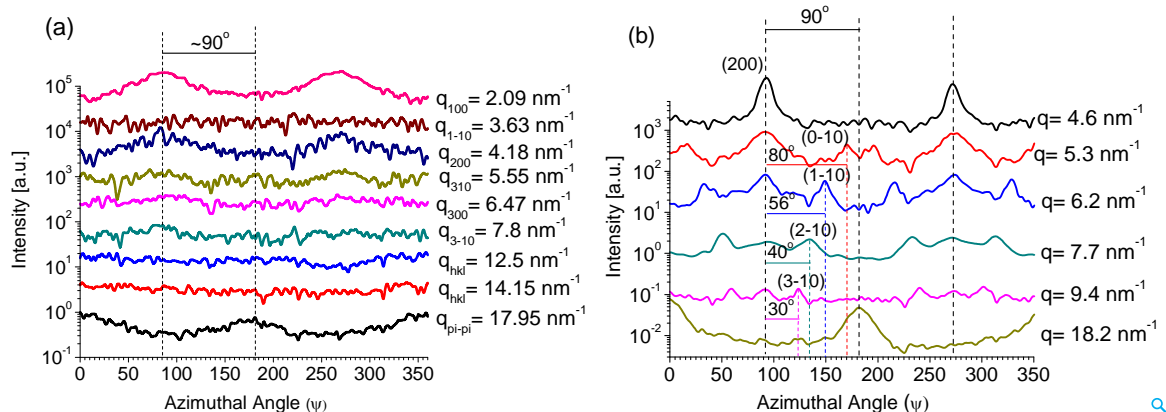
Figure 5.12: Azimuthal intensity dependence of different reflections of (a) PBI 2 and (b) PBI 3 cooled in presence of magnetic field. The $\psi = 0°$ position is on the equator on the left

Table 5.2: Comparison of calculated and experimentally determined azimuthal positions of reflections in aligned sample of PBI 3

Scattering vector q (nm^{-1}) of $(h \pm 1\ 0)$	Angle $\Delta\psi$ between (100) and $(h \pm 1\ 0)$ planes		
	Miller indices	Calculated $\Delta\psi$ (equation(5.5))	Measured $\Delta\psi$ (Figure 5.12)
5.3	(100) and $(0\bar{1}0)$	81.5°	80.0°
6.2	(100) and $(1\bar{1}0)$	60.0°	56.0°
7.7	(100) and $(2\bar{1}0)$	44.0°	40.0°
9.4	(100) and $(3\bar{1}0)$	34.0°	30.0°

molecular weight compound PBI 1 formed a crystalline phase, the OEG substituted PBI's (PBI 2 and PBI 3) and the polymer (PPerAcr) formed only a 2D liquid-crystalline structure with liquid like packing along the stacking direction. These results are in agreement with observations by Boden et al. [108], who synthesized a series of side-chain polymers containing triphenylenes units and reported that polymers in contrast to the monomers, did not form crystalline phases. Further, liquid-crystalline phases have also been observed in small molecules PBI's carrying specific branched OEG and alkyl substituents attached to the PBI cores [174]. An interesting detail of these bulk measurements is that the π-π stacking distance is found to decrease from the alkyl substituted hydrophobic PBI 1 (c= 0.360 nm) to OEG substituted hydrophilic PBI 2 (c = 0.350 nm) and PBI 3 (c = 0.346 nm) to PPerAcr (c = 0.345 nm). A summary of the lattice parameters of PBI 1, PBI 2 and PBI 3 and the side chain polymer PPerAcr is included in Table 5.3.

5.2.4 X-ray diffraction: Microstructure in thin films

Having resolved the bulk structure of perylene samples, it is important to understand the microstructures in thin films given the relevance of these materials for applications

in organic photovoltaics. Normally, the structure obtained after blade/spin coating corresponds to a quenched non-equilibrium state due to the fast evaporation of the solvent. Thermal treatment can have a drastic effect on the packing and crystalline structure of thin films which in turn affects the overall charge transport properties [40, 104].
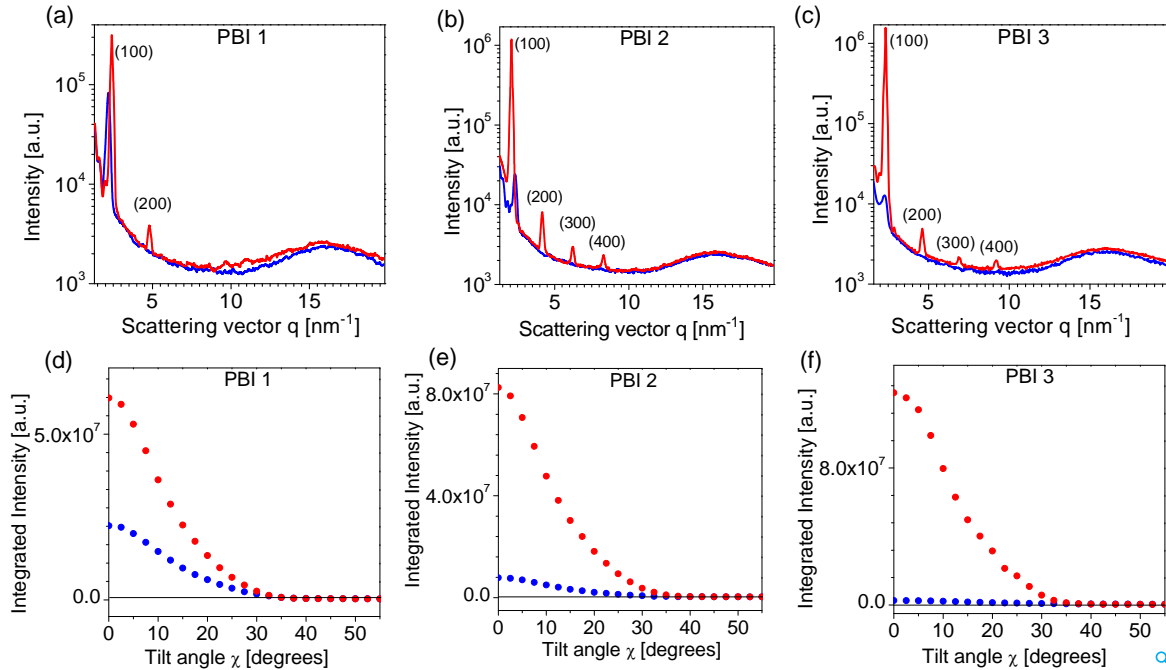

Figure 5.13: θ-2θ scans of thin films of (a) PBI 1 (b) PBI 2 and (c) PBI 3; texture scans: intensity variation with the tilt angle chi (χ) of (100) reflection for (d) PBI 1, (e) PBI 2 and (f) PBI 3 in pristine (blue) and annealed (red) films; the integrated area of the intensity curve is proportional to the total crystallinity in thin films

In order to investigate the structure and orientation distribution in thin films of PBI 1, PBI 2, and PBI 3, θ-2θ scans and texture measurements in reflection geometry were performed. While in a θ-2θ scan only the lattice planes parallel to the substrate contribute to the signal, for a tilted sample the intensity provides quantitative information on the orientation distribution of the crystals within the film.

Figures 5.13(a-c) show the θ-2θ scans performed on pristine and annealed films of PBI 1, PBI 2 and PBI 3. The scattering patterns of the pristine films show a single reflection corresponding to the (100) lattice planes with $q_{100} \approx 2$ nm^{-1}. The broad halo around q = 16 nm^{-1} originates from the glass substrate. Thermal annealing of the pristine films leads to a significant increase in the scattering intensity of the (100) reflection with a reduced width indicating an increased domain size (t_{hkl}) in the direction perpendicular to the substrate (Figure 5.14(a)), which can be evaluated quantitatively using the Scherrer equation (4.1). The crystal size increased by a factor of more than 2 for annealed films from $t_{100} \approx 40$ nm for PBI 1 to $t_{100} \approx 60$ nm for PBI 3. Thus single crystalline domains do not span over the entire film thickness. Additionally, higher order reflections (*h00*) were observed for all annealed films indicating a reduction

of disorder within the crystals. The interplanar spacing d_{100} calculated from the q value of the first Bragg reflection for the annealed films correspond well with the analysis of the bulk samples and are tabulated Table 5.3. However, in both cases i.e. in pristine and annealed films , no (001) reflection (corresponding to the π-π stacking distance) at a scattering vector q $\approx$ 18 nm^{-1} is observed. The observed increase in intensity can either be caused by an increased crystalline order, or by a narrower orientation distribution with a prevalent orientation of the (100) lattice planes parallel to the substrate, or by both.
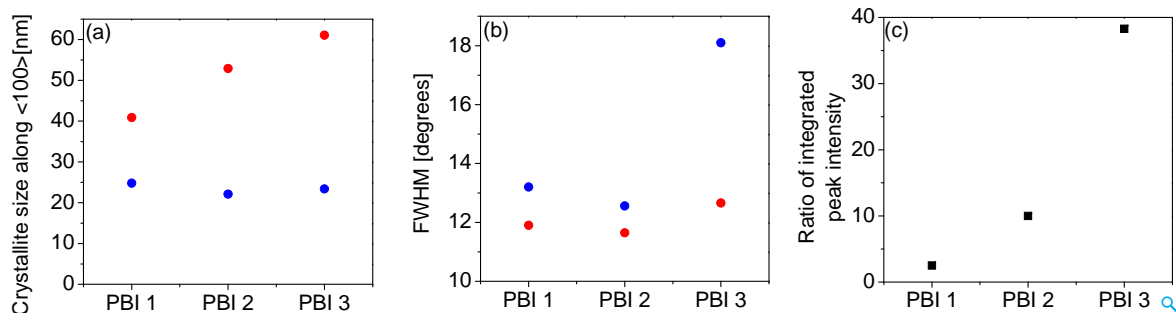

Figure 5.14: (a) Domain size along (100) direction t_{100} for pristine (blue) and annealed (red) films. (b) Full width half maximum (FWHM) of the orientation distribution of the (100) crystallographic lattice planes for pristine and annealed films and (c) the ratio of integrated peak intensities as obtained from the scans shown in Figure 5.13(d-f)

The texture scans shown in Figure 5.13(d-f) allow distinguishing between these two effects. Texture measurements were performed at a fixed angle of incidence and for a fixed detector position, corresponding to the (100) reflection as obtained from θ-2θ scan, while the polar angle χ, was varied from 0° to 55°. For each χ, the azimuthal angle ϕ was scanned over 360°. Clearly there is a strong preferential orientation of the (100) lattice plane perpendicular to the substrate. Figures 5.14(b) and (c) show the FWHM and the ratio of integrated intensity I_{int} (c.f. equation(3.3)) as obtained from the texture scans of the annealed and pristine films. The reduction in FWHM of the intensity curve for the annealed films in comparison to the pristine films demonstrates a narrower orientation distribution, most strongly for PBI 3, but it is clear that the dominant effect of annealing is a substantial increase in intensity I_{int}, i.e. crystalline order. Thus both effects, an increase in intensity as well as a narrowing of the orientation distribution were observed. Exact values are given in Table 5.3. Based on the above observations, the columns of PBI stacks (Figure 5.10 and 5.5(b)) are lying flat on the substrate, which is equivalent to an edge-on orientation of the molecules. These results are in agreement with the AFM measurements which exhibit formation of terraces. Especially for PBI 2, the surface is so well defined that terraces of (100) lattice planes with step heights of $\approx$ 3 nm can be observed [177].

Let us now investigate the thin film microstructure in PPerAcr. It should be mentioned at this point that while texture measurements can provide a quantitative information about the crystallite orientation along the substrate normal, the use of a 2D detector in a GIWAXS measurement can provide information about the crystal-
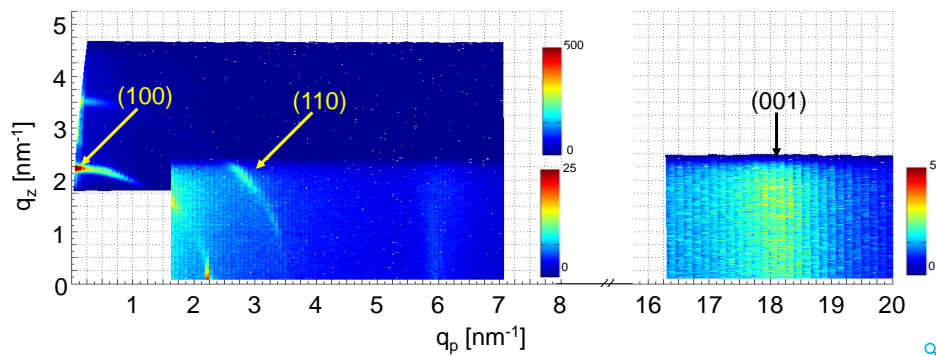
Figure 5.15: 2D reciprocal space map of PPerAcr film cooled from the melt. Indices of relevant reflections are indicated.
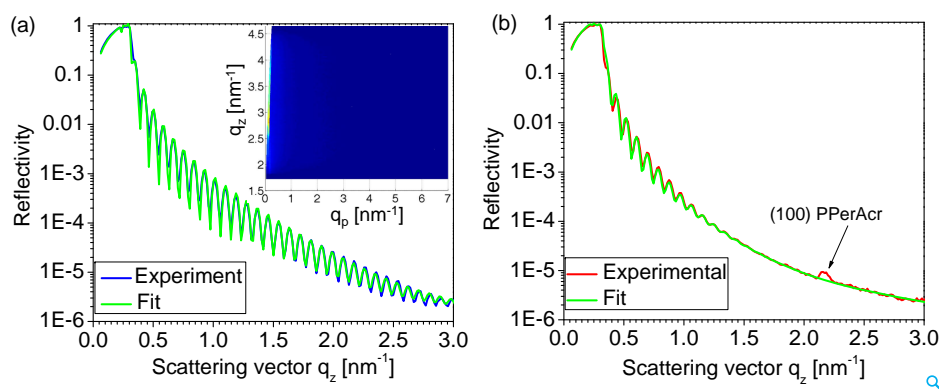

Figure 5.16: Reflectivity curves of the (a) as spun and (b) melt cooled films of PPerAcr. Both the curves exhibit Kiessig fringes at small q values which originate due to the constructive interference of x-rays at the substrate-polymer and polymer-air interface. The film thickness and surface roughness was evaluated by fitting the experimental data. The melt cooled film of PPerAcr (b) exhibits a Bragg reflection at $q \approx 2.2$ nm^{-1} corresponding to the (100) lattice planes while no such reflection is observed for the as spun films. The inset in (a) shows the reciprocal space map of the as spun PPerAcr films exhibiting a featureless scattering pattern

lite orientation (both in and out of the substrate plane). Both the measurements are equivalent to an extent that one can obtain information about the crystallite orientation distribution along the substrate normal. However, as already mentioned in the section 2.4, additional measurement in specular condition are required along with GI-WAXS measurement to obtain complete information about the crystallite orientation along the substrate normal.

Figure 5.15 shows the 2D GIWAXS reciprocal space map of a film cooled from the melt. The coordinates were calculated according to the equation(2.31). The strongest peak is the (100) reflection close to the meridian ($q_z \approx 2.25$ nm^{-1}), suggesting a preferred alignment of the corresponding lattice planes parallel to the substrate. A reflectivity curve measured on the same film is shown in Figure 5.16(b). A detailed analysis of the fringes at small q-values gives a thickness of 67 nm and a roughness of 2 nm.

As in this scattering geometry only lattice planes parallel to the substrate contribute; the single (100) peak confirms the GIWAXS results. The position of the (110) (q $\approx$ 3.4 nm^{-1}) peak in Figure 5.15 is consistent with the lattice suggested from the bulk measurements. The location of the (001) reflection along the q$_p$ axis (q$_p$ $\approx$ 18.2 nm^{-1}) indicates π-π stacking in lateral direction, i.e. edge-on, consistent with the orientation of the (100) planes. Note that the (001) is not a peak but rather a long vertical streak, also considerably broader than the other peaks. This is to be expected for a lamello-columnar liquid-crystalline structure in which the stacking of PBI cores in neighboring layers is uncorrelated and liquid-like. In stark contrast, the pattern of the as spun film (inset Figure 5.16(a)) is featureless corresponding to a quenched, completely amorphous structure. This was further supported by reflectivity measurements where no Bragg reflection corresponding to the (100) lattice planes was observed (Figure 5.16(a)).

Table 5.3: Summary of results from XRD measurements in bulk, thin films and texture scans; interplanar spacing d$_{100}$ as calculated from θ-2θ scans of PBI thin films; domain size along (100) direction t$_{100}$; increase in crystalline order upon annealing as obtained from the ratios of the integrated intensity I$_{\text{int}}$ (Figure 5.14(c)

		PBI 1	PBI 2	PBI 3	PPerAcr
Bulk	Lattice parameters	a = 2.68 nm	a =3.47 nm	a = 2.76 nm	a = 3.01 nm
		b = 1.11 nm	b = 3.47 nm	b = 1.20 nm	a = 2.15 nm
		c = 0.360 nm	c = 0.350 nm	c = 0.346 nm	c= 0.345 nm
		γ = 86.0°	γ = 60.0°	γ = 81.5°	γ = 81.0°
	Packing Packing	Lamello-columnar	Columnar-hexagonal	Lamello-columnar	Lamello-columnar
		3D crystalline	2D order	2D order	2D order
Pristine films	q_{100}	2.20 nm^{-1}	2.32 nm^{-1}	2.29 nm^{-1}	-
	d_{100}	2.86 nm	2.73 nm	2.72 nm	-
	t_{100}	24.8 nm	22.1 nm	23.4 nm	-
Thermally treated films	q_{100}	2.40 nm^{-1}	2.08 nm^{-1}	2.30 nm^{-1}	2.19 nm^{-1}
	d_{100}	2.86 nm	2.73 nm	2.72 nm	2.87 nm
	t_{100}	40.9 nm	52.9 nm	61.1 nm	19.7 nm
Texture Scan	Ratio of I$_{\text{int}}$	2.5	10.0	38.3	-

5.3 Charge transport properties

An important figure of merit for semiconductors is the charge carrier mobility. The electron mobility of PBI 1, PBI 2, PBI 3 and PPerAcr was studied by using the SCLC method. The current density-voltage (j-V) characteristics of pristine and thermally treated films of PBI 1, PBI 2 and PBI 3 and PPerAcr together with the respective fits according to the Mott-Gurney equation are shown in Figure 5.17. At high voltages ohmic injecting contacts and trap free transport can be assumed and the current mea-

sured is space-charge limited only. The charge carrier mobility was estimated by fitting the experimental data using the Mott-Gurney equation (2.36). It is well known, that
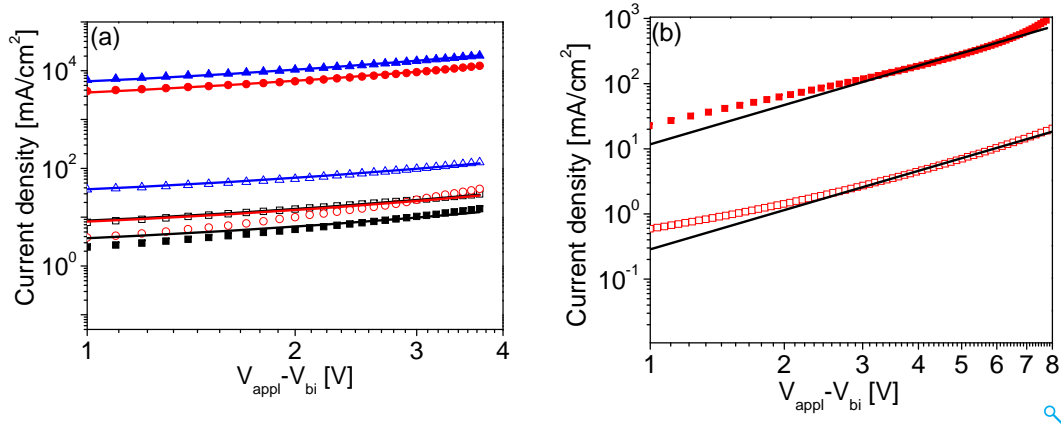

Figure 5.17: Current density-Voltage (j-V) characteristics of electron-only devices before (empty symbols) and after thermal treatment (filled symbols) of (a) PBI 1 (black squares), PBI 2 (red circles), PBI 3 (blue triangles) and (b) PPerAcr (red squares); straight lines represent the corresponding fits according to the Mott-Gurney equation; the active layer thickness L is $\approx$ 300 nm; annealing was carried out for 5 min 5 °C below the T_m for PBI 1, PBI 2, and PBI 3, while PPerAcr was cooled from the melt; the voltage applied (V_{appl}) was corrected for a built in potential (V_{bi}) of 2.2 eV resulting from the differences in work function of calcium and ITO/PEDOT:PSS

Table 5.4: Electron mobilities μ_e of pristine and annealed films of PBI 1, PBI 2, PBI 3 and PPerAcr determined by the SCLC method; the values reported represent an average over varied active layer thicknes L

Sample	Pristine films μ_e [cm^2/(V·s)]	Thermally treated films μ_e [cm^2/(V·s)]
PBI 1	3.0 x 10^{-5}	8.0 x 10^{-6}
PBI 2	2.0 x 10^{-5}	7.0 x 10^{-3}
PBI 3	6.0 x 10^{-5}	6.0 x 10^{-3}
PPerAcr	2.0 x 10^{-5}	4.0 x 10^{-4}

PBIs are good n-type materials [171]. Thus, electrons transported via the LUMO are assumed to be the majority charge carriers in these devices and the resulting mobility values are electron mobilities μ_e. In cases where the experimental data are below the expected Mott-Gurney fit, especially at low voltages, the current measured is potentially limited by charge traps. The mobility values however were calculated at higher voltages, where traps are assumed to be filled. All pristine devices exhibit electron mobilities μ_e in the range of 10^{-5} cm^2/(V·s), with μ_e (PBI 3) = 6 x 10^{-5} cm^2/(V·s) being the highest. After annealing, however, drastic changes in μ_e can be observed for all the samples under investigation. A fourfold drop in μ_e to 8 x 10^{-5} cm^2/(V·s) of

PBI 1 with two alkyl chain substituents was measured. On the other hand, μ_e of PBI 2 and PBI 3 bearing OEG side groups were improved by over two orders of magnitude to 6 x 10^{-3} cm^2/(V·s) and 7 x 10^{-3} cm^2/(V·s), respectively. Further, the melt cooled PPerAcr films also exhibited mobilities increased by an order of magnitude. The electron mobilities of the pristine and thermally treated films of the PBI samples are summarized in Table 5.4.

5.4 Correlating structural order and charge transport properties

The results from structural and transport measurements indicate that upon thermal treatment, a structural reorganization of the molecules in the film takes place, which is beneficial for charge transport only in the case of PBI 2, PBI 3 (with OEG substituents) and in the side chain polymer PPerAcr. Differences in bulk electron mobilities can be expected depending on the molecular packing, orientation and morphology of the molecules. What is now the reason for the strong changes in electron mobility upon annealing in opposing directions for PBI 1 on one hand, and PBI 2, PBI 3, and PPerAcr on the other hand?

After film preparation all the samples are in a quenched non-equilibrium state, mostly amorphous and with low molecular order. The electron mobility in this state is low and similar for all samples. Thermal treatment leads to ordering on a molecular scale throughout the whole film with a preferential edge-on orientation of the molecules and an increased crystalline order as compared to the pristine films. Even though the π-π stacking direction is parallel to the substrate, high mobilities are obtained in a direction perpendicular to the substrate for PBI 2, PBI 3 and PPerAcr. While the local packing in all materials and orientation after the thermal treatment is rather similar, PBI 1 is crystalline while PBI 2, PBI 3, and PPerAcr are liquid-crystalline without 3D correlated order. The results suggest that it is the liquid-crystalline packing which causes the strong increase in mobility in contrast to the crystalline packing of PBI 1, which goes along with the existence of domain boundaries acting as traps or barriers for transport as suggested in reference [94]. Nevertheless one cannot exclude that details of the molecular packing influencing the overlap between π-orbitals of adjacent molecules also contribute. In general, the π-orbital overlap for perylenes may not only exist along the π- π stacking direction, but also normal to it [182], which could explain the high mobility values normal to the substrate plane.

5.5 Summary

In conclusion, the phase behavior, molecular order and packing of three very similar, unsymmetrical N-substituted perylene bisimide (PBI) derivatives with the substituents varying from hydrophobic alkyl (PBI 1) to hydrophilic oligoethylenglycol (OEG) (PBI 2 and PBI 3) and a side chain polymer (PPerAcr) were studied using DSC, optical microscopy and x-ray scattering. The structural investigations revealed that the molecular

packing in the low molecular weight perylenes and the side chain polymer is similar (i.e. lamello columnar for PBI 1, PBI 3 and PPerAcr and columnar hexagonal for PBI 2). While PBI 1 was crystalline (3D ordered) at room temperature, the substitution from alkyl to OEG substituents in PBI 2 and PBI 3 resulted in a liquid-crystalline (LC) phase (2D ordered and a disordered columnar stacking) over a broad temperature range. Further, the attachment of the perylene bisimides to the polymeric chain also led to a reduced order, exhibiting an LC phase. The microstructural order in thin films revealed an amorphous/quenched state in pristine films for all the investigated materials. Thermal treatment (annealing/melt crystallization) resulted in an increased crystalline order and packing in all the films, as evident from the scattering measurements, with a dominant edge-on orientation of the perylene core. Charge transport measurements by SCLC revealed low electron mobilities ($\approx 10^{-5}$ cm^2/(V·s)) in all the pristine films due to lack of molecular ordering. Annealing the films within the LC phases led to an improvement of electron mobility of more than two orders of magnitude for PBI 2 and PBI 3, while the electron mobility of PBI 1 decreased after annealing in the crystalline phase. Electron mobilities as high as 7 x 10^{-3} cm^2/(V·s) (PBI 3) were measured. Further, thermally treated films of the side chain polymer (PPerAcr), also exhibited an improvement in the electron mobility by an order of magnitude as compared to as spun films. Thus, this study highlights that both liquid-crystalline phases and a higher order (as compared to pristine films) are beneficial for obtaining better charge transport properties.

Having investigated the microstructure of both the donor (P3HT) and the acceptor material (PPerAcr) individually, the next chapter deals with the structural investigations of the fully conjugated block copolymer consisting of the semicrystalline P3HT (main chain) as the donor block and the liquid-crystalline PPerAcr (side chain polymer) as an acceptor block.

Chapter 6

Investigation of microstructural and crystalline order in conjugated donor-acceptor di-block copolymers

The self-assembling properties of di-block copolymers having non-crystallizable blocks have been investigated extensively and have found potential applications in the field of nanotechnology [111,183]. The phase behavior in these block copolymers (in bulk [184] and thin films [185]) is well known and several methods exist to align the periodic nanoscale morphology, e.g. shear, electric fields or chemically modified substrates [26, 28,111]. Often, functionality can be introduced by incorporating blocks that show crystalline or liquid-crystalline phases. Consequently, the ordering of the individual blocks, i.e. crystallization or formation of a liquid-crystalline (LC) phase, competes with the microphase separation of the two blocks in the amorphous phase. Thus, understanding the phase behavior of block copolymers comprising two different, but functional blocks, is of major importance for the development of methods to control the material's structure on a microscopic level. For organic photovoltaics, a promising strategy to generate stable, molecularly pure, donor and acceptor domains on the scale of the exciton diffusion length ($\approx$ 10 nm), is by using the self-assembly of block copolymers comprising materials that are good electron and hole conductors in their respective LC or crystalline state.

Having addressed the issue order and packing in the hole conducting polymer P3HT and various electron accepting materials including the side chain polymer PPerAcr in the previous chapters, the focus is now to develop a thorough understanding of the phase behavior and molecular order in a fully functionalized donor-acceptor block copolymer (in bulk and in thin films) and, in turn how the microstructural properties affect the overall charge transport in thin films. This study aims to provide an insight to the following questions:

(1) What are the ordering processes involved in a block copolymer having crystalline/liquid-crystalline blocks? Does the microphase morphology as observed in classical coil-coil block copolymers also exists in such block copolymers?

(2) What is the effect of confinement on crystalline order?

(3) What is the microstructural/crystalline order and orientation in thin films and in turn how does it affects the overall charge transport properties?

The phase behavior and microstructural order in two fully functionalized donor-acceptor P3HT-b-PPerAcr block copolymers, of similar molecular weight with varying weight fraction of PPerAcr component, is investigated. The bulk and thin film microstructure is characterized using differential scanning calorimetry (DSC), x-ray diffraction (SAXS/WAXS), transmission electron microscopy (TEM), atomic force microscopy (AFM) and grazing incidence small/wide angle x-ray scattering (GISAXS/ GIWAXS). The charge transport properties are characterized using space charge limited current (SCLC) method. X-ray scattering measurements on bulk samples show that the block copolymers exhibit microphase separation in the melt state. Upon cooling confined crystallization occurs inside the microphase separated domains without destroying the microphase order. The observed microstructures fit well to the respective volume fractions and the crystalline packing within the individual blocks was analogous to those found in the respective homopolymers. The microstructural order as observed in bulk samples was found to be preserved in thin films. Further, the microstructures in the microphase separated films were found to be oriented parallel to the substrate. Besides microstructural order, thermally treated films exhibited an enhanced crystalline order and texture. The charge transport properties were found to be correlated with the microstructural and crystalline order and orientation. The unfavorable orientation of the microstructures in the microphase separated films results in reduced transport properties. These findings may pave the way for obtaining oriented, molecularly pure percolating pathways with crystalline order, optimal for achieving high device performance in organic photovoltaics.[1]

6.1 Materials and sample preparation

6.1.1 Materials

An alkyne functionalized P3HT (P3HT-alkyne 1) was synthesized via Kumada catalyst transfer polymerization followed by end capping the active chain end by reacting with ethynylmagnesium chloride [186]. The alkyne group was further reacted in a copper catalyzedazide-alkyne reaction with 2,2,5-trimethyl-3-(1-p-azidomethylphenylethoxy)-4-phenyl-3-azahexane 2 to form the alkoxyamine functionalized P3HT-macroinitiator (P3HT-macroinitator 3). The number average molecular weight of the P3HT-macroinitiator as determined by size exclusion chromatography (SEC) was 19.7 kg/mol and the polydispersity index (PDI) 1.15. According to matrix assisted laser desorption ionization mass spectrometry (MALDI-TOF MS) this corresponds to a number average molecular weight M_n of 12.4 kg/mol and about 75 repeating units. For the nitroxide mediated radical polymerization (NMRP) of perylene bisimide acrylate, the ratio of perylene bisimide acrylate monomer to P3HT-macroinitiator to free nitroxide was chosen as 99:1:0.2 in order to obtain a high percentage of PPerAcr in the block copoly-

---

[1]Partial results of this work were published in the following reference [120]
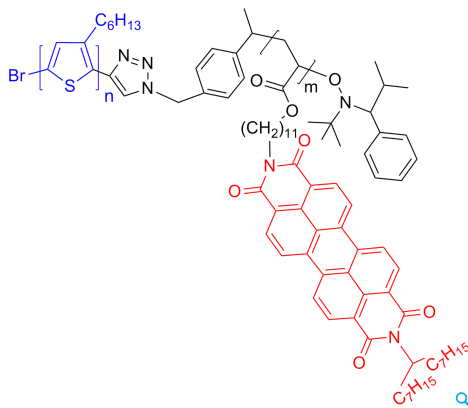
Figure 6.1: Chemical structure of the investigated block copolymer P3HT-b-PPerAcr 5, 6. The first block consists of donor poly(3-hexylthiophene) (P3HT) (blue) and the second block is built up of a flexible polyacrylate backbone with pendant side chains of perylene bisimides (red)

mer. The polymerization was performed at T = 125 °C in o-dichlorobenzene (o-DCB). The polymer was purified by dissolution in chloroform and re-precipitation in acetone. Traces of remaining monomer and macroinitiator were removed by soxhlet extraction using acetone and dichloromethane. The chemical structure of the P3HT-b-PPerAcr block copolymer is shown in Figure 6.1. Complete details of the synthesis are described elsewhere [120]. The resulting block copolymers had a M_n of 28.4 kg/mol (P3HT-b-PPerAcr 5) and 35.5 kg/mol (P3HT-b-PPerAcr 6) and low polydispersity indices (PDIs) of 1.13 and 1.19, respectively [120]. The block ratios were determined with ^{1}H-NMR spectroscopy. The weight ratio of PPerAcr was determined as 47 wt% for P3HT-b-PPerAcr 5 and 64 wt% for P3HT-b-PPerAcr 6. Using the number of P3HT repeating units as determined from MALDI-TOF MS, this corresponds to 13 and 27 repeating units of PPerAcr, respectively. The sample properties are summarized in Table 6.1. The other block copolymer P3HT-b-PPerAcr 7 (used for comparison) had a molecular weight M_n of 29.5 kg/mol (which seems to be higher than P3HT-b-PPerAcr 5, is due to the presence of triblock copolymer content, which shifts the number-average value to higher M_n values) and a PDI of 1.15. The weight percent of PPerAcr in this sample as determined from ^{1}H-NMR was 55 wt%.[2]

6.1.2 X-ray scattering and TEM on bulk samples

X-ray scattering experiments on P3HT-b-PPerAcr 5 and 6 at small and intermediate angles were performed in transmission geometry with a laboratory rotating anode setup. The wavelength used was Cu-k$_\alpha$ radiation ($\lambda = 0.154$ nm). Aluminum disks with a central hole of 0.8 mm diameter were used as sample holders. Measurements were taken on two sample stages SS1 and SS2 (c.f. Figure 3.4). The samples were mounted on a Linkam hotstage for temperature control. Heat conducting paste was used to en-

---

[2]Synthesis and molecular weight determination was done by R. Lohwasser (Univ. Bayreuth). Phase behavior analysis by XRD of P3HT-b-PPerAcr 7 was done by Peter Kohn (MLU Halle). SCLC measurements was done by C. R. Singh (TU Ilmenau)

Table 6.1: Molecular weights, polydispersities, and thermal properties of P3HT-b-PPerAcr 5, 6 and 7 as determined by SEC, MALDI-TOF MS, ^{1}H-NMR, and differential scanning calorimetry

	M_p/M_n (SEC) (kg/mol)	PDI	Repeating units P3HT (Maldi)/ PPerAcr (^{1}H-NMR)	wt% PPerAcr (^{1}H-NMR)	T_m (°C)	T_c (°C)	Microphase morphology bulk (periodicity)
P3HT-b-PPerAcr 5	31.4/28.4	1.13	75/13	47	193/228/ 239	180	Lamellar (42 nm)
P3HT-b-PPerAcr 6	36.4/35.5	1.19	75/27	64	213/232/ 246	190/177	Hexagonal (49 nm)
P3HT-b-PPerAcr 7	-/29.5	1.15	-	55	201/228/ 240	177	- -

sure good thermal contact. The samples were first heated above the complete melting temperature (T = 270 °C), and annealed for 2 hours. Subsequently, measurements were taken during a stepwise cooling run (cooling rate 10 K/min) in vacuum. Liquid nitrogen was used for controlled cooling. The exposure time for each measurement was 1200 s. The scattering patterns were corrected by subtracting empty cell measurements. A standard silver behnate sample was used for calibration. Wide angle x-ray scattering measurements at room temperature were performed on the Empyrean diffractometer operating in Bragg-Brentano geometry. The wavelength used was again Cu-k$_\alpha$ radiation (λ = 0.154 nm). X-ray scattering on P3HT-b-PPerAcr 7 was performed at the beamline ID02 of the European Synchrotron Radiation Facility (ESRF) in Grenoble. The energy of the photons was 12.540 keV (λ = 0.1 nm). Details of the measurement conditions can be found in the reference [120]. The sample preparation for TEM measurements was based on a similar thermal treatment as used for x-ray scattering. The samples were first heated above their melting temperature, in aluminum pans as used for DSC measurements, annealed and then cooled to room temperatures. The heating and cooling rate was 10 K/min. Subsequently the samples were microtomed at room temperature and stained with vapors of RuO_4. TEM measurements were performed with a JEOL 2010 and Zeiss 922 0mega.

6.1.3 Thin films for structural characterization

Thin films of P3HT-b-PPerAcr 5 and P3HT-b-PPerAcr 6 (concentration 14 mg/mL) were spin-coated (1000 rpm for 60 s) from chloroform solution on Si substrates. The substrates, having a thin layer of silicon dioxide, were cleaned with sulfuric acid prior to spin coating. The films were dried in vacuum at room temperature for several hours before subjecting to thermal treatment. Based on the DSC results, three sets of films were prepared differently for both materials. The first set was obtained directly from spin coating. The second set was heated to temperature (T = 215 °C for P3HT-b-PPerAcr 6 and T = 205 °C for P3HT-b-PPerAcr 5) above the melting point of PPerAcr, annealed for 10 minutes, and subsequently cooled. The third set was heated

to T = 250 °C, i.e. above the melting point of P3HT, annealed for 10 minutes and also cooled to room temperature. While the former treatment will be termed as annealing in 'state 1', the latter treatment will be referred as annealed in 'state 2'. The purpose of choosing such a thermal treatment is described in section 6.3.1. The heating and cooling rate was set to 10 K/min on a Linkam hotstage (in nitrogen atmosphere). The same thermal treatment was applied on all the films which were prepared for performing SCLC measurements. The film thickness as measured with AFM was 180 nm and 140 nm for P3HT-b-PPerAcr 5 and P3HT-b-PPerAcr 6 respectively.

6.1.4 Single Carrier Space Charge Limited Current Devices

Single carrier SCLC devices in diode configuration were prepared for charge carrier mobility determination of holes and electrons within the layer stack of glass/ITO/PEDOT:PSS/active layer/Au and glass/PEDOT:PSS/Active layer/Ca/Al, respectively. Polymer solution (concentration 20 mg/mL in chloroform) was spin cast (450 rpm) on top of the bottom electrodes under inert conditions. The film thickness of the devices was ≈ 300 nm. Same thermal treatment was applied to the devices as used in the films for structural investigations. Subsequently the top electrodes (Au and Ca/Al) electrodes were thermally evaporated onto the polymer layer in respective devices under high vacuum conditions. The devices were encapsulated using glass and an epoxy resin under inert environment. The devices were characterized in the dark at room temperature with a Keithley 2400 source measure unit. The charge carrier mobilities were evaluated by fitting measured j-V characteristics using equation (2.36) [135].

6.2 Microstructural order in bulk

6.2.1 Differential scanning calorimetry

The thermal behavior of the block copolymers (P3HT-b-PPerAcr 5 and 6) was investigated using DSC. The measurements show that for P3HT-b-PPerAcr 5 (Figure 6.2(a)) three melting points are observed, one at 193 °C belonging to the PPerAcr, and the other two peaks at 228 °C and 240 °C belonging to P3HT. The two melting peaks for P3HT, were also observed for the P3HT-macroinitiator 3 [120]. This behavior could either be due to the existence of a layered phase with smectic symmetry at high temperatures or, more likely, be caused by re-crystallization and a subsequent second melting during heating [73]. Only a single crystallization peak is visible at 180 °C indicating simultaneous crystallization of both blocks. To find out to what extent crystallization is influenced in the block copolymer, the value of the melting enthalpies of the respective components were considered to qualitatively estimate the crystallinity of the two blocks. For P3HT-b-PPerAcr 5, the total melting enthalpy was calculated to be 15.2 J/g from which 11.9 J/g can be attributed to the melting enthalpy of the P3HT block. Dividing this value by the melting enthalpy of pure P3HT block (P3HT-macroinitiator 3 $\Delta H_m = 21.6$ J/g) gives ratio of about 0.55, which is similar to the weight frac-
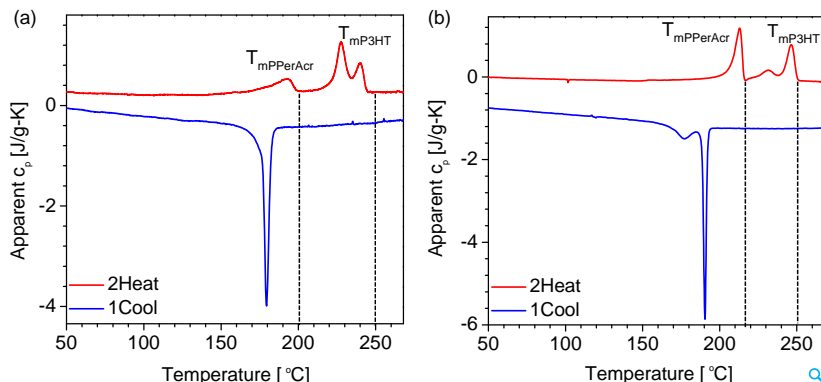
Figure 6.2: DSC heating and cooling curves (a) P3HT-b-PPerAcr 5 (b) P3HT-b-PPerAcr 6 with a scan rate of 10K/min. The dashed lines indicate the temperatures at which the thermal treatment was performed on thin films

tion of P3HT in the block copolymer (53 wt%), indicating that crystallization is not suppressed in the block copolymer P3HT-b-PPerAcr 5.

The thermal properties of P3HT-b-PPerAcr 6 (Figure 6.2(b)) were similar, however the melting temperatures were observed to be slightly higher ($T_{mPPerAcr}$ = 213 °C; T_{mP3HT} = 232 °C and 246 °C). The temperature shift is most pronounced for the PPerAcr block ($\approx$ 20 °C) which can be attributed to the higher molecular weight (27 repeating units in P3HT-b-PPerAcr 6 in comparison to 13 repeating units in P3HT-b-PPerAcr 5). Again crystallization of both the components occur over a narrow temperature range. From the two melting peaks occurring at higher temperatures the melting enthalpy of the P3HT component was determined as 8.2 J/g. This value again roughly corresponds to the weight fraction of P3HT indicating that crystallization in the block copolymer takes place basically without hindrance. To investigate the microphase behavior and crystalline order in the block copolymer, scattering measurements were performed on bulk samples.

6.2.2 Microphase morphology

From the structural investigations of the two components of P3HT-b-PPerAcr (as shown in Chapter 4 and 5), it is known that both blocks exhibit ordered structures at room temperature and melt in a similar temperature range around 200 °C - 250 °C [40, 73]. While P3HT exhibits the well known semi-crystalline morphology, PPerAcr also orders on a molecular scale; it forms a lamello-columnar liquid crystalline phase (as shown in Chapter 5). In consequence, the ordering processes of the two components (here simply called crystallization) are in competition to the classical microphase separation of the two blocks in the amorphous phase. Thus, the structure formation processes in a block copolymer having crystalline blocks could be quite different from that observed in a classical block copolymer having amorphous components. A schematic overview over the resulting different possible scenarios for structure formation is presented in Figure 6.3.

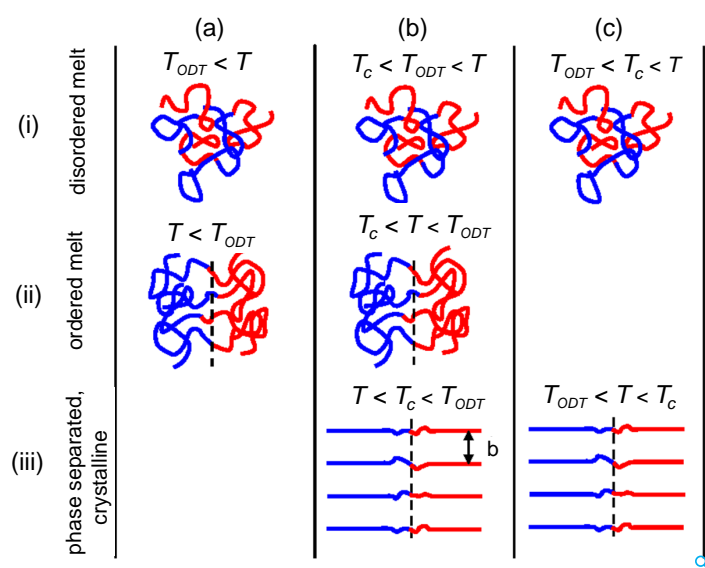The crystallization of one or both blocks could either occur from an ordered, mi-

Figure 6.3: Illustration of ordering scenarios for block copolymers upon cooling (top to bottom): (a) A block copolymer with two non-crystallizable blocks forms a disordered melt at temperatures above the order-disorder temperature T_{ODT} (i), while for $T < T_{ODT}$ (ii) in the ordered melt the well known microphase separated morphologies develop. For BCPs with two crystallizable blocks the crystallization of the individual blocks either occurs from an ordered melt (b) or directly from the disordered melt (c) depending on the relative locations of T_{ODT} and T_c. Here for simplicity the same melting temperature T_m and periodicity b was assumed for both crystalline materials
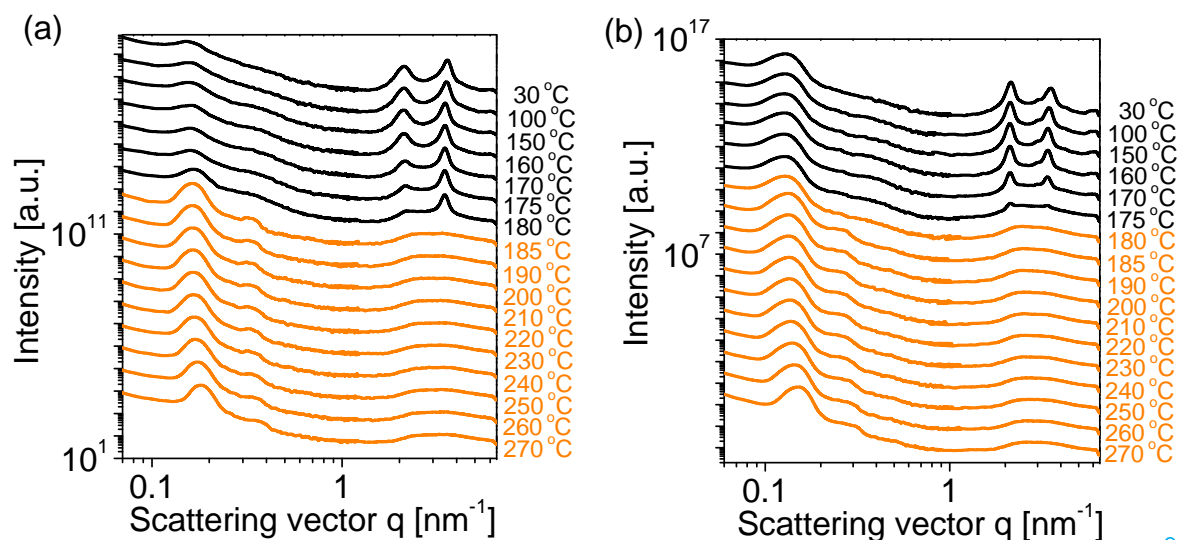

Figure 6.4: X-ray diffracton pattern of (a) P3HT-b-PPerAcr 5 and (b) P3HT-b-PPerAcr 6 recorded during a stepwise cooling from the melt. Temperatures at which the block copolymer is in the molten state are marked in orange

crophase separated melt, Figure 6.3(b), or directly from the disordered melt, as shown in Figure 6.3(c). It was interesting to see how the here used block copolymers behave. Direct evidence about structure formation processes was obtained from temperature dependent x-ray scattering. Figure 6.4 shows the x-ray pattern at small and intermediate scattering vectors of P3HT-b-PPerAcr 5 and 6 measured at different temperatures during stepwise cooling. The obtained scattering curves can be divided into two temperature ranges. At high temperatures both components are in the molten state (orange lines), below T_c crystallization of the individual components occurs (black lines).

Already in the molten state both polymers show clear indications for microphase separation. The peak at small q (q $\approx$ 0.15 nm^{-1}) whose width (FWHM = 0.03 nm^{-1}) corresponds to the resolution of the instrument with higher orders at positions reflecting the symmetry of the microphase separated structure is observed. T_{ODT} is not reached in the experimentally accessible temperature range. At the same time reflections of the crystalline phases at larger q values (q > 1 nm^{-1}) are absent. Upon cooling, below the crystallization temperature, additional reflections show up, indicating crystallization of the individual blocks. In the SAXS signal, the position of the main peak remains unchanged indicating that the crystallization of the components does not create a new microstructure. The change in intensity of the second order peak is most likely caused by additional roughness of the interface between the two components. Thus, both P3HT-b-PPerAcr 5 and 6 form a segregated system with microphase separation in both crystalline and amorphous states as per the ordering scenario shown in Figure 6.3(b).

On the contrary, the scattering pattern of P3HT-b-PPerAcr 7 (Figure 6.5(a)) exhibits the other scenario according to Figure 6.3(c), i.e. crystallization directly from the disordered melt. This conclusion follows from the analysis of the shape of the peak at scattering vector q $\approx$ 0.25 nm^{-1} in the small angle scattering regime [120]. For high temperatures, this shape is well described by the structure factor calculated by Leibler for a disordered block copolymer melt [112]. The resulting value for the incompatibility $\chi_F N$ (where χ_F is the Flory Huggins incompatibility parameter and N is the degree of polymerization) indicates consistently a disordered state. Additionally for P3HT-b-PPerAcr 7, the position of the small angle peak (q $\approx$ 0.25 nm^{-1}) shifts upon crystallization of the components to smaller q values, as shown by arrow in Figure 6.5(a), indicating that crystallization is not confined by a microphase structure. It is to be noted that this polymer P3HT-b-PPerAcr 7 contains certain amounts of triblock copolymer [120]. Generally, for given molecular weight and composition the disordered phase is more stable in triblock copolymers than in diblocks [187].

To identify the microphase structure of P3HT-b-PPerAcr 5 and 6, TEM images were taken from samples which were annealed above the melting temperature and subsequently slowly cooled to room temperature. The samples were stained with RuO$_4$, which selectively stains the P3HT phase [49]. The TEM image of P3HT-b-PPerAcr 5 (Figure 6.6(b)), shows a lamellar morphology with a periodicity of about 40 nm. A detailed analysis of the SAXS pattern shows that the same microphase structure exists in the melt state. Two reflections are visible at q values of 0.181 nm^{-1} and 0.362 nm^{-1} (Figure 6.6(a)). The ratio of 1:2 indicates a lamellar phase. The long period calculated
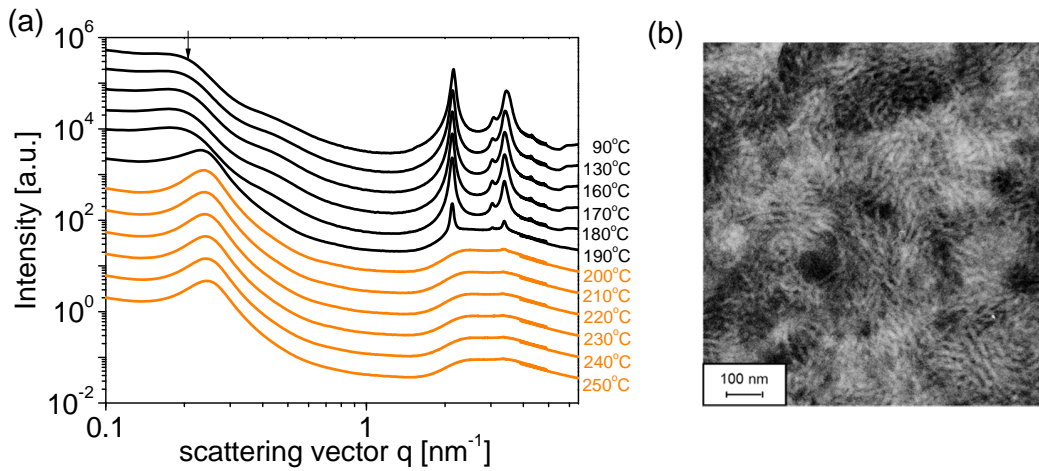
Figure 6.5: (a) X-ray scattering patterns of P3HT-b-PPerAcr 7 at the indicated temperatures during a stepwise cooling run and (b) transmission electron microscopy image at room temperature
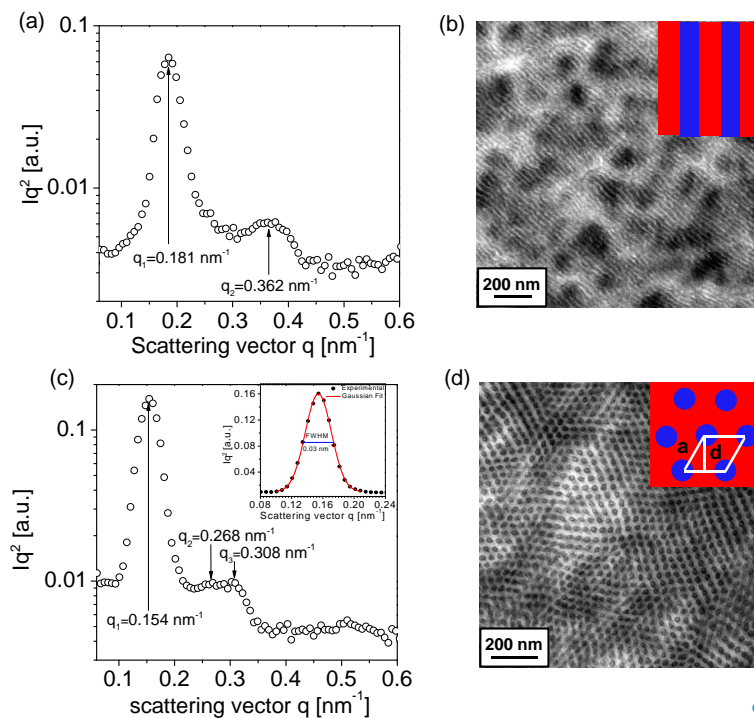

Figure 6.6: Lorentz corrected SAXS data at T = 270 °C of P3HT-b-PPerAcr 5 (a) and P3HT-b-PPerAcr 6 (c). The inset in (c) shows the main peak having a FWHM ≈ 0.03 nm^{-1} corresponding to the resolution limit of the instrument. Transmission electron microscopy image of P3HT-b-PPerAcr 5 (b) and 6 (d) obtained at room temperature in bulk samples showing a lamellar and cylindrical morphology respectively
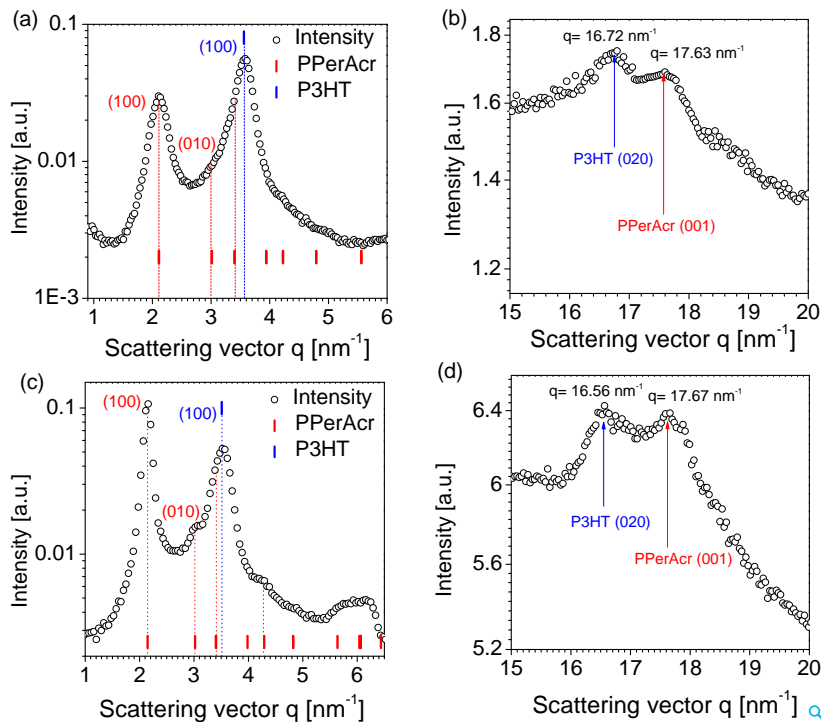
Figure 6.7: Scattering pattern for the block copolymer P3HT-b-PPerAcr 5 (top) and 6 (bottom) at 30 °C for intermediate (a), (c) and high q range (b) and (d) showing the reflections for π- π stacking, with the reflections from P3HT marked in blue and the reflections from PPerAcr marked in red

from q = 0.15 nm^{-1} at 30 °C was 42 nm and consistent with the results obtained from TEM.

For P3HT-b-PPerAcr 6, the TEM image shows hexagonally ordered dark P3HT cylinders in a bright matrix of PPerAcr (Figure 6.6(d)). An additional TEM image over a larger cross sectional area reveals the presence of both standing and lying cylinders [120]. The reflections in the SAXS pattern as shown in Figure 6.6(c) are not as well resolved, but the data are consistent with a hexagonal lattice for which reflections at positions corresponding to a ratio of $1:\sqrt{3}:2$ are expected. The spacing between the (100) planes calculated from the position of the first reflection (q = 0.127 nm^{-1} at T = 30 °C) is 49.5 nm. On the basis of this value, the lattice parameter 'a' of the hexagonal lattice is calculated to be 57 nm (inset Figure 6.6(d)). In comparison to P3HT-b-PPerAcr 5 and 6, TEM images of P3HT-b-PPerAcr 7 (Figure 6.5(b)) reveal a less ordered structure. Thus, it can be concluded that high molecular weight and absence of triblock copolymer byproducts in P3HT-b-PPerAcr 5 and 6 lead to microphase separation in the melt. The next question that arises is what is the crystalline structure of the individual components within the microphase separated domains.

6.2.3 Crystalline structure

Detailed information about the crystalline structure of the individual blocks inside the microdomains can be obtained from the scattering pattern for q > 1 nm^{-1}. Figure 6.7

shows the data for P3HT-b-PPerAcr 5 and 6 recorded at 30 °C for the intermediate and wide angle scattering angular range. While the reflections corresponding to the 2D molecular packing are observed at intermediate scattering vectors (Figure 6.7(a) and (c)), the reflections corresponding to the π- π stacking can be observed at larger scattering vectors (Figure 6.7(b) and (d)). The positions of the reflections fit to the structures known from the individual homopolymers, [40, 73] the P3HT reflections are marked in blue and the PPerAcr reflections in red. P3HT crystals can be described with the well-known orthorhombic unit cell with lattice parameters a = 1.79 nm and b = c = 0.76 nm. PPerAcr forms a lamello-columnar liquid crystalline structure with a two-dimensional oblique unit cell with lattice parameters a = 2.97 nm, b = 2.11 nm, c = 0.36 nm, and $\gamma \approx 81°$ which is in agreement with the unit cell structure of the homopolymer [40]. The unchanged crystalline structures of individual blocks, in comparison to the respective homopolymers, imply a high purity of the components in the respective domains. The crystallographic density of the unit cells was calculated as 1.06 g/cm^3 for P3HT and 1.21 g/cm^3 for PPerAcr using equation (5.1). Using the weight fractions of the block copolymers as determined from ^{1}H-NMR spectroscopy, the volume fraction of PPerAcr were estimated (equation (6.1)) as 0.44 for P3HT-b-PPerAcr 5 and 0.61 for P3HT-b-PPerAcr 6. These volume fractions and the respective lamellar and cylindrical structures are consistent with the phase diagram described for the classical block copolymer systems.

$$\phi_{PPerAcr} = \frac{M_{nPPerAcr}/\rho_{PPerAcr}}{M_{nPPerAcr}/\rho_{PPerAcr} + M_{nP3HT}/\rho_{P3HT}} \tag{6.1}$$

From the results obtained above, it is obvious to question whether the microphase morphology and crystalline order as observed in bulk samples also persists in thin films. If so, is there any preferred orientation of microstructures. For this structural investigations on thin films were performed, the results of which are presented in the following section.

6.3   Microstructure and crystalline order in thin films

6.3.1   Microphase order and orientation

Based on the DSC results, three thermodynamic states (w.r.t. crystallization)(for both P3HT-b-PPerAcr 5 and 6) could be identified namely, (i) the low temperature state where both the components are crystalline (T < T$_{mPPerAcr}$ < T$_{mP3HT}$) (ii) the intermediate temperature state where the P3HT is crystalline while PPerAcr is in molten phase (T$_{mPPerAcr}$ < T < T$_{mP3HT}$) and (iii) the high temperature state where both the components are amorphous/liquid like (T$_{mPPerAcr}$ < T$_{mP3HT}$ < T). Crystallization of both blocks occur either simultaneously (P3HT-b-PPerAcr 5) or over a very narrow temperature range (P3HT-b-PPerAcr 6). Based on the results on bulk samples, it is imperative to investigate whether the microphase morphology and crystalline order, as observed in the bulk, persists in thin films and secondly, what is the relation between the microstructural and crystalline order and orientation on the transport properties.

For this purpose three sets of films were prepared differently for both materials. The first set of films were obtained directly from spin coating. The structure in as-spun films correspond to a trapped non-equilibrium state possessing neither microphase nor crystalline order. The second set of films were prepared by heating the films to temperatures (T = 215 °C for P3HT-b-PPerAcr 6 and T = 205 °C for P3HT-b-PPerAcr 5) above the melting point of PPerAcr (but below the complete melting temperature of the block copolymer), annealing for 10 minutes and subsequent cooling. This treatment leads to crystallization of both components (P3HT crystallizes during heating while PPerAcr crystallizes during the cooling) without the formation of a well developed microphase separated structure. The third set of films was heated to T = 250 °C, i.e. above the melting temperature of P3HT, annealed for 10 minutes and subsequently cooled. This treatment leads to the formation of well developed microphase separated structure besides crystalline order.
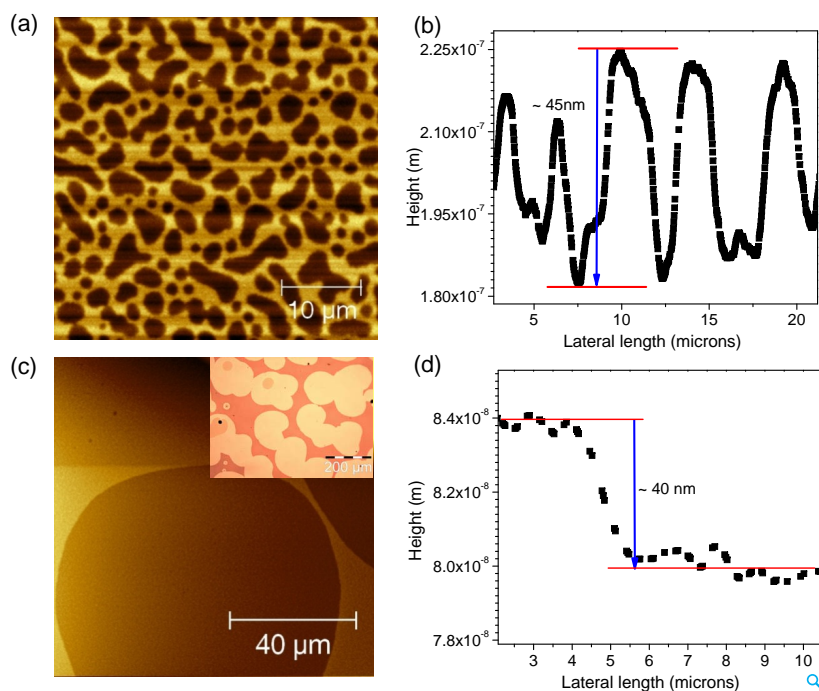
Atomic Force Microscopy

Figure 6.8: Topographic images of films annealed in state 2 exhibiting islands and holes (a) P3HT-b-PPerAcr 6 (scan area 40 μm x 40 μm) and (c) P3HT-b-PPerAcr 5 (scan area 100 μm x 100 μm). The optical microscopic image also exhibit the presence of such structures (see inset in (c)). The formation of such structures is typical for parallel orientation of the microstructure with respect to the substrate. The corresponding profile scans revealing step heights of $\approx$ 45 nm and 40 nm for P3HT-b-PPerAcr 6 (b) and P3HT-b-PPerAcr 5 (d) are in good agreement with the periodicity of the microstructures obtained from bulk measurements

The topographic AFM images of P3HT-b-PPerAcr 5 and 6 annealed in state 2 are shown in Figure 6.8. Both P3HT-b-PPerAcr 5 and 6 exhibit the morphology of islands and holes typical for BCP's in thin films. The presence of such relief features give a first
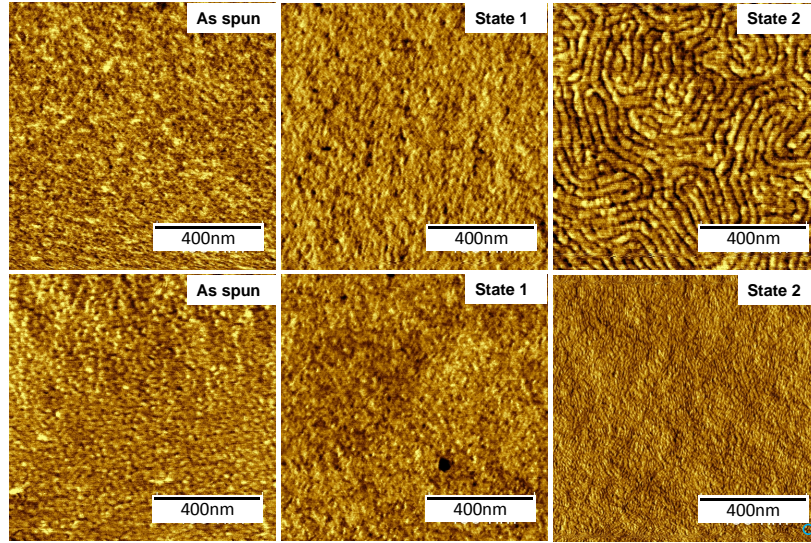
Figure 6.9: Phase images of as-spun and annealed films in state 1 and 2 of P3HT-b-PPerAcr 6 (top) and P3HT-b-PPerAcr 5 (bottom). No microphase separation is observed in as cast and films annealed in state 1. While flat lying cylindrical microstuctures in P3HT-b-PPerAcr 6 films annealed in state 2 are observed, no microstructures are observed in the P3HT-b-PPerAcr 5 films annealed in state 2 consistent with parallel orientation of lamellar microdomains. The images are scanned over film area of 1 μm x 1 μm. The scale bar is 400 nm.

indication of microphase separated states with their orientation parallel to the substrate [28, 188, 189]. The formation of such structures is a consequence of the mismatch between film thickness and periodicity of the microstructure. The profile scans, as shown in Figure 6.8(b) and (d), across such structures give step heights of $\approx$ 40 nm (P3HT-b-PPerAcr 5) and $\approx$ 45 nm (P3HT-b-PPerAcr 6) which is in fair agreement with the corresponding bulk periodicity as obtained from SAXS. The optical microscopy images of P3HT-b-PPerAcr 5 (inset Figure 6.8(c)) also reveal the presence of large islands and holes in line with the AFM measurements. In order to gain an insight to the wetting behavior of P3HT-b-PPerAcr 5, thickness measurements were performed on the films annealed in state 2. The quantization rule for stable film thickness for symmetric and asymmetric wetting for a lamellar microstructure oriented parallel to the substrate is given by nL_o and $(n+1/2)L_o$ respectively where n is an integer and L_o corresponds to the long period of the microstructure [185]. The film thickness of annealed films (state 2) of P3HT-b-PPerAcr 5, as measured by AFM, was found to be $\approx$ 180 nm which corresponds to the quantization rule for the case of asymmetric wetting with n = 4. This would imply that different components wet the substrate/air interface. Further, x-ray photoelectron spectroscopy (XPS) measurements (not presented here) show an enhanced signal from Oxygen and Nitrogen and a simultaneous decrease in the signal from Sulfur in films annealed in state 2 as compared to the as-spun (non microphase separated) films indicating the presence of PPerAcr layer at the air/film interface. Thus, in the lamellar microphase separated films of P3HT-b-PPerAcr 5, while P3HT layer wets the substrate interface, PPerAcr wets the air interface.

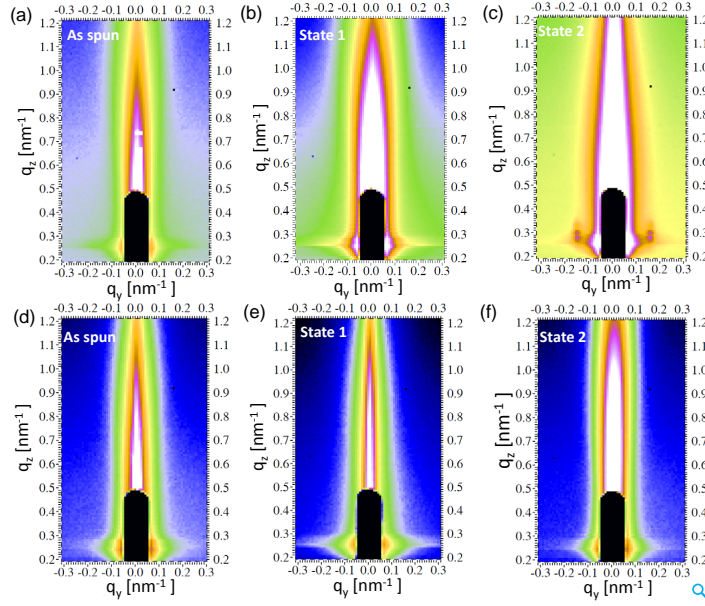The corresponding AFM phase images of P3HT-b-PPerAcr 5 and 6 (over a smaller

Figure 6.10: 2D GISAXS scattering patterns of P3HT-b-PPerAcr6 (top) and P3HT-b-PPerAcr 5 (bottom). The specular beam is masked with a rod like beam stop. A reflection along the q_y axis is observed for P3HT-b-PPerAcr 6 films annealed in state 2 (c) indicating lateral microphase order while no such reflection was observed in as-spun films (a) and films annealed in state 1 (b). However, for P3HT-b-PPerAcr 5 films no reflection was observed along the q_y axis for the films annealed in state 2 (f) consistent with the fact that the lamellar microstructures are aligned parallel to the substrate

scan area) for the different thermally treated films are shown in Figure 6.9. For the as-spun films (both P3HT-b-PPerAcr 5 and 6) no well-defined structures were observed as the structure obtained after spin casting corresponds to a non-equilibrium state trapped by the fast drying process. No significant changes in the surface morphology of the films annealed in state 1 (as compared to as-spun films) for the respective block copolymers could be observed indicating a non well-developed microphase morphology. In stark contrast to the as-spun and films annealed in state 1, P3HT-b-PPerAcr 6 films annealed in state 2 exhibits well-defined flat lying cylindrical microstructures indicating microphase separation. However, no large scale microstructures were observed for P3HT-b-PPerAcr 5 films annealed in state 2. This is consistent with the parallel orientation of the lamellar microstructure with respect to the substrate.

GISAXS

Since AFM probes only the surface morphology of films, the internal microstructure in thin films was investigated using GISAXS. The transformation equations used for data conversion are described in section 2.4.2. The 2D GISAXS patterns of P3HT-b-PPerAcr 5 and 6 films are shown in Figure 6.10. The scattering patterns exhibit a streak like reflection along the vertical axis (at $q_y = 0$) due to the substrate. The specularly reflected peak is masked by a beam stop. An intensity maximum (yoneda peak) at $q_z \approx 0.25$ nm^{-1} (exit angle (α_f) equal to the critical angle of reflection (α_c) of the material) is observed [131]. The scattering pattern of P3HT-b-PPerAcr 6 films
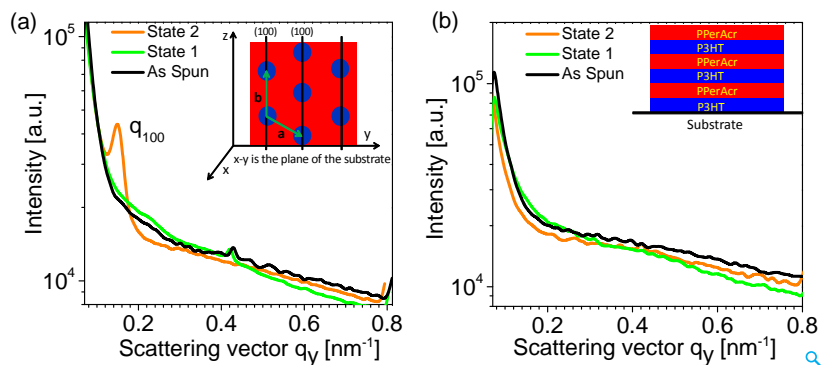
Figure 6.11: Horizontal profile cuts at the yoneda position (a) P3HT-b-PPerAcr 6 (b) P3HT-b-PPerAcr 5. The inset shows the schematic of the lattice orientation of microphase structure

annealed in state 2 (Figure 6.10(c)) exhibit a reflection along the q_y axis ($\alpha_f = \alpha_c$) at $q_y = 0.146$ nm^{-1} indicating a lateral microphase structure in the films. The periodicity of the microstructure corresponding to this reflection is calculated to be $2\pi/q_y = 43$ nm which compares reasonably well with bulk periodicity value of 49 nm [120]. On the contrary, besides the specular reflection, the as-spun films and films annealed in state 1 show no reflections (neither along q_z nor along the q_y axis) suggesting a non-microphase separated morphology. Figure 6.11(a) gives the horizontal profile scan of the 2D GISAXS pattern at the yoneda position for different thermally treated films of P3HT-b-PPerAcr 6. The profile scan exhibits a Bragg reflection at $q_y = 0.146$ nm^{-1} (as mentioned above) for the films annealed in state 2 while no such reflection is observed in the as-spun films and the films annealed in state 1. It is known from AFM (Figure 6.9) and bulk measurements (TEM) (Figure 6.6(d)) that P3HT-b-PPerAcr 6 forms cylindrical microphase separated structures. The appearance of this reflection along the q_y axis is consistent with the findings from AFM that the cylindrical microstructures are oriented with their long axis lying in the plane of the substrate. A schematic of the proposed lattice orientation of the microstructure in films annealed in state 2 is shown in the inset of Figure 6.11(a).

The 2D GISAXS pattern of P3HT-b-PPerAcr 5 (Figure 6.10(d-f)) reveal no reflections neither in the as-spun films nor in the annealed films. Unlike P3HT-b-PPerAcr 6, the horizontal profile cuts for P3HT-b-PPerAcr 5 (Figure 6.11(b)) at the yoneda position revealed no reflection along the q_y axis in the films annealed in state 2. The absence of any such reflection is consistent with the results from AFM and optical microscopy results namely a lamellar microstructure oriented parallel to the substrate. The orientation of microphase separated structures in thin films is known to depend on the energetics/chemical nature of the surfaces that bound the film [185, 190]. Thus, the preferential interfacial interactions of the blocks, for both P3HT-b-PPerAcr 5 and 6, with the air/substrate interface forces the alignment of the microstructures parallel to the substrate.
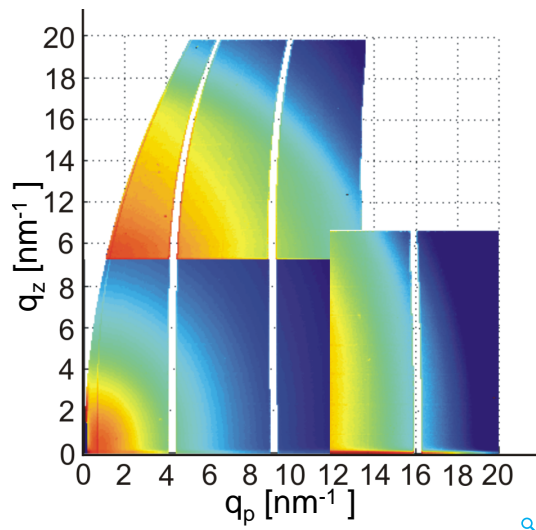
Figure 6.12: A representative 2D GIWAXS reciprocal space map of as-spun P3HT-b-PPerAcr 6 films exhibiting a diffuse scattering pattern corresponding to an amorphous state. The scattering pattern of P3HT-b-PPerAcr 5 as-spun films was similar.

6.3.2 Crystalline order and texture

The crystalline order and texture in thin films was investigated using GIWAXS. The schematic of the GID geometry and the transformation equations used for data conversion from pixels to reciprocal space vectors are given by equation (2.31). The intensities in each data set were normalized with respect to the exposure time. The color (log) scale in each region of measurement is different and chosen such that the reflections at expected q positions are easily visible. The same color scale is kept for the same region for the different thermally treated films. The scattering pattern of the as-spun films for both P3HT-b-PPerAcr 5 and 6 exhibited a diffuse scattering pattern which corresponds to a quenched/amorphous state obtained after spin coating. A representative scan of the as-spun film of P3HT-b-PPerAcr 6 is shown in Figure 6.12. On the other hand, the GIWAXS pattern of all the thermally treated films exhibited distinct Bragg reflections corresponding to individual components as shown in Figure 6.13 and 6.14, indicating crystalline order. The observed Bragg reflections are at the same scattering vector positions as known from respective homopolymers. Generally, for the films annealed in state 1, crystallization of P3HT either occurs during the heating or annealing which hinders the formation of any long range microstructural order; PPerAcr crystallizes during cooling. On the other hand, in the films annealed in state 2, crystallization occurs during cooling after formation of a well-defined microphase structure in the melt state.

Besides crystalline order, the 2D GIWAXS pattern of thermally treated films give indications of a strong crystalline texture. Before starting the analysis let us recall that as homopolymers both blocks show an edge-on orientation in thin films, i.e. the (100) reflection is observed on the q_z axis (cf. Figure 4.6 and 5.15). We first discuss the crystalline texture in films annealed in state 1 (no well-defined microphase structure).
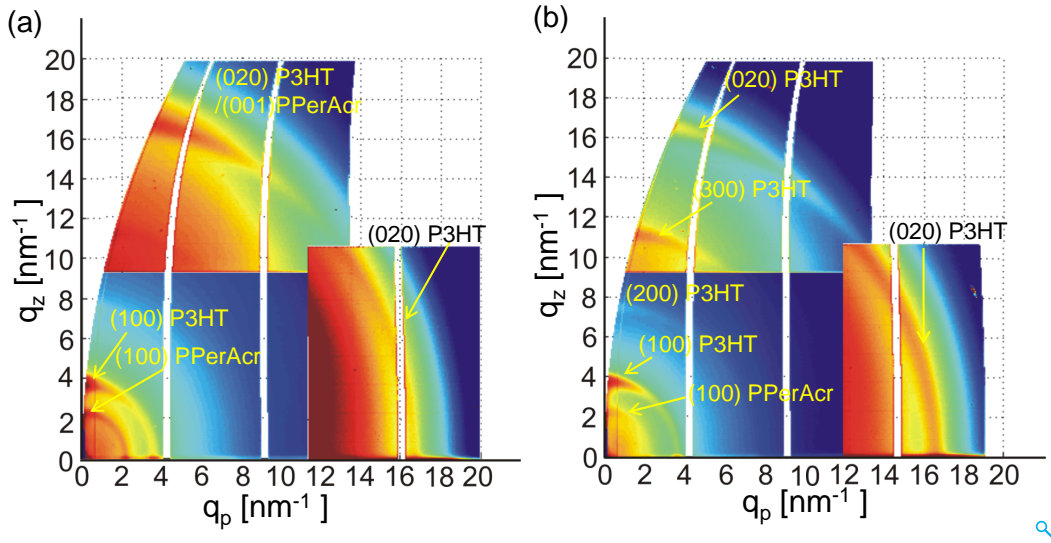
Figure 6.13: 2D GIWAXS reciprocal space maps of films annealed in state 1 of (a) P3HT-b-PPerAcr 6 and (b) P3HT-b-PPerAcr 5. Bragg reflections from the respective components i.e P3HT and PPerAcr are indicated with arrows

The GIWAXS pattern for P3HT-b-PPerAcr 6 and 5 is shown in Figure 6.13(a) and (b) respectively. We begin with the P3HT-b-PPerAcr 6 sample. Bragg reflections from the (100) lattice planes of PPerAcr and P3HT show intensity distributed over the entire azimuthal angular range (meridional to equatorial position) with intensity maximum close to the q_z and q_p axis. In line with the observations one would expect that the (020) reflection of P3HT and (001) reflection of PPerAcr, both corresponding to the π-π stacking also exhibit maxima at the same positions. But, as these latter reflections are broad and therefore difficult to resolve only the maximum close to the meridian is clearly visible, for the equatorial position the reflections are in addition close to the detector edge. A similar scattering pattern for sample P3HT-b-PPerAcr 5 (i.e. again maxima for the dominant reflections close to the q_z and q_p axis) was observed . Here, due to a smaller PPerAcr content in the block copolymer, the (020) reflection of P3HT dominates while the (001) reflection of PPerAcr is too weak to be observed. All together, the films show an anisotropic crystalline texture which is different from the texture observed for the homopolymers and without one single preferred crystalline orientation.

Let us now analyze the crystalline texture for the films annealed in state 2 as shown in Figure 6.14. Generally the observed scattering patterns are similar to what was discussed before, showing maxima of the dominant (100) reflections on the meridian and on the equator. But, as a general feature the reflections are more narrow, indicating larger crystalline domains and in most cases the orientation seems better defined. For P3HT-b-PPerAcr 6 both blocks show a dominant edge-on orientation with the (100) reflection on the meridian. This was further supported by the observance of (100) reflection from PPerAcr and P3HT in the reflectivity and θ-2θ measurements (Figure 6.15(a)). The other component of the orientation distribution ((100) on the q_p axis) is much weaker and only visible for the majority component PPerAcr. The (001)
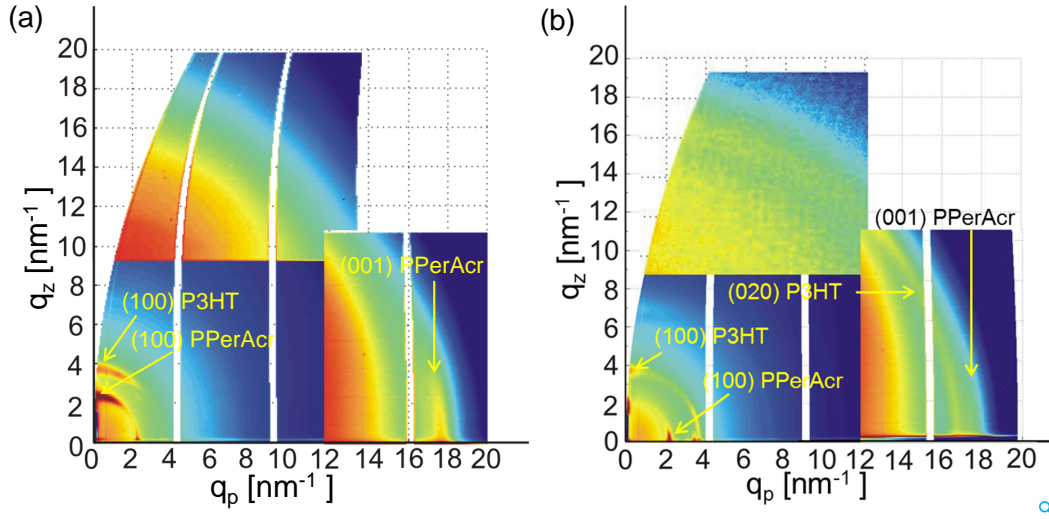
Figure 6.14: 2D GIWAXS reciprocal space maps of films annealed in state 2 of (a) P3HT-b-PPerAcr 6 and (b) P3HT-b-PPerAcr 5. Bragg reflections from the respective components i.e P3HT and PPerAcr are indicated with arrows

reflection corresponding to the π-π stacking of PPerAcr was observed on the q_p axis ($q_p \approx 18$ nm^{-1}). For the PPerAcr block such an orientation could be expected as PPerAcr forms a continuous phase, a dominant edge-on orientation corresponds to the observation made in the homopolymer films [40]. The P3HT component on the other hand displays a similar orientation, obviously only weakly influenced by the confinement within the cylinders of the microphase structure which are parallel to the substrate.

The texture observed in films of the P3HT-b-PPerAcr 5 is quite different and obviously strongly influenced by the microphase structure which in this case, consists of lamellae parallel to the substrate. Here the (100) reflection of PPerAcr exhibits a maximum on the q_p axis with only a smaller signal on the q_z axis (Figure 6.14(b)). This was consistent with the reflectivity measurements where no (100) reflection from PPerAcr was observed (Figure 6.15(b)). The (001) reflection corresponding to the π-π stacking of PPerAcr was very weak and observed along the q_p axis. For the (100) reflection of P3HT the situation is similar. The measurement corresponding to higher scattering vectors along the q_z axis also exhibits a broad intensity at $q_z \approx 16.6$ nm^{-1}. Consequently both components have a mixed orientation distribution with crystals having the a-axis dominantly parallel but also with a smaller fraction perpendicular to the substrate. Obviously the microphase structure disturbs the orientation preferred by the substrate and causes a dominant flat on orientation consistent with a perpendicular orientation of the chains caused by the strongly oriented lamellar microphase structure. In conclusion, we observed that the crystalline texture in the crystalline/liquid-crystalline block copolymer P3HT-b-PPerAcr can be strongly affected by confinement effects in films having long range microstructural order. Figure 6.16 gives a schematic overview of the observations made for the samples with different structure and thermal treatment.

Having investigated the microstructural order in bulk and thin films, an important figure of merit is the charge transport properties. The following section describes the
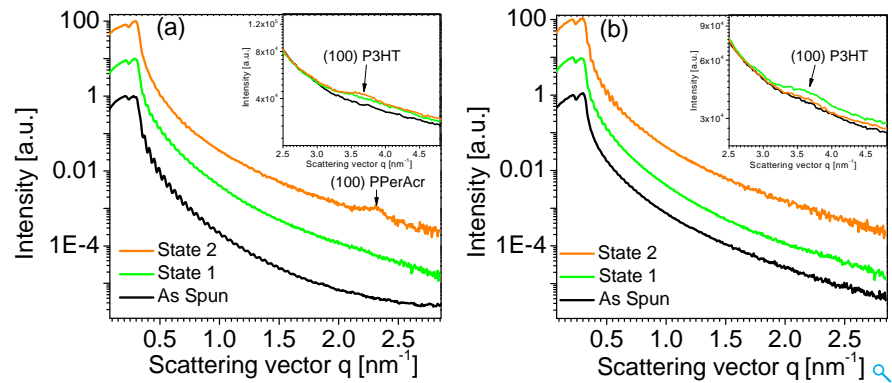
Figure 6.15: Reflectivity curves (a) P3HT-b-PPerAcr 6 (b) P3HT-b-PPerAcr 5 of different thermally treated films. The appearance of (100) reflection corresponding to PPerAcr in the films annealed in state 2 (c.f. (a)) indicates the orientation of 'a' axis perpendicular to substrate. However no such reflection is observed in (b) indicating that the a axis is not perpendicular to the substrate. The inset shows the θ-2θ scans showing a broad peak corresponding to (100) reflection from P3HT
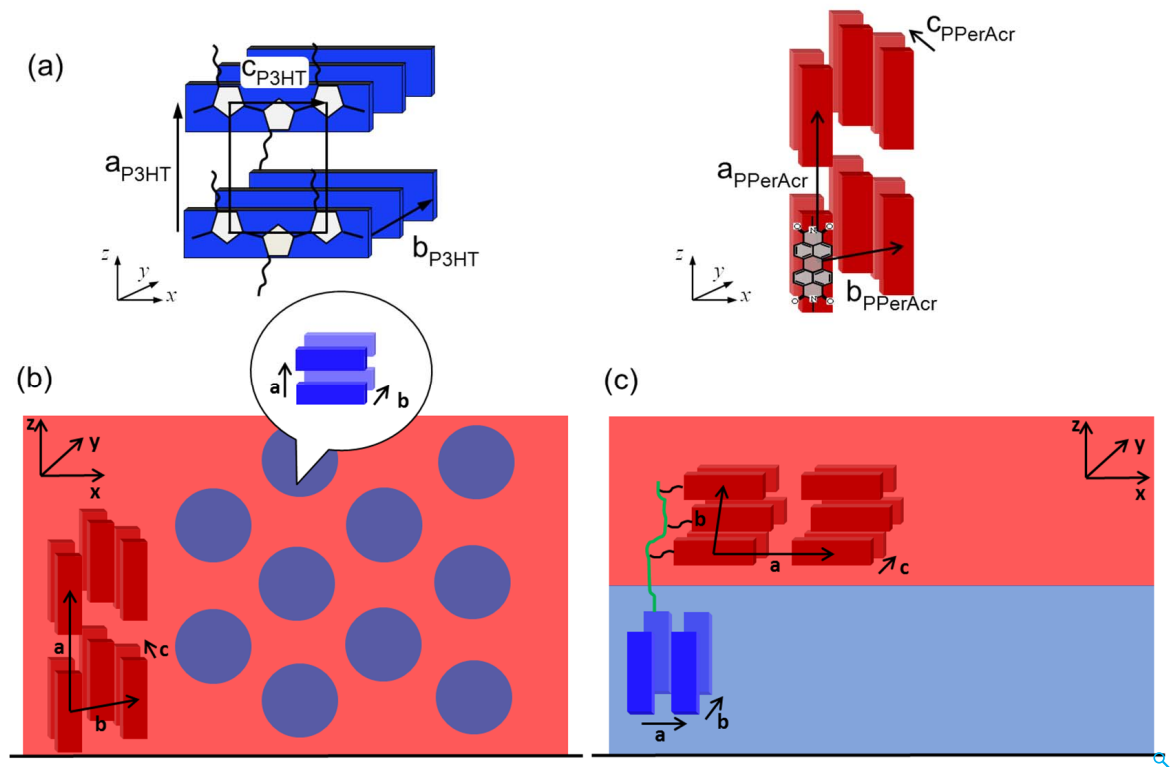

Figure 6.16: (a) Schematic illustration of the unit cell structure of P3HT (orthorhombic) (left) and PPerAcr (monoclinic) right as observed in pure homopolymers. Microstructural and crystalline order and orientation in the films annealed in state 2 for (b) P3HT-b-PPerAcr 6 and (c) P3HT-b-PPerAcr 5 illustrating flat lying cylindrical and lamellar microstructures respectively. For P3HT-b-PPerAcr 6, both PPerAcr and P3HT crystallites adopt a dominant edge on orientation with the orientation of P3HT weakly influenced by the confinement within cylindrical domains. On the other hand, for P3HT-b-PPerAcr 5, the dominant orientation in PPerAcr and P3HT crystallites is with the 'a' axis of PPerAcr aligned parallel to the substrate arising due to the conformational constraint of the polymeric backbone induced by the parallel orientation of lamellar microstructure

results obtained from the transport measurements on the devices made from these block copolymers.

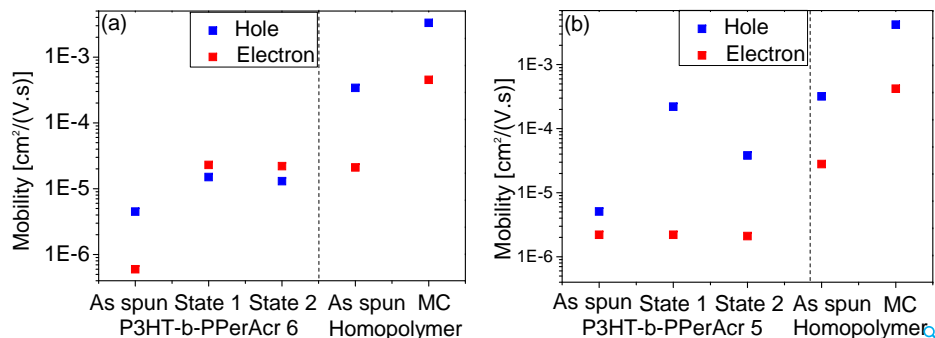### 6.3.3 Charge transport properties

Figure 6.17: SCLC mobilities of holes (blue) and electrons (red) for as cast and thermally treated (annealed in state 1 and state 2) films of (a) P3HT-b-PPerAcr 6 and (b) P3HT-b-PPerAcr 5. SCLC charge carrier mobilities in as cast and melt cooled films of pristine homopolymer (P3HT and PPerAcr) are shown on the right side of dashed line in each graph for comparison

The SCLC charge carrier mobility of holes and electrons were determined in as-spun and thermally treated films of P3HT-b-PPerAcr 6 and P3HT-b-PPerAcr 5 by fitting measured j-V characteristics of single carrier devices as per equation (2.36). Figure 6.17 summarizes the charge carrier mobilities of holes and electrons in P3HT-b-PPerAcr 6 and P3HT-b-PPerAcr 5 films and compares them to the values as measured in pure homopolymer films. The electron and hole mobilities as measured in the as-spun, pure homopolymer films of PPerAcr and P3HT 12 [157] were found to be 2.8 x 10^{-5} cm^2/(V·s) and 3.2 x 10^{-4} cm^2/(V·s) respectively. Upon crystallization from melt (MC), both electron and hole mobilities increased by an order of magnitude. These findings are in congruence with previous results on the respective homopolymers [157](c.f .Table 5.4). Interestingly, the charge carrier mobilities as measured for homopolymes were not preserved in the studied BCPs. The charge carrier mobility of both electrons and holes in as-spun block copolymers films (P3HT-b-PPerAcr 5, 6) were around two orders of magnitude less than those obtained in as-spun pure homopolymer films. The strongly reduced mobilities in the block copolymer films in comparison to the pure homopoly-mers could be due to the intermixed morphology of donor-acceptor phases that hinders direct percolation pathways between the two electrodes. This was supported by the highly quenched PL signal (results not shown) for the as-spun block copolymer films. It is known that charge transport in blended morphologies depend on the volume fraction and that the charge carrier mobility can be reduced up to one order of magnitude in 50:50% blend devices as compared to pure material devices [191, 192]. The ratio of hole mobility to electron mobility in as-spun P3HT-b-PPerAcr 6 film was similar to that in pure homopolymer films i.e. the hole mobility was found to be an order of magnitude higher than the electron mobility. Upon annealing in state 1, an increase

in both, electron and hole mobility was observed in P3HT-b-PPerAcr 6 films as compared to charge carrier mobilities in the as-spun block copolymer films (Figure 6.17(a)). The increase in the electron mobility was around two orders of magnitude and it was comparable to that of in pure PPerAcr as-spun films due to a richer PPerAcr phase. The hole mobility values are still one order of magnitude lower than those observed in the as-spun pure homopolymer P3HT films. However, in films annealed in state 2, no further improvement in the charge carrier mobilities of both holes and electrons was observed. Although PPerAcr forms the continuous phase in P3HT-b-PPerAcr 6, the charge carrier mobilities of electrons is still one order of magnitude lower as compared to the electron mobilities in melt crystallized pure PPerAcr films .

Analogously, reduced charge carrier mobility values were also obtained in the as-spun P3HT-b-PPerAcr 5 films (Figure 6.17(b)) as compared to the pure as-spun homopolymer films. Annealing the films in state 1 resulted in an increased hole mobility by two orders of magnitude due to a richer P3HT phase in P3HT-b-PPerAcr 5. The hole mobility in films annealed in the state 1 was comparable to that of in as-spun pure P3HT films. On the contrary, we do not observe any significant variation in the electron mobility as compared to as-spun films. Upon annealing in the state 2, a significant drop in the hole mobility was observed while the electron mobility remained almost constant.

Let us now try to correlate the structural properties with the transport properties of the investigated block copolymers. The absence of any crystalline order, and a finely intermixed morphology of the donor acceptor phases (absence of percolating pathways) in the as-spun films results in very low charge carrier (electron/hole) mobilities. The presence of a continuous microstructure and improved crystalline order in the non microphase separated (annealed in the state 1) BCP films (P3HT-b-PPerAcr 5 and 6) results in significantly enhanced charge carrier mobilities as compared to as-spun films. The increase in the electron/hole mobility is more pronounced for the dominant phase in the BCP (i.e. electron mobility for P3HT-b-PPerAcr 6 and hole mobility for P3HT-b-PPerAcr 5). Further enhancement in the charge carrier mobilities in P3HT-b-PPerAcr 6, despite an increased crystalline order in films annealed in state 2, is limited due to the misoriented pathways formed by the flat lying cylindrical microstructures. This effect was found to be more prominent for the hole mobilities in P3HT-b-PPerAcr 5 films. The drastic reduction in the hole mobilities in the P3HT-b-PPerAcr 5 films annealed in the state 2 could be attributed to the unfavorable orientation of the lamellar microstructure oriented parallel to the substrate which renders disruptive percolating pathways for the efficient movement of the charge carriers to the respective electrodes. Hence although the block copolymer films, annealed in the state 2, fulfill all the pre-requisites namely: crystalline order, nanostructured interfaces and a percolating pathway; the misoriented microstructures aligned parallel to the substrate is one of the key limitations in achieving high transport properties.

6.4 Summary

In conclusion, the structural investigations on bulk samples reveal that an increased molecular weight (correspondingly a higher $\chi_F N$) and high purity (absence of triblock copolymer content) in P3HT-b-PPerAcr 5 and 6 leads to microphase separation in the melt. While P3HT-b-PPerAcr 5 formed a lamellar morphology, P3HT-b-PPerAcr 6 formed cylindrically microphase separated structures. Confined crystallization of the individual components occurs within these microphase separated structures without altering the microphase morphology. Thus, for the first time lamellar and cylindrical microstructures as known from block copolymers with amorphous blocks were obtained for a semiconducting donor-acceptor block copolymer having crystalline/liquid-crystalline components. The crystalline structures of the individual components i.e. P3HT and PPerAcr are unchanged in comparison to the respective homo-polymers. Further, the microstructures obtained in bulk samples were found to be preserved in thin films. The as-spun films for both P3HT-b-PPerAcr 5 and 6 exhibited no microstructural order and were amorphous. On the other hand, thermal annealing led to an increased crystalline order. While films annealed in state 1 show no long range order, films annealed in state 2 exhibit flat lying microstructures (lamellar for P3HT-b-PPerAcr 5 and cylindrical for P3HT-b-PPerAcr 6) besides crystalline order. The crystalline texture in thermally treated films was found to be strongly affected by confinement effects in films having long range microstructural order. The transport properties in the semiconducting conjugated block copolymer were found to be strongly dependent on the microphase morphology and crystalline order. While, no microphase separation and disordered state in as-spun films resulted in poor transport properties, increased crystalline order and a continuous microstructure in films annealed in state 1 resulted in higher charge carrier mobilities. Misoriented microphase separated structures in films, annealed in state 2, provided disrupted pathways for the charge carriers resulting in reduced charge carrier mobilities. Therefore, both crystalline order and oriented continuous percolating pathways are essential for achieving high charge carrier mobilities. The results presented in this chapter demonstrates that the self-assembling properties of the block copolymer can be used to produce well defined donor-acceptor nanostructures. However, they should be oriented in a favorable way to achieve better device performances relevant for organic photovoltaics.

Chapter 7

Summary

In this thesis various material systems involving one of the most standard hole conductor poly(3-hexylthiophene) (P3HT), electron acceptor materials containing perylene derivatives and fully functionalized donor-acceptor block copolymers incorporating P3HT and poly(perylene bisimide acrylate) (PPerAcr) for applications in organic solar cell were studied. Fundamental aspects of structure formation processes, phase behavior and microstructural order in these semiconducting materials were investigated. Several techniques involving x-ray scattering (in particular grazing incidence), surface imaging (AFM), calorimetry (DSC) and electron/optical microscopy, were employed to get a detailed knowledge of structure and morphology in bulk and thin films, which is of utmost importance for understanding the transport properties relevant for solar cells.

Prior to the study of complex self-assembling properties and microstructure of block copolymers involving semi-crystalline/liquid-crystalline components, individual blocks were investigated for their structure and phase behavior independently. Thin film investigations on P3HT homopolymer of different molecular weights revealed that crystallization from the melt resulted in a substantial increase in crystalline order and a relatively narrower crystallite orientation distribution as compared to the as-cast films. The dominant orientation of the crystallites was found to be edge-on with the 'a' axis of P3HT aligned perpendicular to the substrate. The long period (periodicity of the crystalline plus amorphous regions) increased with increasing molecular weight reaching a maximum for an intermediate molecular weight (P3HT 12) and then decreased for higher molecular weights where chain folding sets in. In congruence to the increase in crystalline order, in the melt-crystallized films, enhanced charge carrier mobility of holes (up by an order of magnitude) in the diode configuration was observed as compared to the corresponding as-cast films except for the smallest molecular weight sample. Generalizing, the enhanced crystalline order was found to be beneficial for the charge transport even though, the dominant crystallite orientation of P3HT crystallites was edge-on. Another interesting finding was that the charge carrier mobility in both as-cast and melt-crystallized films followed the same relationship as observed for the long period and the volume fraction of the ordered P3HT with molecular weight. Among the investigated samples, P3HT 12 exhibited the highest charge carrier mo-

bilities in both as cast and melt crystallized films. Charge transport in the higher molecular weight samples was limited due to the effects of chain folding and a concomitant increase of the amorphous volume fraction of P3HT. These results clearly demonstrate two major findings: importance of a higher crystalline order and morphology; and an optimal molecular weight sample, P3HT 12, to incorporate as the donor block in the block copolymer for improved charge carrier mobilities.

For the electron accepting materials, unsymmetrical N-substituted perylene bisimide (PBI's) derivatives were investigated as the acceptor counterpart in the block copolymer. The substituents were varied systematically: from hydrophobic alkyl groups (PBI 1) to hydrophilic oligoethylene-glycol groups (OEG) (PBI 2 and PBI 3) while an acrylate backbone was attached to PBI 1 to obtain the side chain polymer(PPerAcr). A similar molecular packing in all the perylene compounds and the side chain polymer i.e. lamello columnar for PBI 1, PBI 3 and PPerAcr and columnar hexagonal for PBI 2 was found. A 3D ordered crystalline phase for PBI 1 was observed. On the other hand, the substitution from alkyl to OEG substituents in PBI 2 and PBI 3 and attachment of the polymeric backbone in PPerAcr resulted in a reduced order exhibiting a liquid crystalline (LC) phase (2D ordered and a disordered columnar stacking) over a broad temperature range. In thin films, all the materials exhibited an amorphous/quenched state in the as-prepared pristine films. An increased molecular order and packing was observed in all the thermally treated films with a dominant edge on orientation of the perylene core. Electron mobilities, as obtained from space charge limited current (SCLC) measurements, in all the pristine films were low ($\approx 10^{-5}$ cm^2/(V·s)) due to a lack of molecular order. Significant improvement in electron mobilities of more than two orders of magnitude for PBI 2 and PBI 3 was observed upon annealing the films within the LC phase. Additionally, thermally treated films of the side chain polymer (PPerAcr), also exhibited an improvement in the electron mobility by an order of magnitude as compared to the as spun films. On the contrary, annealing in the crystalline phase in PBI 1 resulted in reduced electron mobility. These results suggest that while a higher molecular order and packing is crucial, materials with inherent liquid crystalline properties are beneficial for obtaining better charge transport properties as compared to their crystalline counterparts.

As the final objective, the structure formation processes, phase behavior and molecular order in functionalized donor-acceptor block copolymers (P3HT-b-PPerAcr) was studied. Investigations on bulk samples, reveal that both P3HT-b-PPerAcr 5 and 6 microphase separate in the melt forming lamellar and cylindrically microphase separated structures respectively. This was attributed to an increased molecular weight (correspondingly a higher $\chi_F N$) and high purity (absence of triblock copolymer content). The volume fractions at which these microstructures occur are analogous to that known from classical block copolymers containing amorphous blocks. Confined crystallization of the individual components occur within these microphase separated structures without altering the microphase morphology. The crystalline structures of the individual components i.e. P3HT and PPerAcr (as known from pure homopolymers) remained unchanged in the block copolymer systems, implying a high degree of purity in the respective domains. Thus, for the first time, a clear evidence of microphase sepa-

rated morphology was elucidated in a semiconducting donor-acceptor block copolymer containing crystalline/liquid-crystalline components. The microphase morphology as obtained in bulk samples was preserved in thin films. None of the samples (P3HT-b-PPerAcr 5 and 6) in the as spun films exhibited any long range microstructural order and were amorphous. In order to decouple the effect of crystalline order and long range order (microphase separated structures) on the transport properties, different thermal treatments were employed. In the first treatment the films were annealed above the melting temperature of PPerAcr (but below the complete melting of the block copolymer) and cooled to room temperature resulting in an enhanced crystalline order but no well-developed long range order. In the second treatment, films were annealed above the complete melting temperature of the block copolymer and cooled to room temperature resulting in the formation of well-developed microphase separated structures, besides crystalline order. The orientation of the observed microstructures (lamellae and cylinders) was found to be parallel to the substrate. The preferential interfacial interactions of the blocks for both P3HT-b-PPerAcr 5 and 6 with the air/substrate interface, force the alignment of the microstructures parallel to the substrate. Significant textural changes in the crystalline structure (in thermally treated films) were observed particularly in films possessing long range microstructural order due to the confinement effects. A strong morphological and order dependence was observed on the transport properties in the semiconducting conjugated block copolymer. While, poor transport properties were detected in the amorphous, non-microphase separated as spun films; improved charge carrier mobilities were observed in the films possessing crystalline order but no well-developed microphase separated structures . A disruptive percolation pathway for the charge carriers was found to be detrimental due to the presence of misoriented microphase separated structures. Therefore, this research work provides an excellent experimental evidence that both crystalline order and oriented continuous percolating pathways are essential for achieving high charge carrier mobilities.

In conclusion, it was shown that molecularly pure nano-domains on the order of exciton diffusion length can be obtained in block copolymers containing semi-conducting blocks. In general, an increased crystalline order is found to be beneficial for charge transport properties. However, to harness the full potential of employing block copolymer systems for organic photovoltaics (OPV), the obtained microphase separated structures must be oriented perpendicular to the substrate which could be a challenging task. Within the context for applications in OPV, crystallinity determination on an absolute scale in thin films might be crucial for a better understanding of transport behavior. Additionally, new n-type semiconducting materials with liquid crystalline phases could be synthesized and incorporated in block copolymers to improve device performances.

Appendix

A1. Pole figure analysis

As discussed in section 2.4.2, the GIWAXS geometry does not allow observation of intensity directly on the meridian i.e. along the q_z axis. To determine the crystallite orientation in a more quantitative way, scattering patterns were also obtained in specular condition using the method as described by Baker et. al. [132] by tilting the sample such that the angle of incidence is equal to the exit angle $(\alpha_i = \alpha_f)$ for the dominant (100) reflections from PPerAcr and P3HT. This was done for thin film samples of P3HT-b-PPerAcr 5 and 6 with different thermal treatments. A representative scattering pattern of the P3HT-b-PPerAcr 6 film annealed in state 2 in the GIWAXS geometry and the local specular condition for the (100) reflection from PPerAcr is shown in Figure A1. Profile cuts were obtained, using Fit2D software, at the corresponding Bragg reflection over the azimuthal range $\psi = 0°$ to $\psi = 100°$ Figure A2. While $\psi = 0°$ is in the plane of the substrate (equatorial position), $\psi = 90°$ corresponds to a direction perpendicular to the substrate (meridional position).
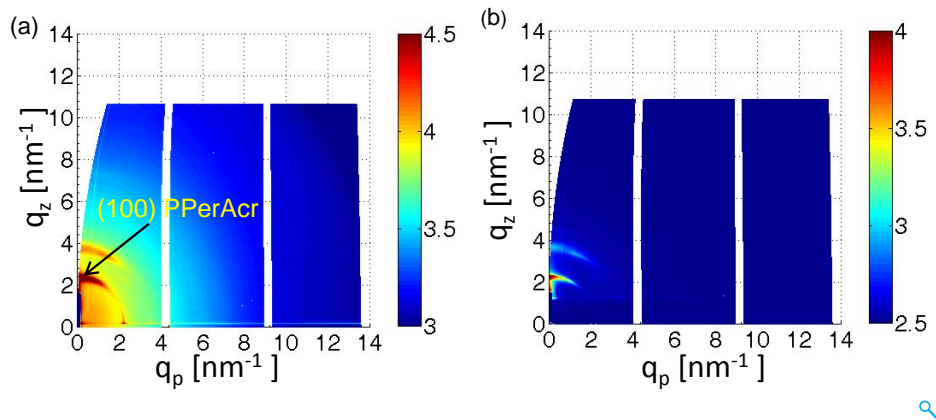

Figure A1: Scattering pattern of P3HT-b-PPerAcr crystallized from the ordered melt (state2) in (a) grazing incidence geometry and (b) in specular condition for the (100) reflection from PPerAcr

Figure A2(a) shows the azimuthal intensity profiles of the (100) reflection from PPerAcr in GIWAXS and local specular condition along with the corresponding profiles from measurements on Si substrate. The azimuthal intensity profile of the (100) reflection of PPerAcr in P3HT-b-PPerAcr 6 films annealed in state 2 Figure A2(b) exhibits a large increase in intensity close to the meridian. The profile shows the presence of two peaks, both centered at the meridian, having peak widths (FWHM) of $\approx$
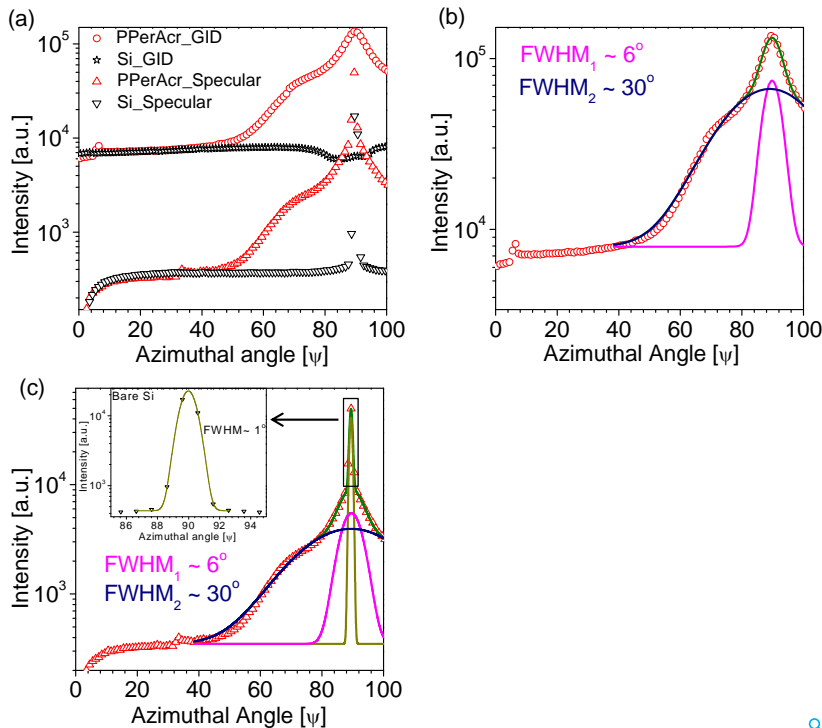
Figure A2: (a) Azimuthal intensity profiles of the (100) PPerAcr reflection from P3HT-b-PPerAcr 6 (annealed in state 2) in GIWAXS geometry (open red circles) and specular condition (open red triangles). The corresponding azimuthal intensity profiles form the bare Si substrate at the (100) PPerAcr position (black open symbols) is also shown for comparison. All the data sets were normalized with respect to the exposure time. (b) Azimuthal intensity profile for the (100) reflection of PPerAcr in GIWAXS geometry fitted with a double gaussian function exhibiting two orientation distribution of crystallites having FWHM of 6° and 30°. (c) Azimuthal intensity profile for the (100) reflection of PPerAcr in specular condition fitted with a triple gaussian function also exhibits two orientation distribution of crystallites having FWHM of 6° and 30°. The additional third peak (FWHM $\approx$ 1°) originates due to the reflection from Si substrate (as also observed from bare Si substrate) (see inset)

6° and 30°. The intensity profile of the same reflection in the specular condition (Figure A2(c)) also reveals the presence of two crystallite orientation distribution at the meridian having similar peak widths (i.e. 6° and 30°) as obtained from the GIWAXS measurement. Additionally, a third peak (FWHM $\approx$ 1° could also be observed. This resolution limited peak could arise from the reflection from Si substrate in the specular condition. Though, at this point we cannot explicitly rule out the possibility of crystallites which are perfectly oriented (FWHM $<$ 1°), preliminary analysis suggests that scattering patterns in the GIWAXS geometry are sufficient to provide complete information of crystalline texture in these samples. Similar analysis was done for the (100) P3HT reflection position and for all the different thermally treated films. Further analysis for understanding and interpreting the crystallite orientation quantitatively is still open.
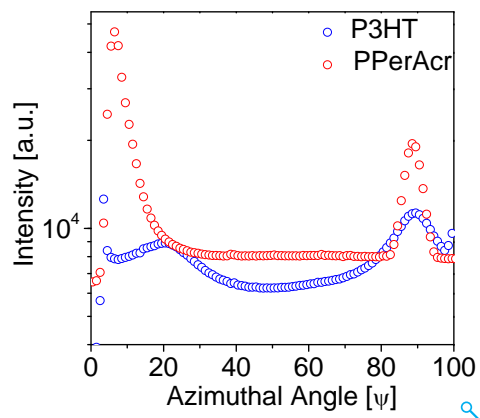
Figure A3: Azimuthal intensity profiles for P3HT-b-PPerAcr 5 films annealed in state 2 corresponding to (100) PPerAcr (red) and (100) P3HT (blue) reflections. The profile cuts for the (100) reflection for PPerAcr exhibits a large increase in intensity along the equatorial position ($\psi = 0°$) indicating a dominant crystallite orientation with the 'a' axis aligned parallel to the substrate. P3HT also shows a bimodal crystallite orientation distribution

Bibliography

[1] D. Chapin, C. Fuller, and G. Pearson, "A new silicon p-n junction photocell for converting solar radiation into electrical power," *Journal of Applied Physics*, vol. 25, p. 676, 1954.

[2] M. Green, K. Emery, Y. Hishikawa, W. Warta, and E. Dunlop, "Solar cell efficiency tables," *Progress in Photovoltaics*, vol. 20, pp. 606–614, 2012.

[3] H. Shirakawa, E. Louis, G. MacDiarmid, C. Chiang, and A. Heeger, "Synthesis of electrically conducting organic polymers: halogen derivatives of polyacetylene," *Journal of the Chemical Society, Chemical Communications*, pp. 578–580, 1977.

[4] R. Friend, R. Gymer, A. Holmes, J. Burroughes, R. Marks, C. Taliani, D. Bradley, D. Dos Santos, J. Bredas, and W. Logdlund, M.and Salaneck, "Electroluminescence in conjugated polymers," *Nature*, vol. 397, pp. 121–128, 1999.

[5] C. Dimitrakapoulos and P. Malenfant, "Organic thin film transistors for large area electronics," *Advanced Materials*, vol. 14, pp. 99–117, 2002.

[6] C. Tang, "Two layer organic photovoltaic cell," *Applied Physics Letters*, vol. 48, pp. 183–185, 1985.

[7] N. Sariciftci, D. Braun, C. Zhang, V. Srdanov, A. Heeger, G. Stucky, and F. Wudl, "Semiconducting polymer-buckminsterfullerene heterojunctions: Diodes, photodiodes, and photovoltaic cells," *Applied Physics Letters*, vol. 62, pp. 585–587, 1993.

[8] J. Halls, K. Pichler, R. Friend, S. Moratti, and A. Holmes, "Exciton diffusion and dissociation in a poly(p-phenylenevinylene)/c-60 heterojunction photovoltaic cell," *Applied Physics Letters*, vol. 68, pp. 3120–3122, 1996.

[9] G. Yu, C. Zhang, and A. Heeger, "Dual-function semiconducting polymer devices: Light-emitting and photodetecting diodes," *Applied Physics Letters*, vol. 64, p. 1540, 1994.

[10] G. Yu, J. Gao, J. Hummelen, F. Wudl, and A. Heeger, "Polymer photovoltaic cells: Enhanced efficiencies via a network of internal donor-acceptor heterojunctions," *Science*, vol. 270, pp. 1789–1791, 1995.

[11] J. Halls, C. A. Walsh, N. Greenham, E. Marseglia, R. Friend, S. Moratti, and A. Holmes, "Efficient photodiodes from interpenetrating polymer networks," *Nature*, vol. 376, pp. 498–500, 1995.

[12] D. Chirvase, J. Parisi, J. Hummelen, and V. Dyakonov, "Influence of nanomorphology on the photovoltaic action of polymer-fullerene composites," *Nanotechnology*, vol. 15, pp. 1317–1323, 2004.

[13] T. Erb, U. Zhokhavets, G. Gobsch, S. Raleva, B. Stuhn, P. Schilinsky, C. Waldauf, and C. Brabec, "Correlation between structural and optical properties of composite polymer/fullerene films for organic solar cells," *Advanced Functional Materials*, vol. 15, no. 7, pp. 1193–1196, 2005.

[14] X. Yang, J. Loos, S. Veenstra, W. Verhees, M. Wienk, J. Kroon, M. Michels, and R. Janssen, "Nanoscale morphology of high-performance polymer solar cells," *NanoLetters*, vol. 5, pp. 579–583, 2005.

[15] W. Ma, C. Yang, X. Gong, K. Lee, and A. Heeger, "Thermally stable, efficient polymer solar cells with nanoscale control of the interpenetrating network morphology," *Advanced Functional Materials*, vol. 15, no. 10, pp. 1617–1622, 2005.

[16] Y. Kim, S. Cook, S. Tuladhar, S. Choulis, J. Nelson, J. Durrant, D. Bradley, M. Giles, I. McCulloch, C. Ha, and M. Ree, "A strong regioregularity effect in self-organizing conjugated polymer films and high-efficiency polythiophene: fullerene solar cells," *Nature Materials*, vol. 5, no. 3, pp. 197–203, 2006.

[17] K. Sivula, Z. Ball, N. Watanabe, and J. Fr'echet, "Amphiphilic diblock copolymer compatibilizers and their effect on the morphology and performance of polythiophene: Fullerene solar cells," *Advanced Materials*, vol. 18, no. 2, pp. 206–210, 2006.

[18] X. Yang, J. vanDuren, R. Janssen, M. Michels, and J. Loos, "Morphology and thermal stability of the active layer in poly(p-phenylenevinylene)/methanofullerene plastic photovoltaic devices," *Macromolecules*, vol. 37, pp. 2151–2158, 2004.

[19] M. Drees, H. Hoppe, C. Winder, H. Neugebauer, N. Sariciftci, W. Schwinger, F. Schaffler, C. Topf, M. Scharber, Z. Zhu, and R. Gaudiana, "Stabilization of the nanomorphology of polymer-fullerene "bulk heterojunction" blends using a novel polymerizable fullerene derivative," *Journal of Materials Chemistry*, vol. 15, pp. 5158–5163, 2005.

[20] X. Yang and J. Loos, "Toward high-performance polymer solar cells: The importance of morphology control," *Macromolecules*, vol. 40, no. 5, pp. 1353–1362, 2007.

[21] J. Chen and C. Hsu, "Conjugated polymer nanostructures for organic solar cell applications," *Polymer Chemistry*, vol. 2, pp. 2707–2722, 2011.

[22] H. Hoppe and N. Sariciftci, "Polymer solar cells," *Advances in Polymer Science*, vol. 214, pp. 1–86, 2008.

[23] C. Singh, M. Sommer, M. Himmerlich, A. Wicklein, S. Krischok, M. Thelakkat, and H. Hoppe, "Morphology controlled open circuit voltage in polymer solar cells," *Physica Status Solidi RRL*, vol. 5, no. 7, pp. 247–249, 2011.

[24] B. de Boer, U. Stalmach, P. van Hutten, C. Melzer, V. Krasnikov, and G. Hadziioannou, "Supramolecular self-assembly and opto-electronic properties of semiconducting block copolymers," *Polymer*, vol. 42, no. 21, pp. 9097–9109, 2001.

[25] S. Lindner, S. Hüttner, A. Chiche, M. Thelakkat, and G. Krausch, "Charge separation at self-assembled nanostructured bulk interface in block copolymers," *Angewandte Chemie-International Edition*, vol. 45, no. 20, pp. 3364–3368, 2006.

[26] S. Sakurai, "Progress in control of microdomain orientation in block copolymers - efficiencies of various external fields," *Polymer*, vol. 49, no. 12, pp. 2781–2796, 2008.

[27] P. Topham, A. Parnell, and R. Hiorns, "Block copolymer strategies for solar cell technology," *Journal of Polymer Science Part B-Polymer Physics*, vol. 49, no. 16, pp. 1131–1156, 2011.

[28] S. Ham, C. Shin, E. Kim, D. Ryu, U. Jeong, T. Russell, and C. Hawker, "Microdomain orientation of ps-b-pmma by controlled interfacial interactions," *Macromolecules*, vol. 41, no. 17, pp. 6431–6437, 2008.

[29] M. Shah and V. Ganesan, "Correlations between morphologies and photovoltaic properties of rod-coil block copolymers," *Macromolecules*, vol. 43, no. 1, pp. 543–552, 2010.

[30] I. Hamley, *The physics of block copolymers.* Oxford University Press, 1998.

[31] I. Hamley, J. Fairclough, F. Bates, and A. Ryan, "Crystallization thermodynamics and kinetics in semicrystalline diblock copolymers," *Polymer*, vol. 39, no. 6-7, pp. 1429–1437, 1998.

[32] Y. Loo, R. Register, and A. Ryan, "Modes of crystallization in block copolymer microdomains: Breakout, templated, and confined," *Macromolecules*, vol. 35, no. 6, pp. 2365–2374, 2002.

[33] J. Xu, J. Fairclough, S. Mai, C. Chaibundit, M. Mingvanish, C. Booth, and A. Ryan, "Crystallization behavior of oxyethylene/oxybutylene diblock and triblock copolymers," *Polymer*, vol. 44, no. 22, pp. 6843–6850, 2003.

[34] S. Li, S. Myers, and R. Register, "Solid-state structure and crystallization in double-crystalline diblock copolymers of linear polyethylene and hydrogenated polynorbornene," *Macromolecules*, vol. 44, no. 22, pp. 8835–8844, 2011.

[35] J. Chang, B. Sun, D. Breiby, M. Nielsen, T. Solling, M. Giles, I. McCulloch, and H. Sirringhaus, "Enhanced mobility of poly(3-hexylthiophene) transistors by spin-coating from high-boiling-point solvents," *Chemistry of Materials*, vol. 16, no. 23, pp. 4772–4776, 2004.

[36] M. Brinkmann and J. Wittmann, "Orientation of regioregular poly(3-hexylthiophene) by directional solidification: A simple method to reveal the semicrystalline structure of a conjugated polymer," *Advanced Materials*, vol. 18, no. 7, pp. 860–863, 2006.

[37] R. Kline, M. Mcgehee, E. Kadnikova, J. Liu, J. Frechet, and M. Toney, "Dependence of regioregular poly(3-hexylthiophene) film morphology and field-effect mobility on molecular weight," *Macromolecules*, vol. 38, no. 8, pp. 3312–3319, 2005.

[38] R. Chesterfield, J. McKeen, C. Newman, P. Ewbank, D. da Silva Filho, J. Bredas, L. Miller, K. Mann, and C. Frisbie, "Organic thin film transistors based on n-alkyl perylene diimides: Charge transport kinetics as a function of gate voltage and temperature," *Journal of Physical Chemistry B*, vol. 108, no. 50, pp. 19281–19292, 2004.

[39] J. Li, F. Dierschke, J. Wu, A. Grimsdale, and K. M?llen, "Poly(2,7-carbazole) and perylene tetracarboxydiimide: a promising donor/acceptor pair for polymer solar cells," *Journal of Materials Chemistry*, vol. 16, no. 1, pp. 96–100, 2006.

[40] P. Kohn, L. Ghazaryan, G. Gupta, M. Sommer, A. Wicklein, M. Thelakkat, and T. Thurn-Albrecht, "Thermotropic behavior, packing, and thin film structure of an electron accepting side-chain polymer," *Macromolecules*, vol. 45, no. 14, pp. 5676–5683, 2012.

[41] B. Boudouris, C. Frisbie, and M. Hillmyer, "Nanoporous poly(3-alkylthiophene) thin films generated from block copolymer templates," *Macromolecules*, vol. 41, no. 1, pp. 67–75, 2008.

[42] C. Dai, W. Yen, Y. Lee, C. Ho, and W. Su, "Facile synthesis of well-defined block copolymers containing regioregular poly(3-hexyl thiophene) via anionic macroinitiation method and their self-assembly behavior," *Journal of the American Chemical Society*, vol. 129, no. 36, pp. 11036–11038, 2007.

[43] T. Higashihara and M. Ueda, "Living anionic polymerization of 4-vinyltriphenylamine for synthesis of novel block copolymers containing low-polydisperse poly(4-vinyltriphenylamine) and regioregular poly(3-hexylthiophene) segments," *Macromolecules*, vol. 42, no. 22, pp. 8794–8800, 2009.

[44] V. Ho, B. Boudouris, B. McCulloch, C. Shuttle, M. Burkhardt, M. Chabinyc, and R. Segalman, "Poly(3-alkylthiophene) diblock copolymers with ordered mi-

crostructures and continuous semiconducting pathways," *Journal of the American Chemical Society*, vol. 133, no. 24, pp. 9270–9273, 2011.

[45] J. Lee, A. Cirpan, T. Emrick, T. Russell, and W. Jo, "Synthesis and photophysical property of well-defined donor-acceptor diblock copolymer based on regioregular poly(3-hexylthiophene) and fullerene," *Journal of Materials Chemistry*, vol. 19, no. 10, pp. 1483–1489, 2009.

[46] S. Miyanishi, Y. Zhang, K. Tajima, and K. Hashimoto, "Fullerene attached all-semiconducting diblock copolymers for stable single-component polymer solar cells," *Chemical Communications*, vol. 46, no. 36, pp. 6723–6725, 2010.

[47] M. Sommer, A. Lang, and M. Thelakkat, "Crystalline-crystalline donor-acceptor block copolymers," *Angewandte Chemie-International Edition*, vol. 47, no. 41, pp. 7901–7904, 2008.

[48] S. Rajaram, P. Armstrong, B. Kim, and J. Frechet, "Effect of addition of a diblock copolymer on blend morphology and performance of poly(3-hexylthiophene):perylene diimide solar cells," *Chemistry of Materials*, vol. 21, no. 9, pp. 1775–1777, 2009.

[49] Y. Tao, B. McCulloch, S. Kim, and R. Segalman, "The relationship between morphology and performance of donor-acceptor rod-coil block copolymer solar cells," *Soft Matter*, vol. 5, no. 21, pp. 4219–4230, 2009.

[50] Q. Zhang, A. Cirpan, T. Russell, and T. Emrick, "Donor-acceptor poly(thiophene-block-perylene diimide) copolymers: Synthesis and solar cell fabrication," *Macromolecules*, vol. 42, no. 4, pp. 1079–1082, 2009.

[51] S. Huettner, M. Sommer, J. Hodgkiss, P. Kohn, T. Thurn-Albrecht, R. Friend, U. Steiner, and M. Thelakkat, "Tunable charge transport using supramolecular self-assembly of nanostructured crystalline block copolymers," *ACS Nano*, vol. 5, no. 5, pp. 3506–3515, 2011.

[52] G. Tu, H. Li, M. Forster, R. Heiderhoff, L. Balk, and U. Scherf, "Conjugated tri-block copolymers containing both electron-donor and electron-acceptor blocks," *Macromolecules*, vol. 39, no. 13, pp. 4327–4331, 2006.

[53] M. Sommer, H. Komber, S. Huettner, R. Mulherin, P. Kohn, N. Greenham, and W. Huck, "Synthesis, purification, and characterization of well-defined all-conjugated diblock copolymers pf8tbt-b-p3ht," *Macromolecules*, vol. 45, no. 10, pp. 4142–4151, 2012.

[54] R. Verduzco, I. Botiz, D. Pickel, S. Kilbey, K. Hong, E. DiMasi, and S. Darling, "Polythiophene-block-polyfluorene and polythiophene-block-poly(fluorene-co-benzothiadiazole): Insights into the self-assembly of all-conjugated block copolymers," *Macromolecules*, vol. 44, no. 3, pp. 530–539, 2011.

[55] C. Guo, Y. Lin, M. Witman, K. Smith, C. Wang, A. Hexemer, J. Strzalka, E. Gomez, and R. Verduzco, "Conjugated block copolymer photovoltaics with near 3 percent efficiency through microphase separation," *NanoLetters*, vol. 13, no. 6, pp. 2957–2963, 2013.

[56] S. Ku, M. Brady, N. Treat, J. Cochran, M. Robb, E. Kramer, M. Chabinyc, and C. Hawker, "A modular strategy for fully conjugated donor-acceptor block copolymers," *Journal of the American Chemical Society*, vol. 134, no. 38, pp. 16040–16046, 2012.

[57] G. Strobl, *The physics of polymers*. Springer, 2007.

[58] H. Sirringhaus, P. Brown, R. Friend, M. Nielsen, K. Bechgaard, B. Langeveld-Voss, A. Spiering, R. Janssen, E. Meijer, P. Herwig, and D. de Leeuw, "Two-dimensional charge transport in self-organized, high-mobility conjugated polymers," *Nature*, vol. 401, no. 6754, pp. 685–688, 1999.

[59] C. Brabec, N. Sariciftci, and J. Hummelen, "Plastic solar cells," *Advanced Functional Materials*, vol. 11, no. 1, pp. 15–26, 2001.

[60] J. Schneider, A. Dadvand, W. Wen, and D. Perepichka, "Tuning the electronic properties of poly(thienothiophene-vinylene)s via alkysulfanyl and alkysulfonyl substituents," *Macromolecules*, vol. 46, pp. 9231–9239, 2013.

[61] V. Ho, B. Boudouris, and R. Segalman, "Tuning polythiophene crystallization through systematic side chain functionalization," *Macromolecules*, vol. 43, no. 19, pp. 7895–7899, 2010.

[62] T. Yamamoto and H. Kokubo, "Seletive stacking of ht-poly(3-n-alkylthiophene-2,5-diyl)s in mixed systems," *Journal of polymer science: Part B: Polymer physics*, vol. 38, p. 84, 2000.

[63] T. Chen, X. Wu, and R. Rieke, "Regiocontrolled synthesis of poly(3-alkylthiophenes) mediated by rieke zinc - their characterization and solid-state properties," *Journal of the American Chemical Society*, vol. 117, no. 1, pp. 233–244, 1995.

[64] R. Loewe, P. Ewbank, J. Liu, L. Zhai, and R. McCullough, "Regioregular, head-to-tail coupled poly(3-alkylthiophenes) made easy by the grim method: Investigation of the reaction and the origin of regioselectivity," *Macromolecules*, vol. 34, pp. 4324–4333, 2001.

[65] T. Yamamoto, K. Sanechika, and A. Yamamoto, "Preparation of thermostable and electric conducting poly(2,5- thienylene)," *Journal of Polymer Science Part C- Polymer Letters*, vol. 18, pp. 9–12, 1980.

[66] R. Elsenbaumer, K. Jen, and R. Oboodi, "Processible and environmentally stable conducting polymers," *Synthetic Metals*, vol. 15, pp. 169–174, 1986.

[67] R. McCullough and R. Lowe, "Enhanced electrical conductivity in regioselectively synthesized poly(3-alkylthiophenes)," *Journal of the Chemical Society, Chemical Communications*, pp. 70–72, 1992.

[68] R. Loewe, M. Khersonsky, and R. McCullough, "A simple method to prepare head-to-tail coupled, regioregular poly(3-alkylthiophenes) using grignard metathesis," *Advanvced Materials*, vol. 11, pp. 250–253, 1999.

[69] R. Kline, M. Mcgehee, E. Kadnikova, J. Liu, and J. Frechet, "Controlling the field-effect mobility of regioregular polythiophene by changing the molecular weight," *Advanced Materials*, vol. 15, no. 18, pp. 1519–1522, 2003.

[70] A. Zen, M. Saphiannikova, D. Neher, J. Grenzer, S. Grigorian, U. Pietsch, U. Asawapirom, S. Janietz, U. Scherf, I. Lieberwirth, and G. Wegner, "Effect of molecular weight on the structure and crystallinity of poly(3-hexylthiophene)," *Macromolecules*, vol. 39, no. 6, pp. 2162–2171, 2006.

[71] S. Allard, M. Forster, B. Souharce, H. Thiem, and U. Scherf, "Organic semiconductors for solution-processable field-effect transistors (ofets)," *Angewandte Chemie, International Edition*, vol. 47, pp. 4070–4098, 2008.

[72] M. Ruderer and P. Müller-Buschbaum, "Morphology of polymer-based bulk heterojunction films for organic photovoltaics," *Soft Matter*, vol. 7, no. 12, pp. 5482–5493, 2011.

[73] Z. Wu, A. Petzold, T. Henze, T. Thurn-Albrecht, R. Lohwasser, M. Sommer, and M. Thelakkat, "Temperature and molecular weight dependent hierarchical equilibrium structures in semiconducting poly(3-hexylthiophene)," *Macromolecules*, vol. 43, no. 10, pp. 4646–4653, 2010.

[74] P. Arosio, M. Moreno, A. Famulari, G. Raos, M. Catellani, and S. Meille, "Ordered stacking of regioregular head-to-tail polyalkylthiophenes: Insights from the crystal structure of form i ' poly(3-n-butylthiophene)," *Chemistry of Materials*, vol. 21, no. 1, pp. 78–87, 2009.

[75] T. Prosa, M. Winokur, and R. McCullough, "Evidence of a novel side chain structure in regioregular poly(3-alkylthiophenes)," *Macromolecules*, vol. 29, no. 10, pp. 3654–3656, 1996.

[76] T. Prosa, M. Winokur, J. Moulton, P. Smith, and A. Heeger, "X-ray structural studies of poly(3-alkylthiophenes) - an example of an inverse comb," *Macromolecules*, vol. 25, no. 17, pp. 4364–4372, 1992.

[77] K. Tashiro, M. Kobayashi, T. Kawai, and K. Yoshino, "Crystal structural change in poly(3-alkyl thiophene)s induced by iodine doping as studied by an organized combination of x-ray diffraction, infrared/raman spectroscopy and computer simulation techniques," *Polymer*, vol. 38, no. 12, pp. 2867–2879, 1997.

[78] M. Brinkmann and P. Rannou, "Effect of molecular weight on the structure and morphology of oriented thin films of regioregular poly(3-hexylthiophene) grown by directional epitaxial solidification," *Advanced Functional Materials*, vol. 17, no. 1, pp. 101–108, 2007.

[79] R. Kline, D. DeLongchamp, D. Fischer, E. Lin, L. Richter, M. Chabinyc, M. Toney, M. Heeney, and I. McCulloch, "Critical role of side-chain attachment density on the order and device performance of polythiophenes," *Macromolecules*, vol. 40, no. 22, pp. 7960–7965, 2007.

[80] R. Zhang, B. Li, M. Iovu, M. Jeffries-EL, G. Sauve, J. Cooper, S. Jia, S. Tristram-Nagle, D. Smilgies, D. Lambeth, R. McCullough, and T. Kowalewski, "Nanostructure dependence of field-effect mobility in regioregular poly(3-hexylthiophene) thin film field effect transistors," *Journal of the American Chemical Society*, vol. 128, no. 11, pp. 3480–3481, 2006.

[81] L. Hartmann, K. Tremel, S. Uttiya, E. Crossland, S. Ludwigs, N. Kayunkid, C. Vergnat, and M. Brinkmann, "2d versus 3d crystalline order in thin films of regioregular poly(3-hexylthiophene) oriented by mechanical rubbing and epitaxy," *Advanced Functional Materials*, vol. 21, no. 21, pp. 4047–4057, 2011.

[82] L. Jimison, M. Toney, I. McCulloch, M. Heeney, and A. Salleo, "Charge-transport anisotropy due to grain boundaries in directionally crystallized thin films of regioregular poly(3-hexyl-thiophene)," *Advanced Materials*, vol. 21, pp. 1568–1572, 2009.

[83] S. Hugger, R. Thomann, T. Heinzel, and T. Thurn-Albrecht, "Semicrystalline morphology in thin films of poly(3-hexylthiophene)," *Colloid and Polymer Science*, vol. 282, no. 8, pp. 932–938, 2004.

[84] T. Shabi, S. Grigorian, M. Brinkmann, U. Pietsch, N. Koenen, N. Kayunkid, and U. Scherf, "Enhancement in crystallinity of poly(3-hexylthiophene) thin films prepared by low-temperature drop casting," *Journal of Applied Polymer Science*, vol. 125, no. 3, pp. 2335–2341, 2012.

[85] D. Choi, S. Jin, Y. Lee, S. Kim, D. Chung, K. Hong, C. Yang, J. Jung, J. Kim, M. Ree, and C. Park, "Direct observation of interfacial morphology in poly(3-hexylthiophene) transistors: Relationship between grain boundary and field-effect mobility," *Applied Materials and Interfaces*, vol. 2, no. 1, pp. 48–53, 2010.

[86] H. Stegemeyer, *Topics in physical chemistry*. Springer New York and Steinkopff Darmstadt, 1994.

[87] S. Kelly and M. O'Neill, *Handbook of advanced electronic and photonic materials and devices*. Liquid Crystals, Display and Laser Materials, 2000.

[88] S. Chandrashekhar, B. Sadashiva, and K. Suresh, "Liquid crystals of disc like molecules," *Pramana*, vol. 9, pp. 471–480, 1977.

[89] S. Laschat, A. Baro, N. Steinke, F. Giesselmann, C. H„gele, G. Scalia, R. Judele, E. Kapatsina, S. Sauer, A. Schreivogel, and M. Tosoni, "Discotic liquid crystals: From tailor-made synthesis to plastic electronics," *Angewandte Chemie-International Edition*, vol. 46, pp. 4832–4887, 2007.

[90] L. Ghazryan, "Structural investigations on perylene bisimide and poly(perylene bisimide acrylate)," Master's thesis, Martin Luther University Halle-Wittenberg, 2010.

[91] S. Prasad, D. Rao, S. Chandrasekhar, and S. Kumar, "X-ray studies on the columnar structures of discotic liquid crystals," *Molecular Crystals and Liquid Crystals*, vol. 396, pp. 121–139, 2003.

[92] B. Glüsen, W. Heitz, A. Kettner, and J. Wendorff, "A plastic columnar discotic phase," *Liquid Crystals*, vol. 20, no. 5, pp. 627–633, 1996.

[93] F. Maeda, K. Hatsusaka, K. Ohta, and M. Kimura, "Discotic liquid crystals of transition metal complexes. part 35. establishment of a unique mesophase in bis(octaalkoxyphthalocyaninato)lutetium(iii) complexes," *Journal of Materials Chemistry*, vol. 13, pp. 243–251, 2003.

[94] W. Pisula, M. Zorn, J. Chang, K. Müllen, and R. Zentel, "Liquid crystalline ordering and charge transport in semiconducting materials," *Macromolecular Rapid Communications*, vol. 30, no. 14, pp. 1179–1202, 2009.

[95] F. Nolde, W. Pisula, S. Muller, C. Kohl, and K. Müllen, "Synthesis and self-organization of core-extended perylene tetracarboxdiimides with branched alkyl substituents," *Chemistry of Materials*, vol. 18, no. 16, pp. 3715–3725, 2006.

[96] A. Wicklein, P. Kohn, L. Ghazaryan, T. Thurn-Albrecht, and M. Thelakkat, "Synthesis and structure elucidation of discotic liquid crystalline perylene imide benzimidazole," *Chemical Communications*, vol. 46, no. 13, pp. 2328–2330, 2010.

[97] C. Struijk, A. Sieval, J. Dakhorst, M. van Dijk, B. Kimkes, R. Koehorst, H. Donker, T. Schaafsma, S. Picken, A. van de Craats, J. Warman, H. Zuilhof, and E. Sudh"lter, "Liquid crystalline perylene diimides: Architecture and charge carrier mobilities," *Journal of the American Chemical Society*, vol. 122, no. 45, pp. 11057–11066, 2000.

[98] G. Zucchi, D. Donnio, and Y. Geerts, "Remarkable miscibility between disk- and lathlike mesogens," *Chemistry of Materials*, vol. 17, no. 17, pp. 4273–4277, 2005.

[99] Y. Xu, S. Leng, C. Xue, R. Sun, J. Pan, J. Ford, and S. Jin, "A room-temperature liquid-crystalline phase with crystalline ã stacks," *Angewandte Chemie-International Edition*, vol. 46, no. 21, pp. 3896–3899, 2007.

[100] S. Liu, G. Sui, R. Cormier, R. Leblanc, and B. Gregg, "Self-organizing liquid crystal perylene diimide thin films: Spectroscopy, crystallinity, and molecular

orientation," *Journal of Physical Chemistry B*, vol. 106, no. 6, pp. 1307–1315, 2002.

[101] E. Zhou, J. Cong, Q. Wei, K. Tajima, C. Yang, and K. Hashimoto, "All-polymer solar cells from perylene diimide based copolymers: Material design and phase separation control," *Angewandte Chemie-International Edition*, vol. 50, no. 12, pp. 2799–2803, 2011.

[102] X. Zhan, Z. Tan, B. Domercq, Z. An, X. Zhang, S. Barlow, Y. Li, D. Zhu, B. Kippelen, and S. Marder, "A high-mobility electron-transport polymer with broad absorption and its use in field-effect transistors and all-polymer solar cells," *Journal of the American Chemical Society*, vol. 129, no. 23, pp. 7246–7247, 2007.

[103] C. Finlayson, R. Friend, M. Otten, E. Schwartz, J. Cornelissen, R. Nolte, A. Rowan, P. Samori, V. Palermo, A. Liscio, K. Peneva, K. Müllen, S. Trapani, and D. Beljonne, "Electronic transport properties or ensembles of perylene-substituted poly-isocyanopeptide arrays," *Advanced Functional Materials*, vol. 18, no. 24, pp. 3947–3955, 2008.

[104] S. Hüttner, M. Sommer, and M. Thelakkat, "n-type organic field effect transistors from perylene bisimide block copolymers and homopolymers," *Applied Physics Letters*, vol. 92, no. 9, p. 093302, 2008.

[105] I. Tahar-Djebbar, F. Nekelson, B. Heinrich, B. Donnio, D. Guillon, D. Kreher, F. Mathevet, and A. Attias, "Lamello-columnar mesophase formation in a side-chain liquid crystal pi-conjugated polymer architecture," *Chemistry of Materials*, vol. 23, no. 21, pp. 4653–4656, 2011.

[106] S. Kumar, "Triphenylene-based discotic liquid crystal dimers, oligomers and polymers," *Liquid Crystals*, vol. 32, no. 9, pp. 1089–1113, 2005.

[107] A. Donald and A. Windle, *Liquid crystalline polymers*. Cambridge University Press, 1992.

[108] N. Boden, R. Bushby, and Z. Lu, "A rational synthesis of polyacrylates with discogenic side groups," *Liquid Crystals*, vol. 25, no. 1, pp. 47–58, 1998.

[109] W. Kreuder and H. Ringsdorf, "Liquid-crystalline polymers with disc-like mesogens," *Macromolecules Chemistry, Rapid Communications.*, vol. 4, no. 12, pp. 807–815, 1983.

[110] M. Sommer, S. Lindner, and M. Thelakkat, "Microphase-separated donor-acceptor diblock copolymers: Influence of homo energy levels and morphology on polymer solar cells," *Advanced Functional Materials*, vol. 17, no. 9, pp. 1493–1500, 2007.

[111] S. Darling, "Directing the self-assembly of block copolymers," *Progress in Polymer Science*, vol. 32, no. 10, pp. 1152–1204, 2007.

[112] L. Leibler, "Theory of microphase separation in block copolymers," *Macromolecules*, vol. 13, no. 6, pp. 1602–1617, 1980.

[113] S. Aggarwal, "Structure and properties of block polymers and multiphase polymer systems: an overview of present status and future potential," *Polymer*, vol. 17, pp. 938–956, 1976.

[114] G. Kampf, M. Hoffmann, and H. Kromer, "Konformation, ubermolekulare struktur und weitreichende ordnung in nichtkristallinen und nichtstereospezifischen polymeren. teil 1. sichtbare ubermolekulare strukturen und weitreichende ordnungen in nichtkristallinen blockcopolymeren," *Berichte der Bunsengesellschaft für physikalische Chemie*, vol. 74, no. 8-9, pp. 851–859, 1970.

[115] N. Hadjichristdis, S. Pispas, and G. Floudas, *Block co-polymers: Synthetic strategies, physical properties and applications*. Wiley Interscience, 2003.

[116] S. Krause, "Polymer compatibility," *Journal of Macromolecular Science- Reviews in Macromolecular Chemistry and Physics*, vol. C7, p. 251, 1972.

[117] M. Matsen and F. Bates, "Block copolymer microstructures in the intermediate-segregation regime," *Journal of Chemical Physics*, vol. 106, no. 6, pp. 2436–2448, 1997.

[118] E. Helfand and Z. Wasserman, "Block copolymer theory .4. narrow interphase approximation," *Macromolecules*, vol. 9, no. 6, pp. 879–888, 1976.

[119] E. Helfand and Z. Wasserman, "Microdomain structure and the interface in block copolymers," in *Developments in Block Copolymers - 1* (I. Goodman, ed.), pp. 99–125, London: Appl. Sci. Publ., 1982.

[120] R. Lohwasser, G. Gupta, P. Kohn, M. Sommer, A. Lang, T. Thurn-Albrecht, and M. Thelakkat, "Phase separation in the melt and confined crystallization as the key to well-ordered microphase separated donor-acceptor block copolymers," *Macromolecules*, vol. 46, no. 11, pp. 4403–4410, 2013.

[121] M. Matsen and M. Schick, "Stable and unstable phases of a diblock copolymer melt," *Physical Review Letters*, vol. 72, no. 16, pp. 2660–2663, 1994.

[122] M. Matsen and F. Bates, "Origins of complex self-assembly in block copolymers," *Macromolecules*, vol. 29, no. 23, pp. 7641–7644, 1996.

[123] C. Kittel, *Introduction to Solid state Physics*. Hohn Wiley and Sons, Inc., 1986.

[124] R. Roe, *Methods of x-ray and neutron scattering in polymer science*. Oxford University Press, 2000.

[125] J. Levine, J. Cohen, Y. Chung, and P. Georgopoulos, "Grazing-incidence small-angle x-ray scattering: new tool for studying thin film growth," *Journal of Applied Crystallography*, vol. 22, pp. 528–532, 1989.

[126] P. Müller-Buschbaum, P. Vanhoorne, V. Scheumann, and M. Stamm, "Observation of nano-dewetting structures," *Europhysics Letters*, vol. 40, pp. 655–660, 1997.

[127] M. Tolan, *X-ray scattering from soft matter thin films.* Springer-Verlag Berlin Heidelberg, 1999.

[128] P. Müller-Buschbaum, *Polymer surfaces and interfaces: Characterization, modification and applications.* Springer-Verlag Berlin Heidelberg, 2008.

[129] P. Müller-Buschbaum, *A basic introduction to grazing incidence small angle x-ray scattering.* Springer-Verlag Berlin Heidelberg, 2009.

[130] S. Sinha, E. Sirota, S. Garoff, and H. Stanley, "X-ray and neutron-scattering from rough surfaces," *Physical Review B*, vol. 38, no. 4, pp. 2297–2311, 1988.

[131] Y. Yoneda, "Anomalous surface reflection of x rays," *Physical Review*, vol. 131, no. 5, pp. 2010–2013, 1963.

[132] J. Baker, L. Jimison, S. Mannsfeld, S. Volkman, S. Yin, V. Subramanian, A. Salleo, A. Alivisatos, and M. Toney, "Quantification of thin film crystallographic orientation using x-ray diffraction with an area detector," *Langmuir*, vol. 26, no. 11, pp. 9146–9151, 2010.

[133] C. Singh, *Correlation of charge transport with structural properties in poly3-hexylthiophene-polyperyleneacrylate block copolymers and its implication on solar cell performance.* PhD thesis, Technical University Ilmeanu, 2013.

[134] C. Child, "Discharge from hot calcium oxide," *Physical Review Series I*, vol. 32, pp. 492–511, 1911.

[135] N. Mott and R. W. Gurney, "Electronic processes in ionic crystals," *Oxford University Press, New York*, vol. 172, 1940.

[136] P. Murgatroyd, "Theory of space-charge-limited current enhanced by frenkel effect," *Journal of Physics D: Applied Physics*, vol. 3, pp. 151–156, 1970.

[137] A. Mozer, N. Sariciftci, A. Pivrikas, R. Osterbacka, G. Juska, L. Brasat, and H. Bässler, "Charge carrier mobility in regioregular poly(3-hexylthiophene) probed by transient conductivity techniques: A comparative study," *Physical Review B*, vol. 71, pp. 035214:1–9, 2005.

[138] H. Bässler, "Charge transport in disordered organic photoconductors - a monte carlo simulation study," *Physica Status Solidi B*, vol. 175, pp. 15–56, 1993.

[139] C. Deibel and V. Dyakonov, "Polymer-fullerene bulk heterojunction solar cells," *Reprts on Progress in Physics*, vol. 73, p. 096401, 2010.

[140] V. Mathot, *Calorimetry and thermal analysis of polymers.* Carl Hanser Verlag, 1994.

[141] D. Williams, *Transmission Electron Microscopy: A textbook for materials science.* Plenium Press, New York, 1996.

[142] C. Sawyer, *Polymer Microscopy.* Springer, 2008.

[143] F. Ebert and T. Thurn-Albrecht, "Controlling the orientation of semicrystalline polymers by crystallization in magnetic fields," *Macromolecules*, vol. 36, no. 23, pp. 8685–8694, 2003.

[144] L. Schulz, "Determination of preferred orientation of a flat reflection samples using a geiger counter x-ray spectrometer," *Journal of Applied Physics*, vol. 20, pp. 1030–1032, 1949.

[145] http://www.esrf.eu/UsersAndScience/Experiments/SoftMatter/ID10, January 10 2014.

[146] T. Henze, *Rasterkraftmikroskopische Untersuchungen an dunnen epitaktisch kristallisierten Filmen des Polyethylens.* PhD thesis, Martin Luther University, Halle-Wittenberg, 2010.

[147] B. Bhushan, *Applied scanning probe methods.* Springer-Verlag Berlin Heidelberg, 2004.

[148] K. Schröter, A. Petzold, T. Henze, and T. Thurn-Albrecht, "Quantitative analysis of scanning force microscopy data using harmonic models," *Macromolecules*, vol. 42, no. 4, pp. 1114–1124, 2009.

[149] A. Zen, J. Pflaum, S. Hirschmann, W. Zhuang, F. Jaiser, U. Asawapirom, J. Rabe, U. Scherf, and D. Neher, "Effect of molecular weight and annealing of poly (3-hexylthiophene)s on the performance of organic field-effect transistors," *Advanced Functional Materials*, vol. 14, no. 8, pp. 757–764, 2004.

[150] M. Surin, P. Leclere, R. Lazzaroni, J. Yuen, G. Wang, D. Moses, A. Heeger, S. Cho, and K. Lee, "Relationship between the microscopic morphology and the charge transport properties in poly(3-hexylthiophene) field-effect transistors," *Journal of Applied Physics*, vol. 100, pp. 33712: 1–6, 2006.

[151] M. Dang, L. Hirsch, and G. Wantz, "Polymeric solar cells based on p3ht:pcbm: Role of the casting solvent," *Advanced Materials*, vol. 23, pp. 3597–3602, 2011.

[152] C. Dimitrakopoulos and D. Mascaro, "Organic thin-film transistors: A review of recent advances," *IBM Journal of Research and Development*, vol. 45, no. 1, pp. 11–27, 2001.

[153] R. Kline, M. Mcgehee, and M. Toney, "Highly oriented crystals at the buried interface in polythiophene thin-film transistors," *Nature Materials*, vol. 5, no. 3, pp. 222–228, 2006.

[154] M. Brinkmann, "Structure and morphology control in thin films of regioregular poly(3-hexyl-thiophene)," *Journal of Polymer Science Part B-Polymer Physics*, vol. 49, pp. 1218–1233, 2011.

[155] R. Kline and M. Mcgehee, "Morphology and charge transport in conjugated polymers," *Journal of Macromolecular Science Part C Polymer Reviews*, vol. 46, pp. 27–45, 2006.

[156] E. Fischer, "Effect of annealing and temperature on the morphological structures of polymers," *Pure and Applied Chemistry*, vol. 31, pp. 113–132, 1972.

[157] C. Singh, G. Gupta, R. Lohwasser, S. Engmann, J. Balko, M. Thelakkat, T. Thurn-Albrecht, and H. Hoppe, "Correlation of charge transport with structural order in highly ordered melt-crystallized poly 3-hexylthiophene thin films," *Journal of Polymer Science Part B-Polymer Physics*, vol. 51, no. 12, pp. 943–951, 2013.

[158] R. Lohwasser and M. Thelekkat, "Toward perfect control of end groups and polydispersity in poly(3-hexylthiophene) via catalyst transfer polymerization," *Macromolecules*, vol. 44, pp. 3388–3397, 2011.

[159] G. Greczynski, T. Kugler, and W. Salaneck, "Characterization of the pedot-pss system by means of x-ray and ultraviolet photoelectron spectroscopy," *Thin Solid Films*, vol. 354, pp. 129–135, 1999.

[160] C. Scharsich, R. Lohwasser, M. Sommer, U. Asawapirom, U. Scherf, M. Thelakkat, D. Neher, and A. K"hler, "Control of aggregate formation in poly(3-hexylthiophene) by solvent, molecular weight, and synthetic method," *Journal of Polymer Science Part B-Polymer Physics*, vol. 50, no. 6, pp. 442–453, 2012.

[161] A. Patterson, "The scherrer formula for x-ray particle size determination," *Physical Review*, vol. 56, pp. 978–982, 1939.

[162] A. Virkar, S. Mannsfeld, Z. Bao, and N. Stingelin, "Organic semiconductor growth and morphology considerations for organic thin-film transistors," *Advanced Materials*, vol. 22, no. 34, pp. 3857–3875, 2010.

[163] M. Brinkmann and P. Rannou, "Molecular weight dependence of chain packing and semicrystalline structure in oriented films of regioregular poly(3-hexylthiophene) revealed by high-resolution transmission electron microscopy," *Macromolecules*, vol. 42, no. 4, pp. 1125–1130, 2009.

[164] C. Goh, R. Kline, M. McGehee, E. Kadnikova, and J. Frechet, "Molecular-weight-dependent mobilities in regioregular poly(3-hexyl-thiophene) diodes," *Applied Physics Letters*, vol. 86, pp. 122110:1–3, 2005.

[165] C. Müller, N. Zhigadlo, A. Kumar, M. Baklar, J. Karpinski, P. Smith, T. Kreouzis, and N. Stingelin, "Enhanced charge-carrier mobility in high-pressure-crystallized poly(3-hexylthiophene)," *Macromolecules*, vol. 44, no. 6, pp. 1221–1225, 2011.

[166] A. Ballantyne, L. Chen, J. Dane, T. Hammant, F. Braun, M. Heeney, W. Duffy, I. McCulloch, D. Bradley, and J. Nelson, "The effect of poly(3-hexylthiophene) molecular weight on charge transport and the performance of polymer:fullerene solar cells," *Advanced Functional Materials*, vol. 18, pp. 2373–2380, 2008.

[167] K. Singh, G. Sauve, R. Zhang, T. Kowalewski, R. McCullough, and L. Porter, "Dependence of field-effect mobility and contact resistance on nanostructure in regioregular poly(3-hexylthiophene) thin film transistors," *Applied Physics Letters*, vol. 92, pp. 2955515 :1–3, 2008.

[168] P. Kohn, S. Huettner, H. Komber, V. Senkovskyy, R. Tkachov, A. Kiriy, R. Friend, U. Steiner, W. Huck, J. Sommer, and M. Sommer, "On the role of single regiodefects and polydispersity in regioregular poly(3-hexylthiophene): Defect distribution, synthesis of defect-free chains, and a simple model for the determination of crystallinity," *Journal of the American Chemical Society*, vol. 134, no. 10, pp. 4790–4805, 2012.

[169] J. Rivnay, L. H. Jimison, J. E. Northrup, M. F. Toney, R. Noriega, S. F. Lu, T. J. Marks, A. Facchetti, and A. Salleo, "Large modulation of carrier transport by grain-boundary molecular packing and microstructure in organic thin films," *Nature Materials*, vol. 8, pp. 952–958, 2009.

[170] K. Law, "Organic photoconductive materials- recent trends and developments," *Chemical Reviews*, vol. 93, pp. 449–486, 1993.

[171] C. Huang, S. Barlow, and S. Marder, "Perylene-3,4,9,10-tetracarboxylic acid diimides: Synthesis, physical properties, and use in organic electronics," *Journal of Organic Chemistry*, vol. 76, no. 8, pp. 2386–2407, 2011.

[172] V. Kamm, G. Battagliarin, I. Howard, W. Pisula, A. Mavrinskiy, C. Li, K. M?llen, and F. Laquai, "Polythiophene:perylene diimide solar cells - the impact of alkyl-substitution on the photovoltaic performance," *Advanced Energy Materials*, vol. 1, no. 2, pp. 297–302, 2011.

[173] F. Würthner, "Perylene bisimide dyes as versatile building blocks for functional supramolecular architectures," *Chemical Communications*, vol. 14, pp. 1564–1579, 2004.

[174] A. Wicklein, A. Lang, M. Muth, and M. Thelakkat, "Swallow-tail substituted liquid crystalline perylene bisimides: Synthesis and thermotropic properties," *Journal of the American Chemical Society*, vol. 131, no. 40, pp. 14442–14453, 2009.

[175] V. Marcon, D. Breiby, W. Pisula, J. Dahl, J. Kirkpatrick, S. Patwardhan, F. Grozema, and D. Andrienko, "Understanding structure-mobility relations for perylene tetracarboxydiimide derivatives," *Journal of the American Chemical Society*, vol. 131, no. 32, pp. 11426–11432, 2009.

[176] T. Kelley, D. Muyres, P. Baude, T. Smith, and T. Jones, "High performance organic thin film transistors," *Materials Research Society Proceedings*, vol. 771, p. L6.5, 2003.

[177] M. Muth, G. Gupta, A. Wicklein, M. Orozco, T. Thurn-Albrecht, and M. Thelakkat, "Crystalline vs liquid crystalline perylene bisimides: Improved electron mobility via substituent alteration," *Journal of Physical Chemistry C*, vol. 118, pp. 92–102, 2014.

[178] S. Lindner and M. Thelakkat, "Nanostructures of n-type organic semiconductor in a p-type matrix via self-assembly of block copolymers," *Macromolecules*, vol. 37, no. 24, pp. 8832–8835, 2004.

[179] M. Bushey, A. Hwang, P. Stephens, and C. Nuckolls, "Enforced stacking in crowded arenes," *Journal of the American Chemical Society*, vol. 123, no. 33, pp. 8157–8158, 2001.

[180] M. Kastler, W. Pisula, F. Laquai, A. Kumar, R. Davies, S. Baluschev, M. Garcia-Gutierrez, D. Wasserfallen, H. Butt, C. Riekel, G. Wegner, and K. Müllen, "Organization of charge-carrier pathways for organic electronics," *Advanced Materials*, vol. 18, no. 17, pp. 2255–2259, 2006.

[181] S. Krimm and A. Tobolsky, "Quantitative x-ray studies of order in amorphous and crystalline polymers - quantitative x-ray determination of crystallinity in polyethylene," *Journal of Polymer Science*, vol. 7, no. 1, pp. 57–76, 1951.

[182] T. Krauss, E. Barrena, D. de Oteyza, X. Zhang, J. Major, V. Dehm, F. Wuerthner, and H. Dosch, "X-ray/atomic force microscopy study of the temperature-dependent multilayer structure of ptcdi-c-8 films on silicon dioxide," *Journal of Physical Chemistry C*, vol. 113, pp. 4502–4506, 2009.

[183] C. Park, J. Yoon, and E. L. Thomas, "Enabling nanotechnology with self assembled block copolymer patterns," *Polymer*, vol. 44, p. 6725, 2003.

[184] F. Bates and G. Fredrickson, "Block copolymer thermodynamics: Theory and experiment," *Annual Review of Physical Chemistry*, vol. 41, pp. 525–557, 1990.

[185] M. Fasolka and A. Mayes, "Block copolymer thin films: Physics and applications," *Annual Review of Materials Research*, vol. 31, pp. 323–355, 2001.

[186] M. Jeffries-El, G. Sauve, and R. McCullough, "Facile synthesis of end-functionalized regioregular poly(3-alkylthiophene)s via modified grignard metathesis reaction," *Macromolecules*, vol. 38, pp. 10346–10352, 2005.

[187] A. Mayes and M. Olvera de la Cruz, "Microphase separation in multiblock copolymer melts," *Journal of Chemical Physics*, vol. 91, pp. 7228–7235, 1989.

[188] P. Busch, D. Posselt, D. Smilgies, B. Rheinl„nder, F. Kremer, and C. Papadakis, "Lamellar diblock copolymer thin films investigated by tapping mode atomic force microscopy: Molar-mass dependence of surface ordering," *Macromolecules*, vol. 36, no. 23, pp. 8717–8727, 2003.

[189] H. Kim and T. Russell, "Ordering in thin films of asymmetric diblock copolymers," *Journal of Polymer Science Part B-Polymer Physics*, vol. 39, no. 6, pp. 663–668, 2001.

[190] S. Kim, M. Misner, and T. Russell, "Controlling orientation and order in block copolymer thin films," *Advanced Materials*, vol. 20, no. 24, pp. 4851–4856, 2008.

[191] P. Borsenberger and J. Fitzgerald, "Effects of the dipole-moment on the charge transport in disordered molecular-solids," *Journal of Physical Chemistry*, vol. 97, pp. 4815–4819, 1993.

[192] C. Groves, L. J. A. Koster, and N. C. Greenham, "The effect of morphology upon mobility: Implications for bulk heterojunction solar cells with nonuniform blend morphology," *Journal of Applied Physics*, vol. 105, pp. 094510(1–6), 2009.

Acknowledgement

Eidesstattliche Erklärung

Hiermit erkläre ich an Eides statt, dass ich die vorliegende Arbeit selbständig und ohne fremde Hilfe verfasst, andere als die angegebenen Quellen und Hilfsmittel nicht benutzt und die aus anderen Quellen entnommenen Stellen als solche gekennzeichnet habe. Ferner habe ich nicht versucht, anderweitig mit oder ohne Erfolg eine Dissertation einzureichen oder mich einer Doktorprüfung zu unterziehen.

Gaurav Kumar Gupta

Halle (Saale), January 15, 2014

Curriculum vitae

First Name	Gaurav Kumar
Family Name	Gupta
Date of Birth	November 09, 1982
Place of Birth	Allahabad, India
Nationality	Indian
E-mail	ggbhai1982@gmail.com

EDUCATION

Aug. 2001 - Jul. 2004	Bachelor of Science Allahabad Central University Allahabad, India
Aug. 2004 - Jun. 2006	Master of Science Allahabad Central University Allahabad, India
Jul. 2007 - Jun. 2009	Master of Technology Materials Science Indian Institute of Technology Kanpur, India
Since Sep. 2009	**Ph.D** in Institut für Physik Experimental Polymer Physics Martin-Luther-Universität Halle-Wittenberg (Supervised by Prof. Thomas Thurn-Albrecht)

Publications

1. R.H. Lohwasser, G. Gupta, P. Kohn, M. Sommer, A.S. Lang, T. Thurn-Albrecht, and M. Thelakkat, 'Phase separation in the melt and confined crystallization as the key to well-ordered microphase separated donor acceptor block copolymers', Macromolecules 2013, vol. 46, 4403-4410

2. C.R. Singh, G. Gupta, R.H. Lohwasser, S. Engmann, J. Balko, M. Thelakkat, T. Thurn-Albrecht, H. Hoppe, 'Correlation of charge transport with structural order in highly ordered melt crystallized P3HT films', Journal of Polymer Science Polymer Physics B, 2013, vol. 51, 943-951

3. M.A. Muth, G. Gupta, A. Wicklein, M. Carrasco-Orozco, T. Thurn-Albrecht, and M. Thelakkat, 'Crystalline vs liquid crystalline perylene bisimides: Improved electron mobility via substituent alteration', The Journal of Physical Chemistry C, 2014, vol. 118, 92-102

4. P. Kohn, L. Ghazaryan, G. Gupta, M. Sommer, A. Wicklein, M. Thelakkat, T. Thurn-Albrecht, 'Thermotropic behavior, packing, and thin film structure of an electron accepting side-chain polymer', Macromolecules, 2012, vol. 45, 5676-5683

5. H.H. Le, K. Oswald, S. Wiesner, A. Das, K.W. Stöckelhuber, R. Boldt, G. Gupta, G. Heinrich, H.J. Radusch, 'Location of dispersing agent in rubber nanocomposites during mixing process', Polymer, 2013, vol. 54, 7009-7021